The Pennsylvania State University

The Graduate School

Graduate Program in Acoustics

LOW WAVENUMBER TURBULENT BOUNDARY LAYER WALL PRESSURE AND SHEAR STRESS MEASUREMENTS FROM VIBRATION DATA ON A CYLINDER IN PIPE FLOW

A Dissertation in

Acoustics

by

William K. Bonness

Submitted in Partial Fulfillment
of the Requirements
for the Degree of

Doctor of Philosophy

August 2009

The dissertation of William K. Bonness was reviewed and approved* by the following:

Dean E. Capone
Senior Research Associate
Associate Professor of Acoustics
Dissertation Advisor
Chair of Committee

Stephen A. Hambric
Senior Scientist
Professor of Acoustics

Martin W. Trethewey
Professor of Mechanical Engineering

Gary H. Koopmann
Distinguished Professor of Mechanical Engineering

Anthony A. Atchley
Professor of Acoustics
Head of the Graduate Program in Acoustics

*Signatures are on file in the Graduate School

ABSTRACT

The response of a structure to turbulent boundary layer (TBL) excitation has been an area of research for roughly fifty years. However, uncertainties persist surrounding the low wavenumber levels of TBL surface pressure and shear stress spectra. In this experimental investigation, a cylindrical shell with a smooth internal surface is subjected to TBL excitation from water in fully developed pipe flow at 6.1 m/s. The cylinder's vibration response is used to inversely determine low wavenumber TBL surface pressure and shear stress levels. A three-dimensional experimental modal analysis is also conducted on the water-filled cylindrical shell to determine structural parameters used to extract these levels.

The cylinder's radial vibration response for certain lightly damped modes is used to determine TBL surface pressure at lower streamwise wavenumbers than previously reported ($k_1/k_c < 0.01$). The nearly constant low wavenumber pressure level determined from these measurements is roughly 40 dB below the convective peak level. This level falls midway between the Smol'yakov (2006) and Chase (1987) TBL models and is roughly 25 dB lower than the Corcos (1964) model. The current data is a few decibels below the lower bound of related measurements in air by Farabee and Geib (1975) and Martin and Leehey (1977). Simple wavenumber white forms for the TBL surface pressure spectrum at low wavenumber are discussed.

Low wavenumber fluctuating shear stress levels in both the cross-flow and streamwise directions are determined using directionally uncoupled low-order cylinder modes in the circumferential and axial directions. This data addresses a critical gap in

available literature regarding experimental low wavenumber shear stress data. The low wavenumber shear stress levels in both the cross-flow and streamwise directions are determined to be roughly 10 dB higher than those of normal pressure. As is the case for various models of TBL pressure, these measurements suggest that a nearly constant value for normalized shear stress at low wavenumber is valid over a broad range of frequencies. The same wavenumber white model forms suggested for low wavenumber TBL surface pressure are also appropriate for shear stress.

TABLE OF CONTENTS

LIST OF FIGURES

LIST OF TABLES

ACKNOWLEDGEMENTS

including, technicians, staff assistants, and engineers makes working in the Water Tunnel at ARL a privilege.

To my wonderful wife, Linda, and beautiful children: Daniel, Lauren, Kristina, and Rebecca, I owe all my love and gratitude. They made untold sacrifices, because of their love for me, for which I am forever grateful. Thank you. Finally, I give honor and praise to God (Father, Son, and Spirit) who has given me comfort in the midst of doubt, and humility in the midst of believing I had solved the mysteries of this remarkable world He created.

Chapter 1

INTRODUCTION

1.1   Background

As a boundary layer develops and grows in the fluid near the surface of a moving

vehicle (or flow over a stationary body), turbulent eddies of varying scales are generated

due to the shearing of the fluid layers within the boundary layer moving at different

velocities. These eddies decay and regenerate over a relatively short distance, are

correlated over a limited region, and cause velocity fluctuations throughout the boundary

layer. The integrated effect of these velocity fluctuations produces fluctuating pressures

and fluctuating shear stress on the surface of the underlying structure as depicted in

Figure 1.1.

Fluctuating pressures and shear stress, correlated over some surface area, generate

fluctuating forces that can radiate sound directly and can also excite the underlying

structure producing undesirable vibration and noise. Past research has demonstrated the

significance of this phenomenon in generating interior aircraft cabin noise (Graham,

1977). Naval researchers are also interested in understanding and mitigating the vibration

and acoustic radiation of marine vehicles (Blake, 1986, Leehey, 1988, Ko, 1993). The

pressures themselves can interfere with a ship or submarine sonar system's ability to

detect incoming acoustic pressures from farfield sources. The forces associated with

boundary layer surface pressures and shear stress can also cause vibration and noise in

common piping systems (Chase, 1980,1993).

Although the response of structures excited by turbulent boundary layers has received significant attention for nearly fifty years, important questions still remain. Among these questions are the details of how energy in a turbulent boundary layer is distributed in the wavenumber domain such that some is rejected by the underlying structure and some couples to the structure causing unwanted vibration and sound. Unsteady wall pressure has received the bulk of the attention, while unsteady wall shear stress has received significantly less attention until roughly 20 years ago.

Most of the energy in a turbulent boundary layer is contained at wavenumbers associated with the eddy convection velocity, $k_c = \omega/U_c$, where k_c is the convective wavenumber, ω is radian frequency, and U_c is the convection velocity or average speed at which eddies travel (roughly 60% – 70% of the freestream velocity or vehicle speed). Figure 1.2 shows a schematic of the TBL streamwise wavenumber spectrum and the strong peak at the convective wavnumber. For the relatively high Mach number flow associated with aircraft cabin noise, convective wavenumbers in the flow tend to match wavenumbers of the bending waves in the underlying structures (aerodynamic coincidence). Therefore, wavevector-frequency models of the surface pressure that accurately represent the convective wavenumber portion of the TBL spectrum can be reliably used to study aircraft cabin vibration and noise.

For the low Mach number flow associated with marine applications, convective wavenumbers are too high to match those of the bending waves in the underlying structure and therefore do not cause significant vibration. The structural wavelengths of interest lie in the low wavenumber portion of the surface pressure spectrum (defined as the region above the acoustic wavenumber, $k_0 = \omega/c_0$, and below the convective

wavenumber, $k_c = \omega/U_c$). Although past investigations (Chase, 1987, Smol'yakov, 2006) have shown that the low wavenumber pressure levels in undisturbed flow are roughly $1/100^{th}$ of the convective wavenumber levels (40 dB below), these low wavenumber pressures are responsible for structural vibration and sound. Therefore the wavevector-frequency models of the surface pressure used in marine applications must accurately represent the low wavenumber portion of the TBL spectrum. However, because the levels are so low relative to the convective waveumber pressures, they have historically been very difficult to measure and model correctly. A review of the extensive literature in the area of TBL wall pressures reveals a general lack of measured wall pressures at especially low wavenumbers ($k_1/k_c < 0.01$). Particularly difficult to measure are the TBL wavenumber components of surface pressure below the acoustic wavenumber which radiate sound directly.

Mathematical models of TBL wall pressure and shear stress take the form of a statistical space-time correlation function, and its corresponding Fourier transform or wavevector-frequency spectrum. Several empirical models of TBL surface pressure have been developed over the years and used for various applications. Initially these models were based on direct two-point cross-correlation and cross-spectrum measurements (Maidanik, 1967). However, these two-point measurements did not adequately characterize the low wavenumber TBL surface pressure levels. More sophisticated measurement techniques, better able to filter out the convective wavenumbers, led to better low wavenumber data and ultimately more sophisticated TBL models (Chase, 1980). Despite continued interest and research in this area there is still uncertainty and even controversy about low wavenumber excitation of structures from TBL sources.

A review of some highlights of research in this field carried out over the past fifty years is provided in the next section.

1.2   Review of Related Literature

1.2.1   TBL Unsteady Wall Pressure

The first quality two-point, cross-correlation measurements of wall pressure were obtained by Willmath and Wooldridge (1962), which showed that pressure fluctuations convect with the flow at a frequency dependent mean convection velocity. Corcos (1964) used these measurements, and those by Bakewell, *et. al.* (1962) in fully developed pipe flow, as the basis for an early form of a TBL surface pressure model. He proposed a separable form for the cross-spectral function of pressure on the surface below spatially homogenous boundary layer turbulence. The separable function includes factorable terms of the surface pressure autospectrum, $\phi(\omega)$, exponentially decaying terms involving non-dimensional streamwise and cross-flow separation distances, and an oscillating or propagating function of non-dimensional separation distance in the flow direction. A straightforward Fourier transformation of the cross-spectrum to the wavenumber domain yields the surface pressure wavevector-frequency spectrum. The spatial and temporal separability of the cross-spectrum enables the frequency spectrum and wavenumber spectrum to be evaluated independently. The wavevector spectrum is notably flat very near zero wavenumber. Because of its simplicity and early widespread use, the Corcos model is still used for certain applications and is often the standard by which other surface pressure models are compared. While this model has shown remarkable utility, it is widely accepted that the low wavenumber levels overestimate actual surface pressure

levels. Modifications to the original Corcos model have been proposed by others attempting to better match the low wavenumber levels to available data.

Chase (1980) proposed another popular TBL surface pressure model based on the relationship between the velocity field and fluctuating pressures from the Poisson equation. Chase intended to model the entire hydrodynamic domain ($k >> k_0$) and address the low wavenumber limitations of the Corcos model. Chase cast his model directly in the wavenumber domain, consequently there is no simple inverse Fourier transformation to get a cross-spectral density function. Also, in contrast to the Corcos model, the Chase model is non-separable in frequency and wavevector. Chase did however propose a nearly separable form of his wavevector-frequency spectrum, which can be integrated over wavenumber to provide an exact form for the wall pressure autospectrum. This point pressure spectrum is valid over a broad range of frequencies at high Reynolds number, and is still used as cited in an approximate form by Howe (1998). The point pressure spectrum does not contain the viscous subrange so its use is limited to high Reynolds number and low reduced frequencies. The Chase point pressure model can be modified to account for the viscous subrange of measured data at high frequencies.

Chase suggested contributions to the wall pressures come from the velocity product of two sources identified in the Poisson equation: 1) the interaction of the turbulence velocity and mean shear and 2) the interaction between turbulent eddies. The mean shear sources dominate pressures in the convective domain while the pure turbulence sources dominate pressures in the low wavenumber domain. Chase utilized available low wavenumber data and flow field data (principally from pipe flow measurements in air) to determine several empirical coefficients required for his model.

Guided by theoretical arguments of Kraichnan (1956) and Phillips (1956), the original Chase model goes to zero very near zero wavenumber in contrast to the Corcos model which remains essentially constant near zero wavenumber. Chase offered improvements to the original model (1980) with the addition of terms accounting for the acoustic domain (1987) and rotational or viscous contributions (1992). Chase (1991a) presented two forms (one separable and one non-separable) for the wall pressure spectrum to include wavenumber white levels. He later suggests this may be superseded by viscous contributions and concluded the rotational effects would likely dominate surface pressure levels near zero wavenumber. This renders the Kraichnan and Phillips theoretical arguments for incompressible, inviscid flow essentially moot (arguments suggesting the wall pressure should go to zero at zero wavenumber). While the Chase model addresses some of the low wavenumber limitations of the Corcos model, it lacks experimental validation in the acoustic domain and the lowest hydrodynamic wavenumbers.

A recent comprehensive wavevector-frequency model (and cross-spectral density function) of TBL surface pressure is reported by Smol'yakov (2006). This model is a generalization and extension of an earlier model proposed by Smol'yakov and Tkachenko (1991). The revised model includes a dependence on Reynolds number and accounts for the effects of viscosity not included in the original 1991 model. Like the Corcos model, the Smol'yakov (2006) model contains separable functions of time and spatial separation and can be easily transformed between the cross-spectrum and the wavevector-frequency spectrum. The wall pressure frequency autospectrum accompanying this model was

proposed by Smol'yakov (2000). This frequency spectrum contains four characteristic frequency regions which vary in importance as a function of Reynolds number.

Helpful summaries of TBL excitation and radiation were published by Leehey (1988), Bull (1996), and Graham (1997). Leehey (1988) addressed several practical unresolved questions regarding structural excitation and sound radiation and discussed various complicating factors. He suggests the wavenumber spectrum near the acoustic wavenumber and below is largely conjectural. Bull (1996) provides a theoretical summary of the statistical description of TBL wall pressure and a review of historical modeling efforts. Graham (1997) also reports and compares several TBL surface pressure models including those of Ffowcs Williams (1982) and Efimtsov (1982). Common to all models of TBL pressure is the peak in the wavenumber spectrum at the convective wavenumber. Essentially all TBL pressure models contain similar character in the convective peak vicinity, however the discrepancy in the low wavenumber region, below the convective peak, is the source of some controversy. Theoretical arguments for incompressible, inviscid flow suggest a squared dependence on streamwise wavenumber, however most available data suggests a wavenumber "white" or flat streamwise wavenumber dependence.

Mapping out the entire TBL wavevector-frequency surface pressure spectrum experimentally has been difficult because of the difficulty in accurately measuring low wavenumber surface pressures. The shape of the wavenumber spectrum near the convective peak has been relatively well established from two-point, cross-spectral density measurements between flush mounted pressure transducers (Leehey, 1988). However, at large transducer separation distances, needed to resolve the low wavenumber

spectrum, these measurements are typically overwhelmed by convective pressures and cannot be reliably used. Several wavenumber filtering schemes have been implemented to filter out the convective and acoustic TBL pressures and to isolate low wavenumber pressures. Nearly all of this work has involved flow over smooth surfaces.

One class of low wavenumber measurements involves using surface pressure transducers to measure wall pressure directly. Maidanik (1967) proposed a wavenumber filtering scheme in which a streamwise array of flush mounted pressure sensors with appropriate sensor size and separation distance are summed with alternate phasing to determine pressure levels at discrete wavenumbers and frequencies. This method was implemented by Blake and Chase (1971) and Farabee and Geib (1975) in air using four and six sensor arrays respectively. The method is fairly effective at filtering out background noise present in the acoustic domain, but is less effective at filtering out convective pressures. More recent direct measurements of pressure were conducted by Manoha (1996) and Abraham and Keith (1998) in water using large sensors arrays of 32 and 48 sensors respectively. A spatial Direct Fourier Transform was applied to the measured data to extract the entire streamwise wavenumber spectrum. Aliasing and leakage effects limited the low wavenumber filtering to roughly 30 dB below the convective peak.

The second class of filtering methods involves measuring the vibration response of a structure subjected to TBL excitation to indirectly determine the low wavenumber level of TBL pressure. This indirect measurement scheme is often termed an "inverse method" and utilizes the filtering effects of a flexible structure to isolate low wavenumber pressures. This method more successfully filters out convective

wavenumbers, but can be somewhat less successful at rejecting background noise contaminating the acoustic wavenumber domain. Jameson (1975) first reported the results from measurements in air over a flat plate using this technique. Data measured by Martin and Leehey (1977) using a membrane in air is frequently cited as reliable low wavenumber data. The inverse method focuses on measuring the peak response of individual structural modes. The vibration response can be related to the modal force exciting the structure and the modal force can in turn be related to the TBL wavevector-frequency spectrum (Hwang and Maidanik, 1990).

To determine the modal force spectrum of TBL excitation, one must know the wavenumber dependence of the structure's response as well as an estimate of the TBL wavevector-frequency spectrum. The integrated product of these functions yields the modal force spectrum. For relatively simple geometries and boundary conditions, analytic solutions exist for the structural response functions. The peak in structural response of low-order modes occurs at lower wavenumbers; the peak in structural response of high order modes occurs at higher wavenumbers.

1.2.2 TBL Unsteady Wall Shear Stress

To this point the review of related research has been limited to the modeling and measurement of fluctuating pressures normal to the wall surface, which is where nearly all research in this field focused prior to the late 1980's and early 1990's. The majority of work was based on the assumption of inviscid flow and that the effect of fluctuating shear stress is negligible in most situations. However, a research emphasis began to emerge

with the goal of understanding the role of fluctuating shear stress on structural excitation, vibration, and radiation.

Howe (1979) investigated fluctuating shear stress in a turbulent boundary layer and associated noise. Hariri and Akylas (1985) computed the dominant contribution of shear stress dipoles (from viscous effects) to the radiated pressure field and the corresponding low wavenumber region of wall pressures for low Mach number and large Reynolds number flow. They concluded that dipole sources contribute to sound generation, but for typical values of Mach number and Reynolds number, the viscous dipole contribution is small compared with that of the inviscid quadrupole sources from normal pressures.

Chase (1991b) investigated the roll of rotational effects (viscosity) on both wall pressure and the flow-aligned wall shear stress in the low wavenumber domain. He concludes these effects may well dominate the irrotational non-viscous effects for both pressure and shear stress and suggests the results support the necessity for considering fluctuating wall shear stress along with pressure for various applications. Chase (1992) further proposes estimates for the rotational and irrotational forms of pressure and shear stress. This leads to a revised model (Chase, 1993) of the wall pressure and a related trial model of the flow-aligned wall shear stress wavevector-frequency spectrum. The Chase (1993) model of streamwise shear stress indicates low wavenumber levels of shear stress are roughly comparable to those of wall pressure.

Compared to the large number of experimental TBL wall pressure investigations, only a few experimental studies of fluctuating wall shear stress have been conducted. Measurements of TBL wall pressure are relatively easy and have become common place.

Fluctuating wall shear stress measurements require completely different sensors and instrumentation and are much more difficult to conduct. Of the limited experimental studies, most have focused on measuring the streamwise point frequency spectrum and associated convection velocity. Little or no attempt has been made to measure the streamwise shear stress wavenumber dependence or components of the cross-flow wavevector-frequency shear stress spectrum.

Keith and Bennett (1991) used hot-film probes in a water tunnel to measure and report one of the earliest empirical assessments of the shear stress frequency spectrum. They reported spectral levels of the wall shear stress as 18-24 dB below the wall pressure frequency spectrum for a limited range of Reynolds numbers, but acknowledge some absolute level limitations due to uncertainties in calibrating the hot-film transducers.

Measurements by Hespeel, *et. al.* (1998) using hot-film sensors were used to determine several parameters of the flow-aligned shear stress in a wind tunnel. These parameters include convection velocity, streamwise and spanwise cross-spectral density functions, and the streamwise wavenumber spectrum. These results suggest the streamwise shear stress wavenumber spectrum levels are roughly 20 dB below the corresponding pressure levels at convective wavenumbers. The low wavenumber shear stress levels are similar to the levels of wall pressure estimated by the Chase (1991) model suggesting the viscous contribution to wall pressure may be important at low wavenumber.

Khoo, *et. al.* (2001) conducted experiments in turbulent-channel flow and flat-plate boundary layer flow (open-circuit wind tunnel) using near wall hot wire probes. The probability density functions for the streamwise wall shear stress fluctuations and

streamwise velocity fluctuations were measured and reported. The normalized frequency spectrum of wall shear stress is compared to measurements of Keith and Bennett (1991). While the spectral character is similar, the Khoo, *et. al.* levels are roughly 10 dB higher than the reported Keith and Bennett data. Khoo, *et. al.* suggest this discrepancy is likely due to the use of hot-film elements by Keith and Bennett which result in severe spatial resolution problems combined with a relatively low measured wall-shear stress intensity.

Colella and Keith (2003) measured wall shear stress fluctuations in an external boundary layer on a towed vertical flat plate in water using an array of flush-mounted hot film sensors. They also measured streamwise velocity fluctuations and reported correlations between velocity and shear stress. From measured wall shear stress fluctuations, they report the probability density function, convection velocity ($U_c/U_0 = 0.45 – 0.55$), and non-dimensional frequency spectrum. The reported frequency spectrum is consistent with Khoo, *et. al.* (2001) at low reduced frequencies when scaled on outer variables, but is 10 dB above the Keith and Bennett (1991) data.

Several Direct Numerical Simulation (DNS) studies of wall shear stress in turbulent channel flow have been conducted in recent years at very low Reynolds number. Jeon, *et. al.* (1999) computed the convection velocities, frequency spectra, and wavevector spectra for pressure and shear stress (both streamwise and cross-flow) for channel flow at a Reynolds number based on the wall shear velocity and channel half-width of 180. Hu, *et. al.* (2001) computed similar quantities (streamwise shear stress only) for Poiseuille and Couette flow at three Reynolds numbers including the Jeon, *et. al.* (1999) condition. Abe, *et. al.* (2004) conducted a study similar to Jeon, *et. al.* (1999)

with similar results, but with an emphasis on describing the inner and outer layer flow-field structures which contribute to wall pressure and shear stress. Computed frequency spectra from Jeon, *et. al.* (1999) show reasonable agreement with results from other numerical studies and the limited experimental data from Keith and Bennett (1991). They conclude no self-similar behavior or universal functions exist for the normalized wavevector shear stress spectra as many suggest it does for pressure. Hu, *et. al.* (2001) report finite values for pressure and shear stress near zero wavenumber and wavenumber spectra very similar to one another. These studies report the convection velocity for pressure (0.7-$0.8U_0$) exceeds the convection velocity for shear stress (0.5-$0.6U_0$). The wavevector spectral results and convection velocities reported from these DNS studies are presented without comparison to experimental results because of the lack of corresponding data.

1.3   Dissertation Objectives

A review of the extensive literature in the area of TBL wall pressures and shear stress reveals at least two specific deficiencies this research desires to address. The first is a general lack of measured wall pressures at especially low wavenumbers specifically of the high quality obtained using inverse measurement techniques (Martin and Leehy, 1977). The second is the near complete absence of wavenumber shear stress measurements of any kind.

Most measurements of low wavenumber TBL wall pressure have been made in air at relatively high Mach numbers over smooth surfaces. However, making these measurements in water has some distinct advantages since measurements can be made at

lower Mach number extending the low wavenumber region of the wall pressure spectrum. The higher speed of sound in water shifts the acoustic wavenumber downward and the lower practical speeds of vehicles (and measurement facilities) shifts the convective wavenumber upward. This broadens the low wavenumber range at both ends. Also, the higher density of water generates higher surface pressures (even at low speeds), which increases the signal to noise ratio. Also, measurements in water allow for using the hydrostatic head of water to drive flow through a test-section eliminating the need for noisy fans or pumps. This significantly reduces the facility background vibration and noise, which traditionally limits getting uncontaminated low wavenumber pressure data. Figure 1.3 shows the relationship between several TBL surface pressure models at low wavenumber and representative available data from which current models are based. It also indicates the low wavenumber region in which this work intends to contribute additional data where it currently does not exist.

Inverse measurements of TBL pressures using flow past flat plates or membranes have yielded high quality low wavenumber data in the past. The dynamic response of plates and membranes is not coupled in the three coordinate directions; therefore, vibration response in the surface normal direction corresponds to excitation in only the surface normal direction. Since the dynamic response of a cylinder is coupled in all directions, measuring TBL excitation using flow through a cylinder allows one to assess shear stress (in-plane) contributions to structural excitation. Sorting out the excitation levels for each coordinate direction is possible because the relative contributions from each direction change with each shell resonance depending on the associated mode shape.

In this work, an experimental facility and measurement approach is developed and presented for measuring low wavenumber TBL fluctuating pressures and shear stress in water over a smooth surface. This work extends earlier work utilizing inverse measurement schemes. By measuring the vibration of a structure subjected to TBL excitation, one can inversely determine the low wavenumber pressure and shear stress required to generate the structural response. In the present case, a thin cylindrical shell is subjected to excitation from internal fully developed pipe flow in water, and wall pressures are presented at lower streamwise wavenumbers than previously reported ($k_1/k_c < 0.01$). The experimental methodology presented capitalizes on the advantages of making measurements in water rather than air, using a quiet hydrostatically driven flow facility with no moving mechanical parts, and using a directionally coupled structural filter (cylinder) rather than an uncoupled flat plate or membrane. The specific goals of this work are to: 1) measure and report TBL wall pressure and shear stress at lower wavenumbers than have previously been reported, and 2) use these measurements to evaluate and suggest improvements to existing empirical wall pressure and shear stress wavevector-frequency models.

This research extends the existing database of low wavenumber TBL wall normal pressures and fills a critical need for low wavenumber shear stress data. The shear stress data is particularly relevant for the study of marine vehicle excitation since most underwater vehicles have curved surfaces where shear stress excitation couples to flexural vibration and therefore can generate radiated noise. The mechanism of shear stress excitation has traditionally been neglected when evaluating vehicle noise.
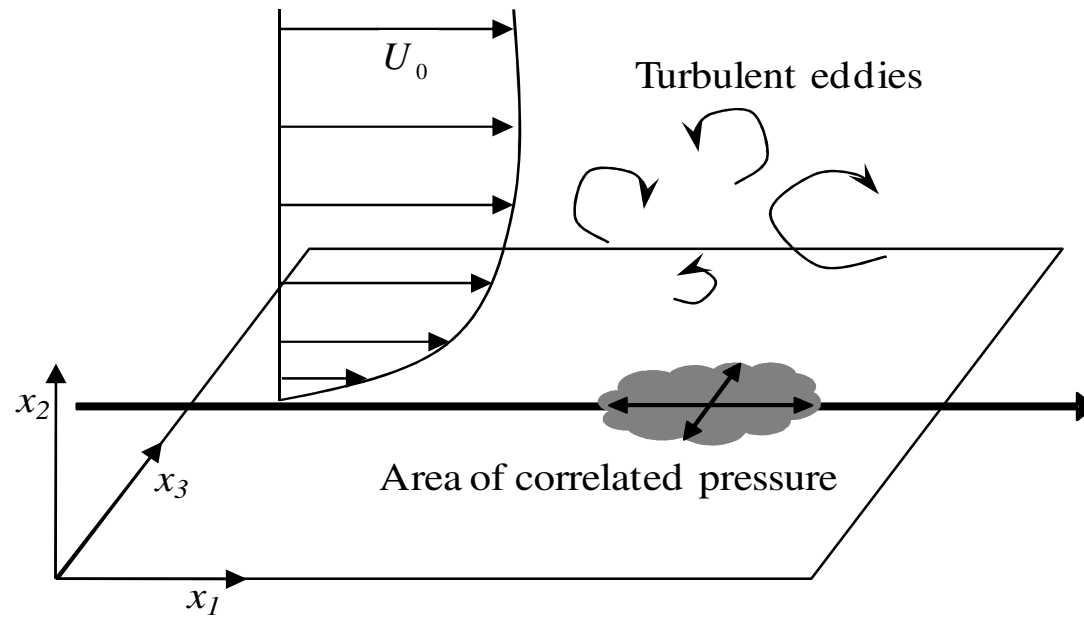
Figure 1.1 Wall pressure and wall shear stress from boundary layer turbulence over a surface

Figure 1.2 Schematic of TBL wall pressure wavenumber spectrum
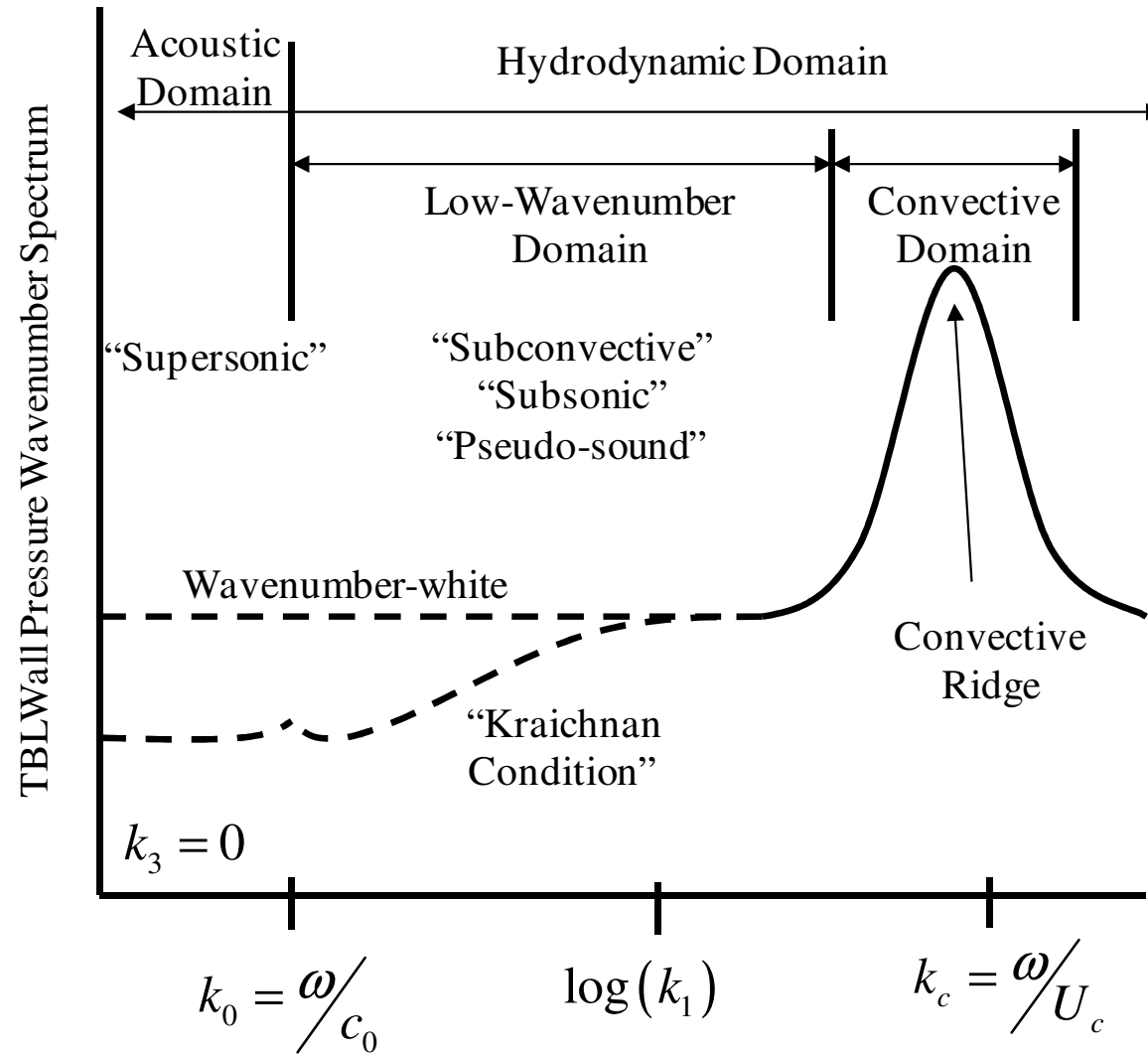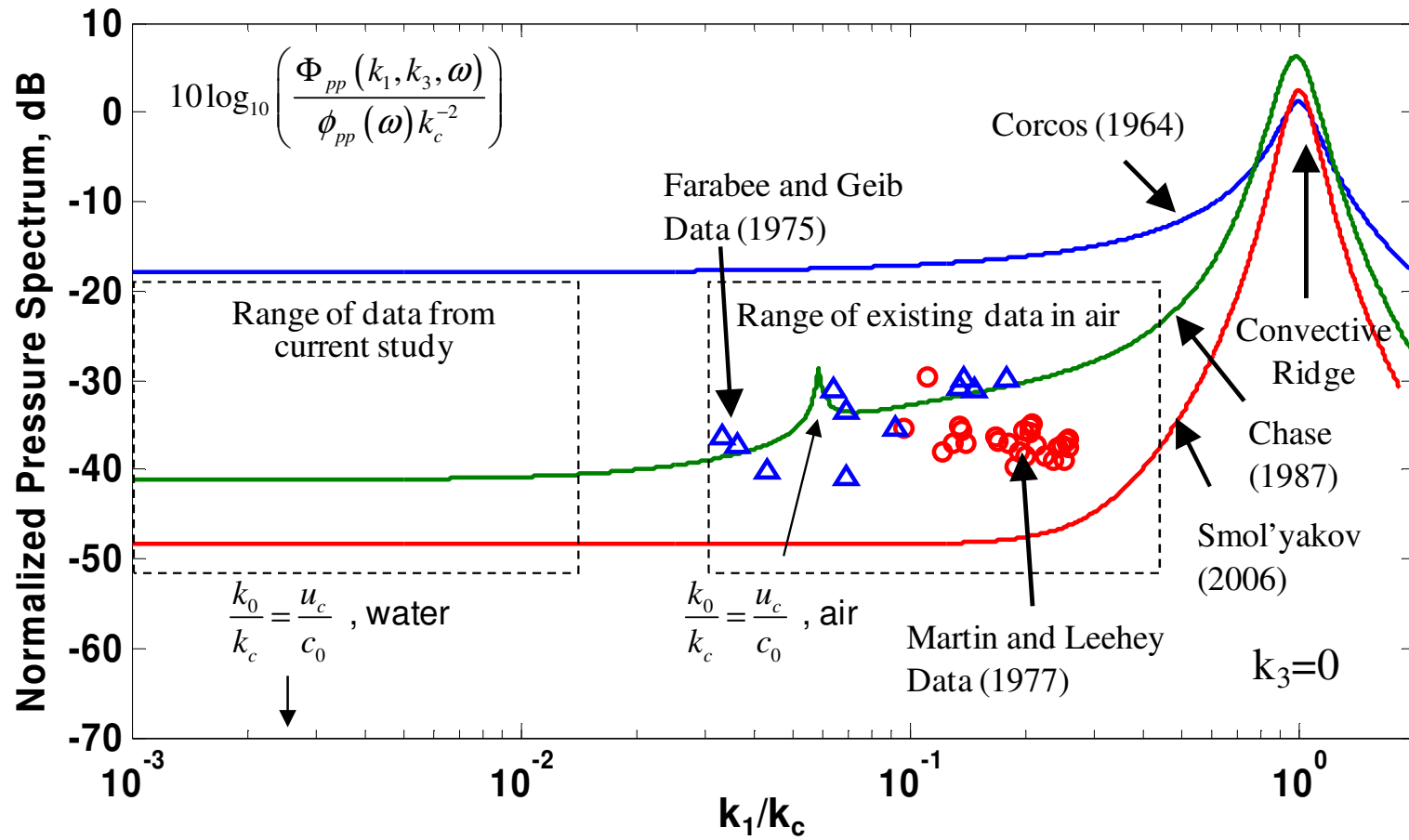
Figure 1.3 Representative TBL surface pressure wavenumber models and historical low wavenumber data

Chapter 2

MATHEMATICAL FORMULATIONS

2.1   TBL Wall Pressure and Shear Stress Models

On the surface of a structure beneath a locally homogeneous turbulent boundary

layer, the correlation between fluctuating pressure, p, at a point, x_1, x_3, and time, t, and

a second point separated from p in space and time by ξ_1, ξ_3, and τ respectively can be

represented with a statistical space-time correlation function (Bull, 1996),

$$R(\xi_1, \xi_3, \tau) = \langle p(x_1, x_3, t) \, p(x_1 + \xi_1, x_3 + \xi_3, t + \tau) \rangle, \tag{2.1}$$

where the brackets, $\langle \ \rangle$, represent an ensemble average. Its corresponding Fourier

Transform, or wavevector-frequency spectrum, is

$$P(k_1, k_3, \omega) = \frac{1}{(2\pi)^3} \int_{-\infty}^{\infty} \int_{-\infty}^{\infty} \int_{-\infty}^{\infty} R(\xi_1, \xi_3, \tau) e^{-i(k_1\xi_1 + k_3\xi_3 + \omega\tau)} d\xi_1 d\xi_3 d\tau. \tag{2.2}$$

The streamwise variables in Equations 2.1 and 2.2 are x_1, ξ_1, k_1 and the cross-flow

variables are x_3, ξ_3, k_3.

The single point frequency spectrum of wall pressure is related to the wavevector-

frequency spectrum by

$$\phi(\omega) = \int_{-\infty}^{\infty} \int_{-\infty}^{\infty} P(k_1, k_3, \omega) \, dk_1 dk_3. \tag{2.3}$$

and the mean square pressure fluctuation $\langle p^2 \rangle$, is given by

$$\left\langle p^2 \right\rangle = \int_{-\infty}^{\infty} \phi(\omega) d\omega. \tag{2.4}$$

A partial Fourier Transform of the space-time correlation function yields the pressure cross-spectrum, $\Gamma(\xi_1, \xi_3, \omega)$, where

$$\Gamma(\xi_1, \xi_3, \omega) = \frac{1}{2\pi} \int_{-\infty}^{\infty} R(\xi_1, \xi_3, \tau) e^{-i\omega\tau} d\tau. \tag{2.5}$$

The Corcos (1964) model of wall pressure below spatially homogenous boundary layer turbulence was originally proposed in a separable form of the cross-spectrum,

$$\Gamma(\xi_1, \xi_3, \omega) = \phi(\omega) f(\xi_1, \xi_3) = \phi(\omega) f_1(\xi_1 k_c) f_3(\xi_3 k_c). \tag{2.6}$$

Independent functions of frequency and spatial separation were suggested as

$$\Gamma(\xi_1, \xi_3, \omega) = \phi(\omega) e^{-\alpha_1 |\xi_1 k_c|} e^{-\alpha_3 |\xi_3 k_c|} e^{i\xi_1 k_c} \tag{2.7}$$

where $\alpha_1 = 0.11, \quad \alpha_3 = 0.7$ are the exponential decay constants usually assumed for smooth walls. The separable cross-spectrum includes factorable terms of the surface pressure frequency spectrum, exponentially decaying terms involving the non-dimensional separation distances, and an oscillating or propagating function of non-dimensional separation distance in the flow direction.

As a result of many years of additional research (Hwang, *et. al.*, 2008, Lysak, 2006, Goody, 2004, Smol'yakov, 2000), the point wall pressure frequency spectrum, $\phi(\omega)$, can be characterized by four characteristic frequency regions illustrated in Figure 2.1: 1) the low frequency region where levels increase as roughly ω^2, 2) the spectral peak region, 3) the inertial subrange, universal range, or scale independent range where levels are roughly $\phi(\omega) \approx 1\rho^2 u_t^4 \omega^{-1}$, and 4) the high frequency or viscous subrange which

exhibits a roughly exponential roll-off from the universal range. These frequency regions vary in importance as a function of Reynolds number. The low frequency levels of measured point surface pressure data collapse when scaled on outer variables of boundary layer displacement thickness, δ^*, and freestream velocity, U_0. The high frequency levels collapse when scaled on the inner variables of ν/u_τ and u_τ, where ν is kinematic viscosity and u_τ is friction velocity. The universal range or scale independent range collapses using either inner or outer variables.

A straightforward spatial Fourier transformation of a separable pressure cross-spectrum yields a separable form of the surface pressure wavevector-frequency spectrum where

$$P\left(k_1,k_3,\omega\right)=\phi\left(\omega\right)F(k_1,k_3)\,. \tag{2.8}$$

Hwang and Maidanik (1989) suggest a helpful non-dimensionalization such that

$$P\left(k_1,k_3,\omega\right)=\phi\left(\omega\right)F\left(\boldsymbol{k}\right)=\phi\left(\omega\right)k_c^{-2}G\left(\boldsymbol{k}/k_c\right), \tag{2.9}$$

where $G\left(\boldsymbol{k}/k_c\right)=G_1\left(k_1/k_c\right)G_3\left(k_3/k_c\right)$ and $\int\limits_{-\infty}^{\infty}\int\limits_{-\infty}^{\infty}G\left(\boldsymbol{k}/k_c\right)\mathrm{d}^2\left(\boldsymbol{k}/k_c\right)=1$. The Corcos wavevector-frequency spectrum of TBL pressure non-dimensionalized in this manner becomes

$$\frac{P\left(k_1,k_3,\omega\right)}{\phi\left(\omega\right)k_c^{-2}}=\frac{\alpha_1/\pi}{\left[\alpha_1^2+\left(k_1/k_c-1\right)^2\right]}\frac{\alpha_3/\pi}{\left[\alpha_3^2+\left(k_3/k_c\right)^2\right]}, \tag{2.10}$$

where the wavevector spectra are two-sided in k_1 and k_3. A three-dimensional surface plot of the Corcos model (Equation 2.10) is shown in Figure 2.2. The convective peak is

evident at a non-dimensional streamwise wavenumber of one and the function is

symmetric about $k_3 = 0$ where the maximum values in the k_3 direction occur.

The non-separable TBL pressure model proposed by Chase (1987) directly in the

wavevector-frequency domain is given as

$$\frac{P(k_1, k_3, \omega)}{\phi(\omega) k_c^{-2}} = \frac{k_c^2}{\phi(\omega)} \frac{\rho^2 u_\tau^3 \delta^3}{\left[(k_+ \delta)^2 + \frac{1}{b^2}\right]^{5/2}} \times$$

$$\left[C_M (k_1 \delta)^2 \frac{k^2}{\left|k^2 - k_o^2\right| + \varepsilon^2 k_o^2} + C_T (k \delta)^2 \frac{(k_+ \delta)^2 + \frac{1}{b^2}}{(k \delta)^2 + \frac{1}{b^2}} \times \right.$$

$$\left. \left(c_1 + c_2 \frac{\left|k^2 - k_o^2\right|}{k^2} + c_3 \frac{k^2}{\left|k^2 - k_o^2\right| + \varepsilon^2 k_o^2} \right) \right] \qquad (2.11)$$

where $\qquad k_+^2 = (\omega - U_c k_1)^2 / (h v_*)^2 + k^2, \quad k \equiv \sqrt{k_1^2 + k_3^2}$

$$h = 3.0, \quad b = 0.75, \quad \varepsilon = 0.2$$

and $\qquad C_M = 0.466/h, \quad C_T = 0.014/h$.

$$c_1 = 2/3, \quad c_2 = 1/6, \quad c_3 = 1/6$$

A three-dimensional surface plot of the Chase (1987) model is shown in Figure 2.3.

Values for the Chase model differ from Corcos near zero wavenumber where outside the

acoustic domain the levels are roughly 15 dB below Corcos and the value of the Chase

model at zero wavenumber is zero.

Although Equation 2.11 cannot be integrated over wavenumber analytically,

Chase proposed a nearly separable form of his wavevector-frequency spectrum, which

can be integrated to provide the two-sided wall pressure frequency spectrum,

$$\frac{\phi(\omega)}{\rho^2 U_\infty^3 \delta} = \left(\frac{u_\tau}{U_\infty}\right)^4 \frac{\left(\left(\frac{\omega\delta}{U_\infty}\right)^2 + \alpha_c^2\right)}{\left(\left(\frac{\omega\delta}{U_\infty}\right)^2 + 1\right)^{1.5}}, \tag{2.12}$$

where $\alpha_c = 0.2$ which controls the low frequency level and slope. This point pressure

frequency spectrum is valid over a broad range of frequencies at high Reynolds number

and includes the first three regions of Figure 2.1, but does not contain the viscous

subrange (region 4 in Figure 2.1). Howe (1998) reports a useful approximate form to the

Chase frequency spectrum using boundary layer displacement thickness, δ^*, rather than

boundary layer thickness, δ. This frequency spectrum yields a true ω^2 dependence at low

frequencies (region 1 in Figure 2.1) and is given as

$$\frac{\phi(\omega)}{\rho^2 U_\infty^3 \delta^*} = \left(\frac{u_\tau}{U_\infty}\right)^4 \frac{\left(\frac{\omega\delta^*}{U_\infty}\right)^2}{\left(\left(\frac{\omega\delta^*}{U_\infty}\right)^2 + \alpha_p^2\right)^{1.5}}, \qquad \text{where } \alpha_p = 0.12. \tag{2.13}$$

Since neither of these models are valid at high frequency, an exponential decay factor,

$\exp\left(-2.2\left(\omega v / u_\tau\right)\right)$, can be appended to either Equation 2.12 or 2.13 to account for the

viscous subrange of measured data at high frequencies. This factor comes from a curve fit

of wall pressures computed at several Reynolds numbers produced by modeling the

turbulent velocity spectrum for fully developed pipe flow, Lysak (2006).

The separable wavevector-frequency model of TBL surface pressure by

Smol'yakov (2006) is given as

$$\frac{P(k_1,k_3,\omega)}{\phi(\omega)k_c^{-2}} = \frac{k_c^2}{2\pi}\left\{\frac{h\Lambda_1\Lambda_3}{\left[\left[1+\left(\frac{\Lambda_1\omega}{U_c}-\Lambda_1 k_1\right)^2+\left(\Lambda_3 k_3\right)^2\right]\right]^{3/2}} - \right.$$

$$\left. \frac{(h-1)l^2}{\left[1+\left(\frac{lm_1\omega}{U_c}-lk_1\right)^2+\left(lk_3\right)^2\right]^{3/2}}\right\} \qquad (2.14)$$

where
$$\Lambda_1 = U_c/(B\omega), \quad \Lambda_3 = U_c/(m_0 B\omega),$$

$$h = \left[1-m_1 B/\left(m_0 n^2 G^{1/2}\right)\right]^{-1},$$

$$l = (U_c/\omega)\left[n/(m_1 G)\right]^{1/2},$$

$$m_1 = \left(1+B^2\right)/\left(5n-4+B^2\right),$$

$$G = 1+B^2-nm_1,$$

$$m_0 = 6.45, \quad n = 1.005,$$

$$B = A/\left[1+SA\left(\omega v/u_\tau^2\right)\left(u_\tau/U_0\right)\left(U_0/U_c\right)\right],$$

$$A = 0.124\left\{1-0.25 U_c/\left(\omega\delta^*\right)+\left[0.25 U_c/\left(\omega\delta^*\right)\right]^2\right\}^{1/2},$$

and
$$S = 100.$$

Smol'yakov also presents a form for the convection velocity of wall pressure as

$$U_c/U_0 = 1.6\left(\omega\delta^*/U_0\right)/\left[1+16\left(\omega\delta^*/U_0\right)^2\right]+0.6, \qquad (2.15)$$

which is used in this work in calculations involving the Smol'yakov (2006) model. A three-dimensional surface plot of this model is shown in Figure 2.4. Values for the Smol'yakov model at $k_3 = 0$ are roughly 15 dB below the Chase (1987) model and the Smol'yakov model yields a true wavenumber white spectrum at low wavenumbers.

The wall pressure point frequency spectrum accompanying this model was proposed by Smol'yakov (2000). This model is normalized using inner variables and is given as

$$\frac{\phi(\omega)}{\rho^2 u_\tau^2 \nu} = 1.49 \times 10^{-5} R_\theta^{2.74} \bar{\omega}^2 \left(1 - 0.117 R_\theta^{0.44} \bar{\omega}^{1/2}\right) \qquad \text{at } \bar{\omega} < \bar{\omega}_0,$$

$$\frac{\phi(\omega)}{\rho^2 u_\tau^2 \nu} = 2.75 \bar{\omega}^{-1.11} \left\{1 - 0.82 \exp\left[-0.51\left(\bar{\omega}/\bar{\omega}_0 - 1\right)\right]\right\} \qquad \text{at } \bar{\omega}_0 < \bar{\omega} < 0.2,$$

$$\frac{\phi(\omega)}{\rho^2 u_\tau^2 \nu} = \left(38.9 e^{-8.35\bar{\omega}} + 18.6 e^{-3.58\bar{\omega}} + 0.31 e^{-2.14\bar{\omega}}\right)$$

$$\times \left\{1 - 0.82 \exp\left[-0.51\left(\bar{\omega}/\bar{\omega}_0 - 1\right)\right]\right\} \qquad \text{at } \bar{\omega} > 0.2, \qquad (2.16)$$

where Reynolds number based on momentum thickness, θ, is $R_\theta = U_0 \theta / \nu$, $\bar{\omega} = \omega \nu / u_\tau^2$, and $\bar{\omega}_0 = 49.35 R_\theta^{-0.88}$. Momentum thickness can be related to displacement thickness for a neutral pressure gradient over a smooth surface as roughly $\theta = 7/9 \delta^*$, (Schlichting, 1979).

A comparison of all previously mentioned models of point pressure frequency spectra are non-dimensionalized using outer variables U_0 and δ^* and shown in Figure 2.5. Spectra included in this plot are: the Chase (1980) model, the Howe modification to Chase (1980), the Howe modification with the exponential decay factor included, and the

Smol'yakov (2000) model. A point frequency spectral model of fluctuating shear stress

(discussed in the subsequent paragraphs) is also included for comparison.

The surface roughness of the wall over which a TBL resides is known to affect

the underlying wall pressure field (Blake, 1970, Howe, 1988). The pressure models

presented thus far, both point frequency spectra and wavevector spectra, have been

developed for TBL flow over smooth walls. Howe (1991) suggests the pressure field over

a rough wall comes from two sources: 1) increased turbulence production due to surface

roughness which results in increased convective pressures, and 2) the scattering of these

convective pressures by roughness elements and a redistribution of energy to low

wavenumbers. Appropriate values of friction velocity, u_τ, in the point frequency models

presented can be used to estimate the convective pressures due to increased turbulence

over rough walls. However, to capture the effect of surface roughness on low

wavenumber pressures, the wavevector models must appropriately represent the scattered

pressure field.

Howe (1991) presents a model of the scattered pressure field due to roughness at

low Mach number starting with the Chase (1987) model of Equation 2.11. In addition to

the two terms in Equation 2.11 accounting for mean shear, C_M, and pure turbulence, C_T,

Howe adds a third term, C_R, to account for the scattered pressure field. Howe (1988)

developed this term based on a theoretical analysis of hemispheres attached to a flat

surface to represent surface roughness. He used experimental data to determine

parameters reflecting the shape of this function, but could only establish a lower bound

for the level. The addition of this term to the Chase model increases pressure levels in the

low wavenumber region.

To account for roughness using the Corcos model of Equation 2.10, appropriate values for the convection velocity and decay constants, α_1 and α_3, can be used. Measurements by Blake (1970) suggest the decay rate in the flow direction, α_1, increases by a factor of three when changing from the smooth surface to the rough surfaces he tested. The cross-flow decay rate, α_3, remained nearly constant between his smooth and rough surfaces. Increasing the streamwise decay rate in Equation 2.10 has the effect of flattening out the wavenumber spectrum or lowering the convective peak level and increasing the surrounding levels. A factor of three increase for α_1 results in a 5 dB increase in the low wavenumber levels of the Corcos model. A question to be addressed is whether the increased streamwise decay rate measured above a rough surface represents the scattered pressure field modeled by Howe. It does have a similar effect of redistributing energy in the wavenumber domain from the convective peak region to lower wavenumbers as Howe suggests.

The Smol'yakov (2006) model is also examined for the possibility of accounting for roughness. The decay rates used in the Corcos model are found in the definition of correlation lengths, Λ_1 and Λ_3, in the Smol'yakov model of Equation 2.14. In this model, the variable B represents the streamwise decay rate and is defined as a function of friction velocity to account for viscosity. The product m_0B represents the cross-flow decay rate. Increasing the friction velocity in Equation 2.14 by a factor of two (or four) to represent its increase from a smooth to a rough surface has minimal effect on the low wavenumber Smol'yakov spectrum (less than 1 dB). In contrast, simply increasing the streamwise decay rate, B, by a factor of two results in an increase in the Smol'yakov low

wavenumber levels by nearly 30 dB. These levels seem unreasonably high, but additional work is needed to further evaluate this model for roughness effects. Using either a representative value for friction velocity in the definition of the streamwise decay rate or simply adjusting the decay rate itself does not appear to adequately account for surface roughness in the Smol'yakov model.

While surface roughness has been demonstrated to have a significant effect on the low wavenumber TBL wall pressure levels, a brief review of historical work in this area reveals a general lack of suitable modeling. Additional experimental research in this area would provide valuable data and could help lead to a practical understanding of roughness and the ability to predict its effect on TBL wall pressures. In this thesis, however, surface roughness is not considered further.

The interest in fluctuating wall shear stress, in addition to normal wall pressure, led to a semi-empirical wavevector-frequency model for shear stress proposed by Chase (1993). This model is given as

$$S\left(k_{1}, k_{3}, \omega\right) = \rho^{2} v^{3} S^{+}\left(k_{1+}, k_{3+}, \omega_{+}\right). \tag{2.17a}$$

where the subscript plus on a variable indicates it has been non-dimensionalized using inner variables u_{τ} and v. The normalized variables become

$$k_{1+} = k_{1} v / u_{\tau}, \quad k_{3+} = k_{3} v / u_{\tau}, \quad \omega_{+} = \omega v / u_{\tau}^{2}, \quad \delta_{+} = \delta u_{\tau} / v,$$

and

$$S^{+}\left(k_{1+}, k_{3+}, \omega_{+}\right) = B_{0} \omega_{+}^{-3/2}\left(1+m\omega_{+}\right)^{-n} \sum_{\pm}\left(K_{*\pm+}^{2} / \omega_{+}\right)^{-(r+3/2)}, \tag{2.17b}$$

where

$$K_{*\pm+}^2 = \left(\omega_+ - k_{1+}/\varepsilon\right)^2 / h^2 + k_{1+}^2 + \left(k_{3+} \pm \zeta_0 \omega_+^{1/2}\right)^2 + \alpha_0 \omega_+ + \left(\beta \delta_+\right)^{-2}. \tag{2.17c}$$

The empirical constants in Equations 2.17 are given by

$$\varepsilon = 0.11, \quad \zeta_0 = 0.1, \quad \alpha_0 = 0.11/4, \quad h = 2,$$
$$\beta = 0.11, \quad r = 2, \quad m = 3.5, \quad n = 4, \quad B_0 = 0.70 \times 10^{-4}.$$

A three-dimensional surface plot of the Chase (1993) shear stress model is shown in Figure 2.6. Values for this model are roughly 6 dB the below the Chase (1987) TBL pressure model at low wavenumber.

Analogous to the wall pressure frequency spectrum, the frequency spectrum of wall shear stress can be calculated using Equations 2.17 by

$$\phi_{ss}(\omega) = \int_{-\infty}^{\infty} \int_{-\infty}^{\infty} S(k_1, k_3, \omega) dk_1 dk_3. \tag{2.18}$$

The Chase (1993) frequency spectrum of the wall shear stress becomes

$$\frac{\phi_{ss}(\omega)}{\rho^2 u_\tau^4 \omega^{-1}} = 2 D_0 \varepsilon_0 \omega_+^{1/2} \left(1 + m\omega_+\right)^{-n} \left[\varepsilon_0^2 \omega_+ / h^2 + \alpha_0 + \left(\beta^2 \delta_+^2 \omega_+\right)^{-1}\right]^{-(r+1/2)}, \tag{2.19a}$$

where

$$D_0 = C_0 \pi^{1/2} \, \Gamma\left(1/2 + r\right) \big/ \Gamma\left(1 + r\right), \qquad C_0 = B_0 \pi^{1/2} \, \Gamma\left(1 + r\right) \big/ \Gamma\left(3/2 + r\right),$$

and
$$\varepsilon_0^2 = \left(h\varepsilon\right)^2 \big/ \left[1 + \left(h\varepsilon\right)^2\right]. \tag{2.19b}$$

As noted previously, this spectrum is included in Figure 2.5 for comparison with the pressure frequency spectra.

2.2 The Inverse Method for Measuring Low Wavenumber TBL Pressure

The inverse method for measuring low wavenumber TBL pressure and shear stress focuses on measuring the peak resonance response of individual structural modes to TBL excitation. This requires information about the structure's dynamic response. For a given structure, the transfer function, or the Frequency Response Function (FRF), between the displacement u at a point α and the force F at a point β for an individual mode n is given by Ewins (2001),

$$\frac{u_n(\alpha,\omega)}{F(\beta,\omega)} = \frac{1}{m_n} \frac{\psi_n(\alpha)\psi_n(\beta)}{\left[-\omega^2 + \omega_n^2 + i\eta_n\omega_n\omega\right]}. \tag{2.20}$$

The four modal parameters of each structural mode in Equation 2.20 are: angular resonance frequency, ω_n, loss factor, η_n, normalized structural normal mode shape function with a peak value of one, ψ_n, and the modal mass, m_n. The modal force F_n can be related to the force at point β by $F_n(\omega) = \psi_n(\beta)F(\beta,\omega)$. Therefore, displacement at a point on the structure is related to the modal force for a given mode by

$$u_n(\alpha,\omega) = \frac{1}{m_n} \frac{\psi_n(\alpha)F_n(\omega)}{\left[-\omega^2 + \omega_n^2 + i\eta_n\omega_n\omega\right]}. \tag{2.21}$$

The modal force can in turn be related to the TBL wavevector-frequency spectrum (Hwang and Maidanik, 1990) by

$$\left|F_n(\omega)\right|^2 = \int\limits_{-\infty}^{+\infty}\int P(k_1,k_3,\omega)\left|S_n(k_1,k_3)\right|^2 dk_1 dk_3 \tag{2.22}$$

where,

$S_n(k_1, k_3)$ is the sensitivity or filter shape function - a spatial transform of $\psi_n(x_1, x_3)$,

$$S_n(k_1, k_3) = \iint_A \psi_n(x_1, x_3) e^{ik_1 x_1} e^{ik_3 x_3} dx_1 dx_3 . \tag{2.23}$$

The measurement scheme for inversely determining low wavenumber TBL surface pressures and shear stress involves measuring the vibration response of a section of pipe (or a clamped cylindrical shell) to TBL pipe flow excitation in water and measuring the modal parameters of a water-filled cylindrical shell. A summary of the steps is outlined below.

1. The vibration response of a water-filled cylindrical shell subjected to TBL excitation at fully developed pipe flow conditions is measured.

2. Resonance frequency and damping for identified modes are extracted from the measured data in step 1.

3. A standard experimental modal analysis is conducted on the cylindrical shell filled with water to determine the spatial mode shapes and modal mass for each mode identified in step 2.

4. The normalized mode shapes of the cylinder are transformed to the wavenumber domain to determine the sensitivity functions from Equation 2.23.

5. A constant low wavenumber pressure spectrum level at and around the modal wavenumber is assumed and the modal force for each mode is computed through numerical integration using Equation 2.22.

6. The frequency response function for a single mode is combined with the modal force using Equation 2.21 and expected TBL induced cylinder vibration levels are computed.

7. The expected vibration levels (step 6) are compared with the measured vibration levels (step 1) to evaluate the accuracy of the assumed pressure spectrum levels.

8. Assumed low wavenumber TBL pressure levels are adjusted until they produce the measured vibration.

2.3   Analytical Cylindrical Shell Model

An analytical shell model is introduced here to provide analytic results for cylindrical shell dynamics and to help explain the role of the structure in determining the modal force when subjected to TBL flow. The analytical model, taken from Skelton and James (1997), is a fluid-loaded, simply-supported, shell using the Goldenveizer-Novozhilov cylindrical shell equations of motion. These equations apply for an isotropic, thin-walled (h<<a) cylinder in which rotational inertia and transverse shear effects are neglected. The simply-supported boundary conditions are defined in terms of cylindrical coordinates where points along the cylinder ends each possess six degrees of freedom: three degrees of translation along the coordinate axes, and three degrees of rotation about the coordinate axes. Two of the six degrees of freedom are fixed - translation in the radial and circumferential directions. Four of the six degrees of freedom are free - translation in the axial direction and rotation about all three coordinate axes. A diagram of the analytical shell model, variable definitions, and parameter values used for these calculations are shown in Figure 2.7.

The time-harmonic motion, spectral form of the equations become,

$$
\begin{bmatrix}
S_{11}(n,m) & S_{12}(n,m) & S_{13}(n,m) \\
S_{21}(n,m) & S_{22}(n,m) & S_{23}(n,m) \\
S_{31}(n,m) & S_{32}(n,m) & S_{33}(n,m)+f(n,m)
\end{bmatrix}
\begin{Bmatrix}
u_z(n,m) \\
u_\phi(n,m) \\
u_r(n,m)
\end{Bmatrix}
=
\begin{Bmatrix}
E_z(n,m) \\
E_\phi(n,m) \\
E_r(n,m)
\end{Bmatrix}
\qquad (2.24)
$$

where the dynamic stiffness matrix, *S*, is defined by:

$$
S_{11}(n,m) = E_1\left(\alpha_m^2 + n^2(1-v)/2a^2\right) - \omega^2 \rho_s h,
$$

$$
S_{12}(n,m) = -E_1(1+v)in\alpha_m/2a,
$$

$$
S_{13}(n,m) = -E_1 v\,\alpha_m/a,
$$

$$
S_{21}(n,m) = -S_{12}(n,m),
$$

$$
S_{22}(n,m) = E_1\left((1-v)\alpha_m^2/2 + n^2/a^2 + 2\alpha_m^2\beta^2(1-v) + \beta^2 n^2/a^2\right) - \omega^2\rho_s h,
$$

$$
S_{23}(n,m) = -E_1\left(i\,n/a^2 + i\beta^2(2-v)\alpha_m^2 n + i\beta^2 n^3/a^2\right),
$$

$$
S_{31}(n,m) = S_{13}(n,m),
$$

$$
S_{32}(n,m) = -S_{23}(n,m), \text{ and}
$$

$$
S_{33}(n,m) = E_1\left(1/a^2 + \beta^2 a^2 \alpha_m^4 + \beta^2 n^4/a^2 + 2\beta^2\alpha_m^2 n^2\right) - \omega^2\rho_s h,
$$

and $\alpha_m = m\pi/2L$. The excitation vector, *E* (in units of force per unit area), can be

specified as a distributed modal force, such as a unit force in the *r* direction,

$$
\begin{Bmatrix}
E_z(n,m) \\
E_\phi(n,m) \\
E_r(n,m)
\end{Bmatrix}
=
\begin{Bmatrix}
0 \\
0 \\
1/2\pi La
\end{Bmatrix},
\qquad (2.25)
$$

or a point force at a specific location (z_0, ϕ_0) in any direction,

$$
\begin{Bmatrix} E_z\left(n,m\right) \\ E_\phi\left(n,m\right) \\ E_r\left(n,m\right) \end{Bmatrix} = \begin{Bmatrix} F_z \cos(m\pi(z_0+L)/2L)e^{-in\phi_0} \big/ 2\pi La \\ F_\phi \sin(m\pi(z_0+L)/2L)e^{-in\phi_0} \big/ 2\pi La \\ F_r \sin(m\pi(z_0+L)/2L)e^{-in\phi_0} \big/ 2\pi La \end{Bmatrix}. \tag{2.26}
$$

Approximations to internal or external fluid loading (or both) can be included using the

term, $f\,(n,m)$ defined in terms of Bessel and Hankel functions,

$$
f_{int}\left(n,m\right) = -\rho\omega^2 \frac{J_{|n|}\left(\gamma_m a\right)}{\gamma_m J_{|n|}'\left(\gamma_m a\right)}, \qquad f_{ext}\left(n,m\right) = \rho\omega^2 \frac{H_{|n|}\left(\gamma_m a\right)}{\gamma_m H_{|n|}'\left(\gamma_m a\right)}, \tag{2.27}
$$

where $\gamma_m = \sqrt[+]{k_0^2 - \alpha_m^2}$, and $k_0 = \omega/c_0$ is the acoustic wavenumber of the fluid medium.

Knowing S and F, one can solve for the modal displacement, $u(n,m)$. From the modal

displacement, the spatial displacement, $u(\phi,z)$, can be obtained from the Fourier Series

expansions,

$$
u_z(\phi,z) = \sum_{m,n}^{\infty} u_z(n,m)\cos(m\pi(z+L)/2L)e^{-in\phi}
$$

$$
u_\phi(\phi,z) = \sum_{m,n}^{\infty} u_\phi(n,m)\sin(m\pi(z+L)/2L)e^{-in\phi} \tag{2.28}
$$

$$
u_r(\phi,z) = \sum_{m,n}^{\infty} u_r(n,m)\sin(m\pi(z+L)/2L)e^{-in\phi}.
$$

The cylindrical shell response functions or mode shapes include displacement in

all three coordinate directions: axial - z, circumferential - ϕ, and radial - r. The

displacements contain a sinusoidal dependence in the axial direction (m represents the

number of half wavelengths) and the circumferential direction (n represents the number

of full wavelengths). Shell curvature accounts for the coupling of displacement in all

three directions for all modes except the special case of $n=0$ or "breathing" modes. These

modes represent a different class of modes which are not fully directionally coupled.

Therefore, three distinct mode shapes exist for each *m,n* combination all occurring at

different resonance frequencies. In contrast, the higher order bending (*n*=1) and lobar

(*n*>1) modes are fully coupled and a unique mode or mode shape exists for each *m,n*

combination. Example mode shapes for each class of modes are shown in Figure 2.8.

The surface averaged radial accelerance for a radially applied unit modal input

force on the analytical water-filled cylindrical shell is shown in Figure 2.9. Resonance

peaks for several low-order modes, labeled with their corresponding mode order, are

evident in the plot in which resonance frequencies tend to increase with mode order.

Figure 2.10 shows the average radial cylinder accelerance in response to unit modal

excitation in all three coordinate directions from 0 - 5 kHz. These results indicate that

cylinder radial vibration is most responsive to radial excitation followed by

circumferential and then axial excitation for nearly all modes. Figures 2.11 and 2.12

indicate the same progression is also true for the cylinder response in the circumferential

and axial coordinate directions as well below 2000 Hz. In other words, a radial drive

generates the highest vibration levels in all three directions below 2000 Hz.

The exception to this observation is evident in the n=0 modal response which

occurs above 2000 Hz in the circumferential and axial directions. As mentioned

previously, three unique mode shapes and resonance frequencies exist for the n=0,m=1

mode order. Figure 2.9 shows the n=0, m=1 mode resonance in the radial direction near

750 Hz which has a very low peak amplitude relative to the surrounding modes. In

contrast, Figures 2.11 and 2.12 indicate the circumferential and axial n=0, m=1 modes

(near 2500 Hz and 4300 Hz, respectively) dominate the response spectra near their

resonance frequencies in their respective directions. As evident in these figures, both of these modes are preferentially excited by drives aligned in the corresponding coordinate direction and therefore represent an opportunity to evaluate the magnitude of the input force in their respective directions. The higher order n>1 modes identified in Figures 2.9 and 2.10 form the basis for determining the radial input force. The low-order n=0 modes prominent in Figures 2.11 and 2.12 form the basis for determining the axial and circumferential input forces.

The resonance peaks identified in Figures 2. 9 - 2.12 have corresponding mode shapes whose spatial Fourier transforms, or sensitivity functions, exhibit primary lobes (or lobe) in the wavevector domain. The peaks of these lobes represent points in the wavevector domain and therefore points corresponding to locations on the TBL wavevector spectrum. For example, the spatial Fourier transform of the lowest order $n=0$, $m=1$ mode shape results in a single primary lobe in the wavevector domain centered at $k_1=0$, $k_3=0$. For all higher order modes, this single peak splits and results in multiple primary lobes which move toward higher positive and negative wavenumbers. Higher order circumferential modes ($n>0$) shift the primary wavevector lobes along the cross-flow wavenumber axis (k_3) away from zero wavenumber. Higher order axial modes ($m>1$) shift the primary wavevector lobes along the streamwise wavenumber axis (k_1) away from zero wavenumber. By evaluating several cylinder vibration peaks and associated modes, a three-dimensional mapping of a portion of the TBL pressure spectrum can be achieved. Nearly all reported low wavenumber TBL data to date is given at $k_3 = 0$.

Figure 2.13 shows an example of the (3,1) mode shape and its corresponding spatial Fourier Transform. By comparing the peaks of the structural wavevector plots of Figure 2.13 and the TBL surface pressure plots of Figures 2.2-2.4, one can determine the portion of the TBL pressure spectrum to which this mode corresponds. Figure 2.14 further illustrates the filtering effect of a flexible structure to TBL pressures by showing the terms of Equation 2.22 for the (3,1) mode. The product of the sensitivity function and TBL spectrum provides the structural filtering effect and forms the integrand of the modal force spectrum. Figure 2.14 reveals a 70 dB convective ridge rejection for the (3,1) mode assuming a Corcos TBL spectrum.

Use of a cylindrical shell as the structural filter presents an opportunity to evaluate the TBL fluctuating shear stress in addition to normal pressure as has been done previously in inverse measurements of TBL excitation. For the cylinder under investigation, a radially applied force generates the highest cylinder vibration levels in all three coordinate directions for all higher order modes (n>1). These modes can be used to evaluate the magnitude of radial excitation. For the special case of the n=0 modes where directionally coupling does not occur, excitation in one direction produces a preferentially high response in the same direction. These modes are best suited to evaluate the magnitude of circumferential and axial shear stress excitation.
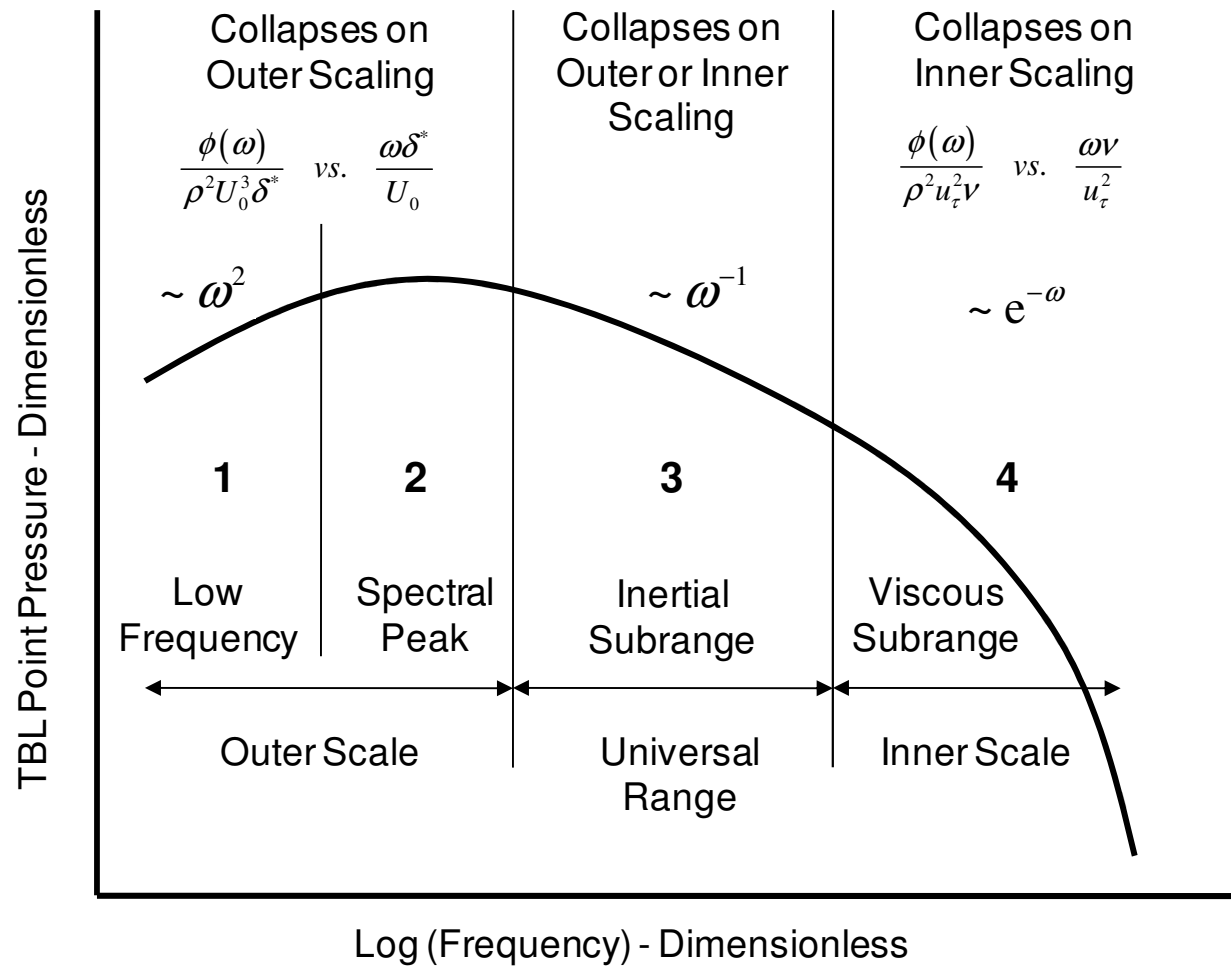
Figure 2.1 Schematic of TBL wall pressure frequency spectrum

$$10\log_{10}\left(\frac{P(k_1,k_3,\omega)}{\phi(\omega)k_c^{-2}}\right)$$

Corcos

Water at 6.1 m/s, 500 Hz

$\delta^* = 9.5$ mm, $u_\tau/U_0 = 0.032$

Normalized Pressure Spectrum, dB

k3/kc

k1/kc
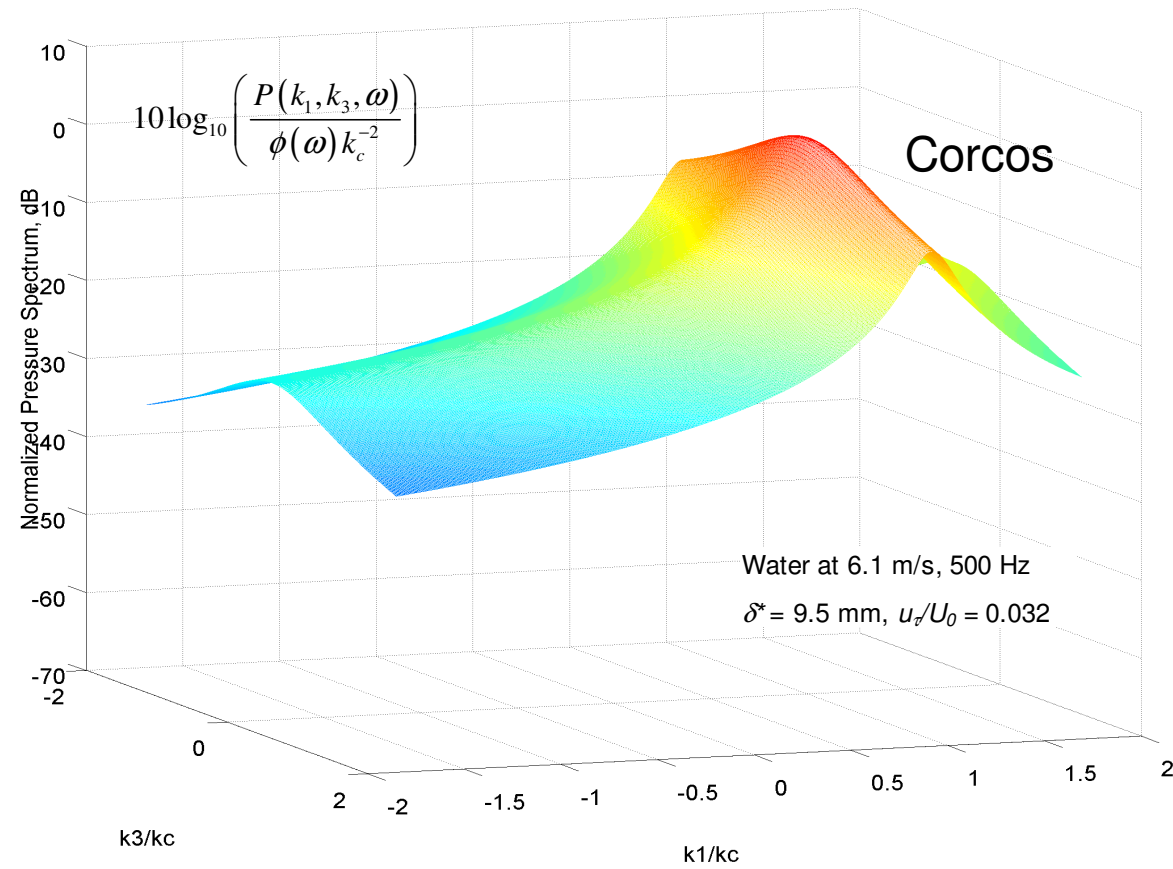
Figure 2.2 Corcos (1964) model of TBL wall pressure wavevector spectrum

$$10\log_{10}\left(\frac{P(k_1,k_3,\omega)}{\phi(\omega)k_c^{-2}}\right)$$

Chase 87

Water at 6.1 m/s, 500 Hz

$\delta^* = 9.5$ mm, $u_\tau/U_0 = 0.032$

Value of zero at zero wavenumber

Normalized Pressure Spectrum, dB

k3/kc

k1/kc
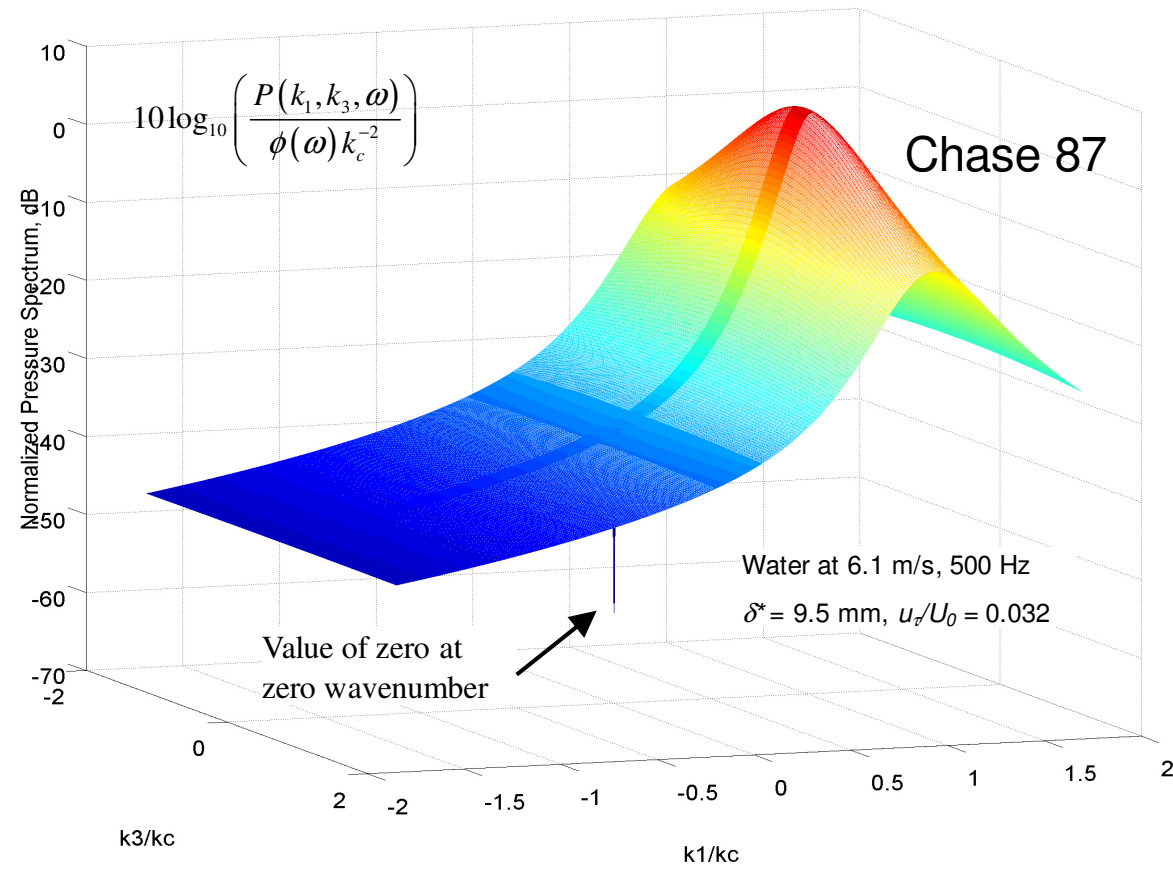
Figure 2.3 Chase (1987) model of TBL wall pressure wavevector spectrum

$$10\log_{10}\left(\frac{P(k_1,k_3,\omega)}{\phi(\omega)k_c^{-2}}\right)$$

Smolyakov

Water at 6.1 m/s, 500 Hz

$\delta^* = 9.5$ mm, $u_\tau/U_0 = 0.032$

Normalized Pressure Spectrum, dB

k3/kc

k1/kc
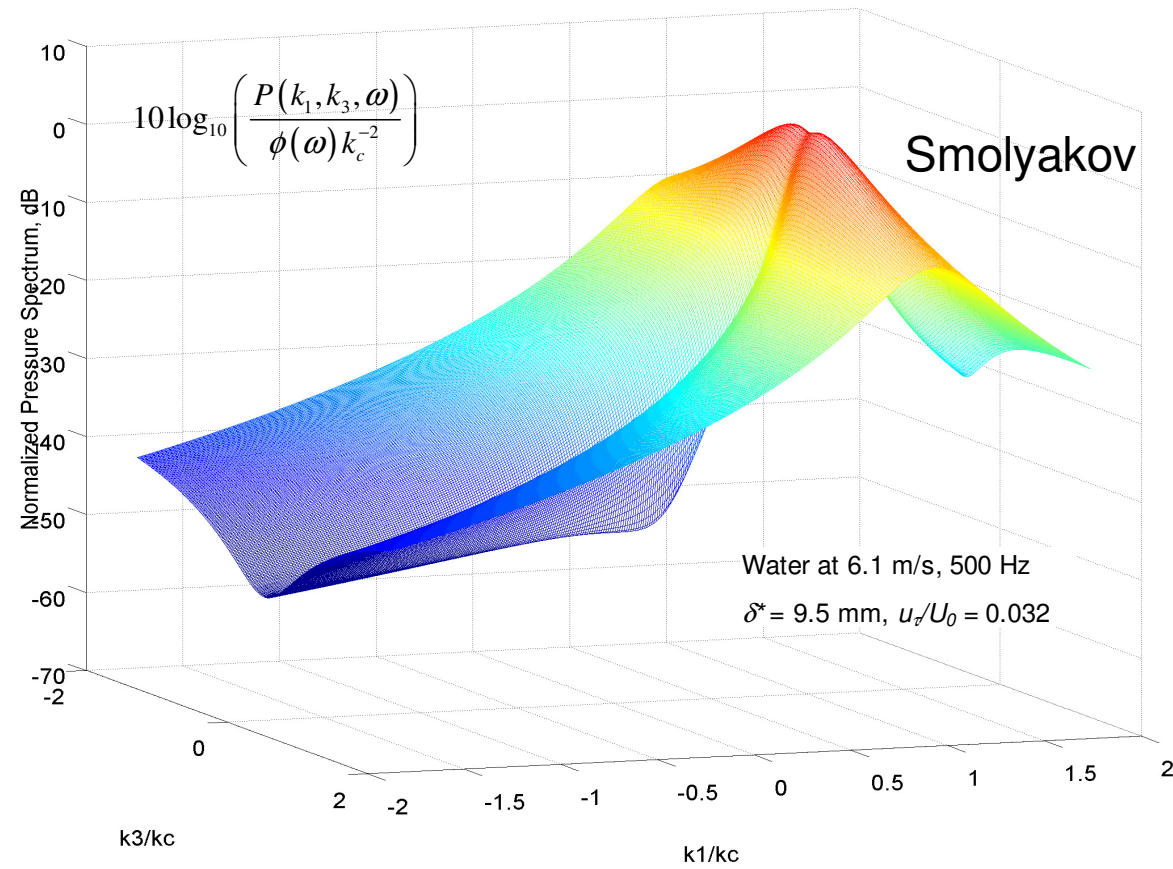
Figure 2.4 Smolyakov (2006) model of TBL wall pressure wavevector spectrum
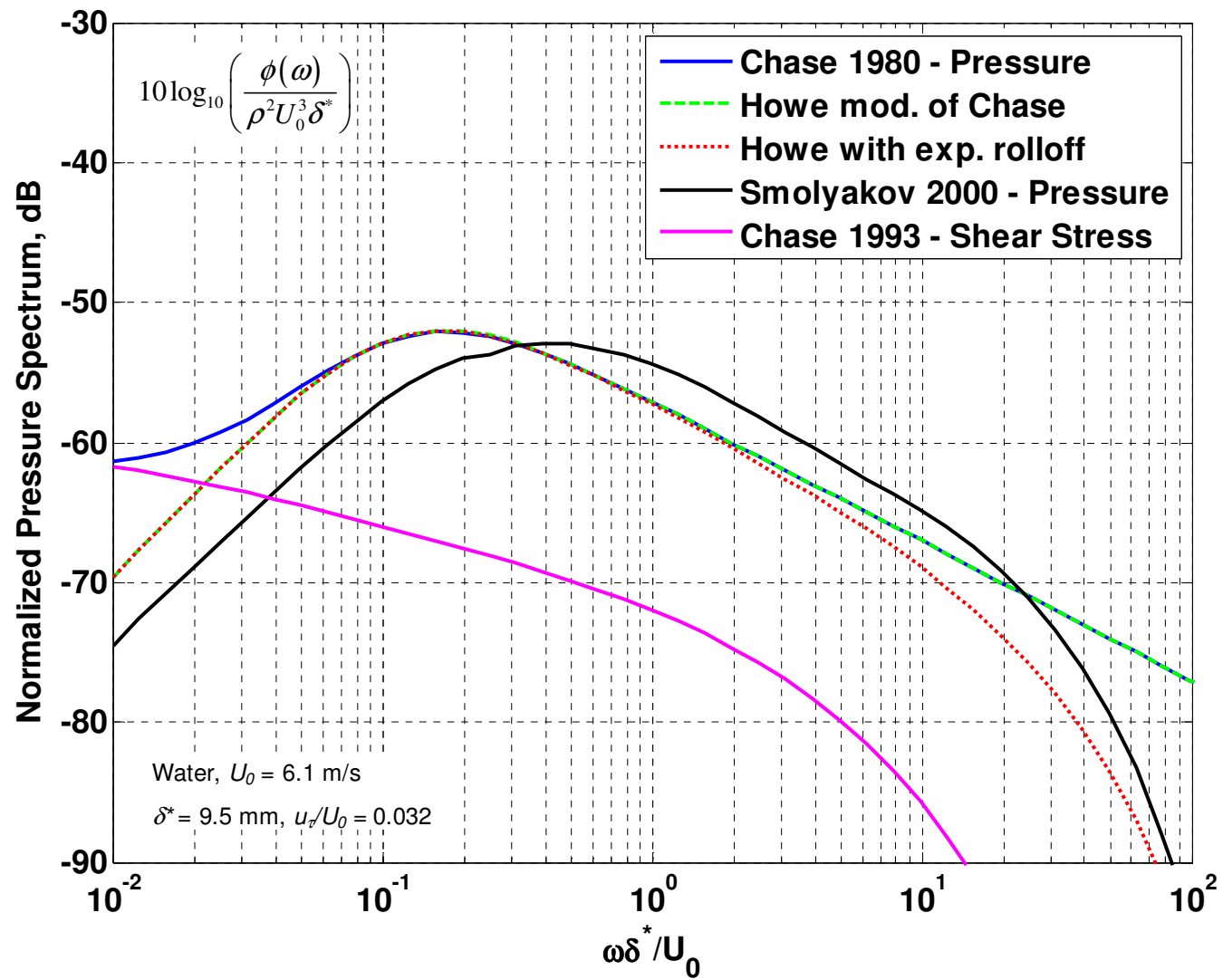
Figure 2.5 Models of TBL wall pressure and shear stress frequency spectra

$$10\log_{10}\left(\frac{S\left(k_1,k_3,\omega\right)}{\phi_{ss}\left(\omega\right)k_c^{-2}}\right)$$

Chase 93
Shear Stress

Water at 6.1 m/s, 1000 Hz

$\delta^* = 9.5$ mm, $u_\tau/U_0 = 0.032$

Normalized Shear Stress Spectrum, dB

k3/kc

k1/kc
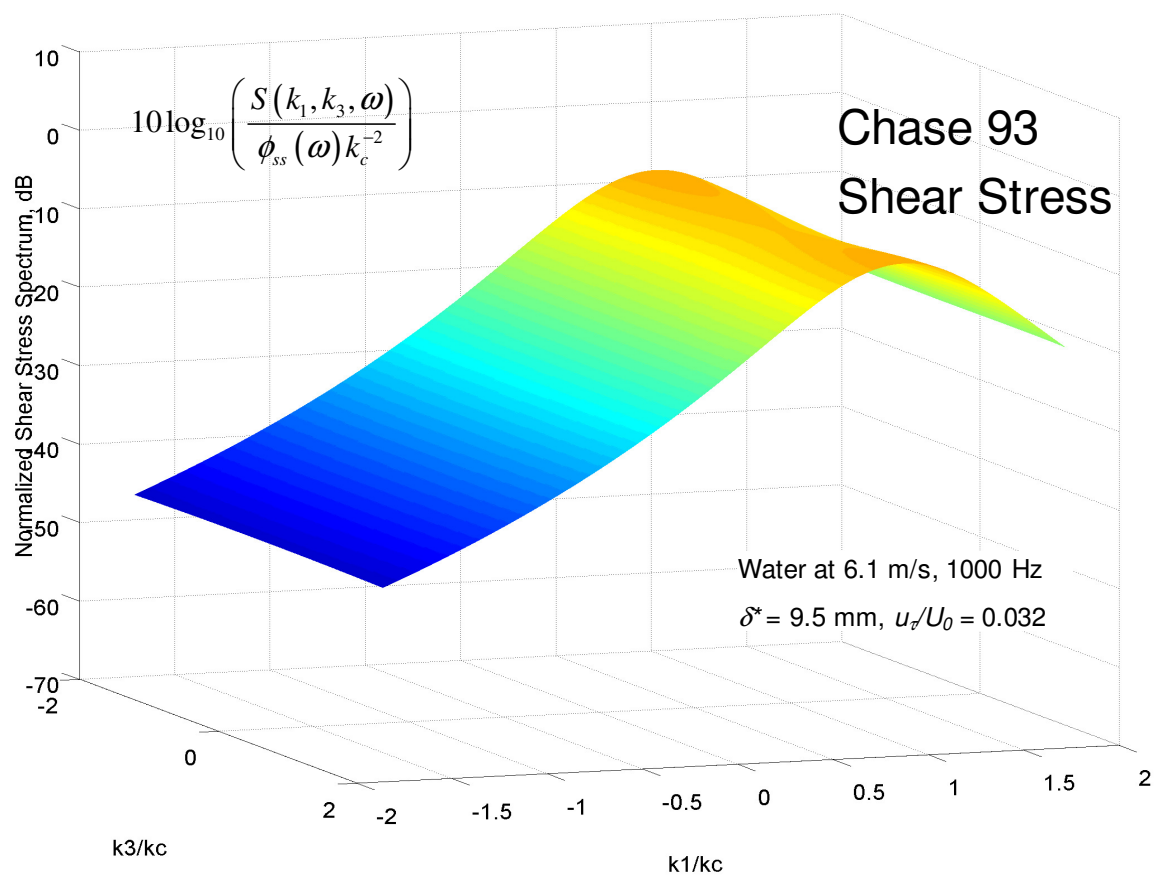
Figure 2.6 Chase (1993) model of TBL streamwise shear stress wavevector spectrum
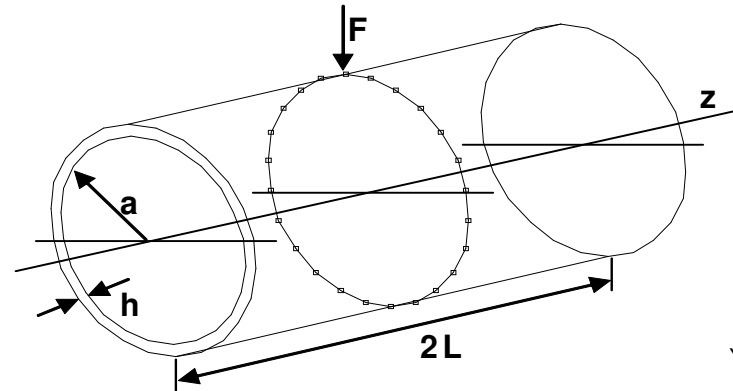
Aluminum cylinder

$\rho_s = 2700$ Kg/m^3 Material Density

$E_1 = 6.9 \times 10^{10}$ N/m^2 Young's Modulus

$\nu = 0.3$ Poison's ratio

$a = 75$ mm   Cylinder radius

$h = 3.2$ mm   Cylinder wall thickness

$2L = 0.61$ m   Cylinder half length (L)

$\eta = 0.01$ Mechanical damping ratio

Figure 2.7 Diagram of the cylindrical shell model, variable definitions, and parameter values

breathing **n = 0**

bending **n = 1**

lobar (n>1) **n = 2**

m = 1

0,1 - 760 Hz

1,1 - 431 Hz

2,1 - 242 Hz

m = 2

0,2 - 1497 Hz

1,2 - 1278 Hz

2,2 - 633 Hz
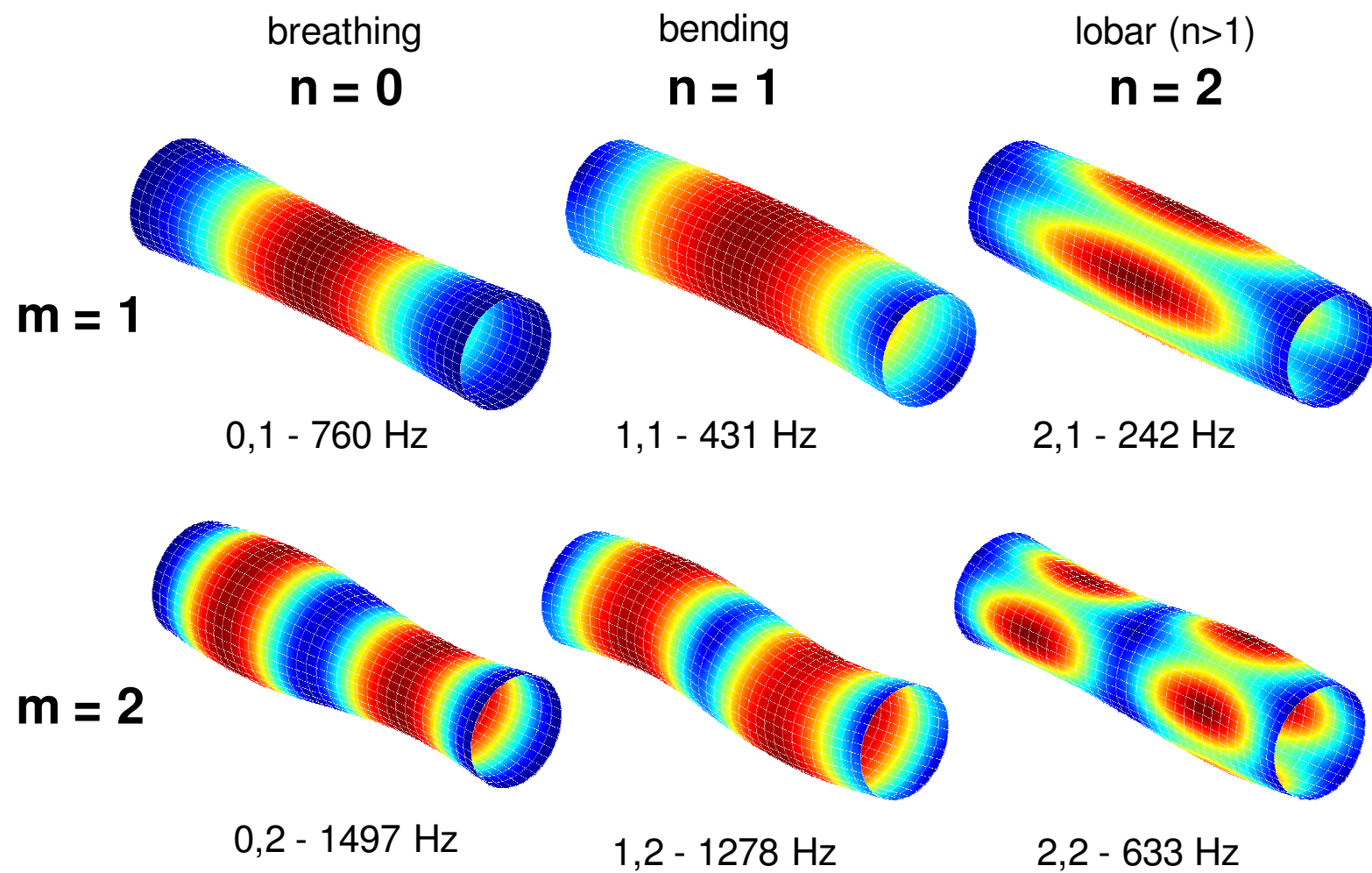
Figure 2.8 Example mode shapes of low-order cylinder modes
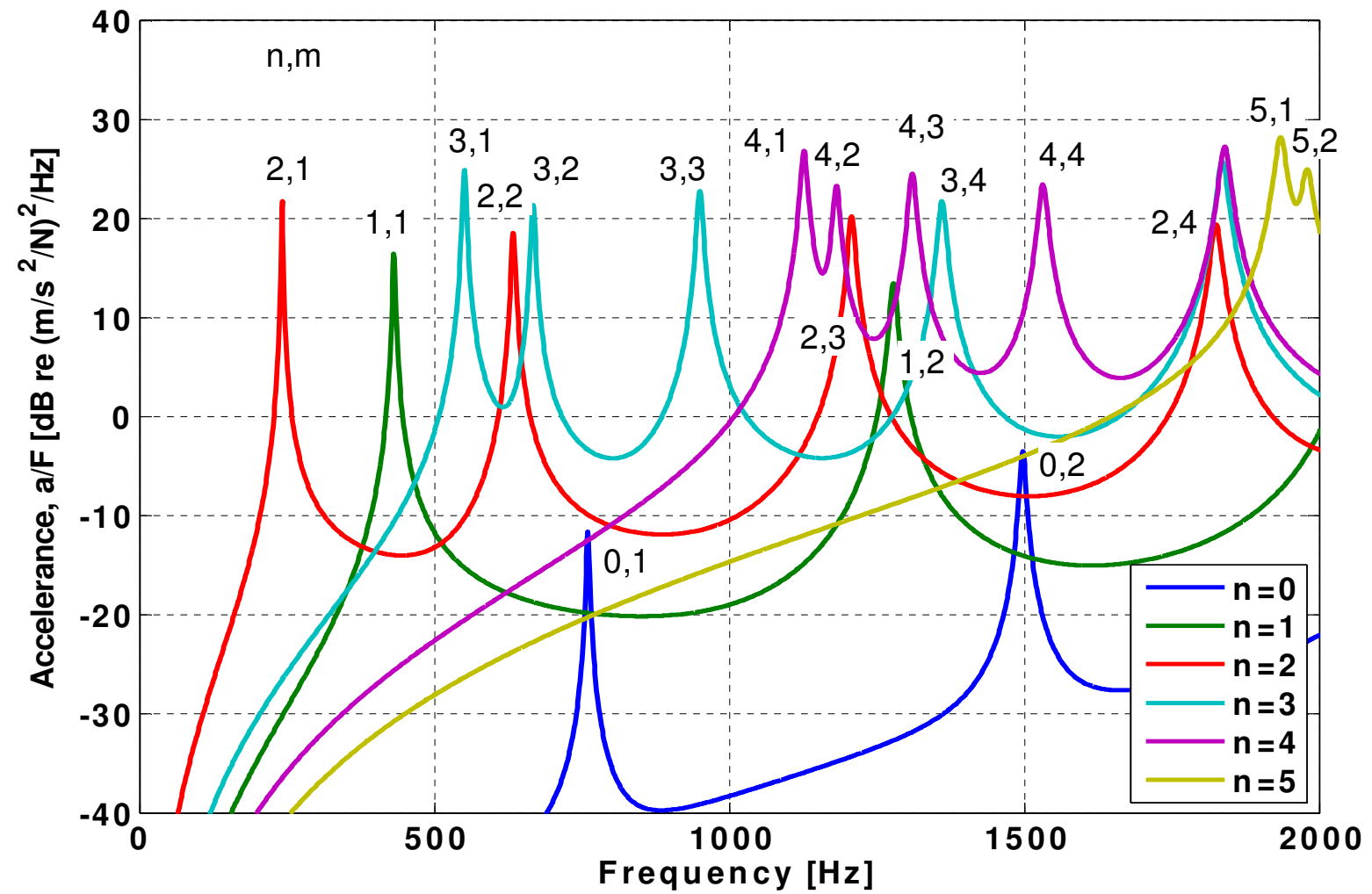
Figure 2.9 Analytical shell model radial vibration in response to radial excitation
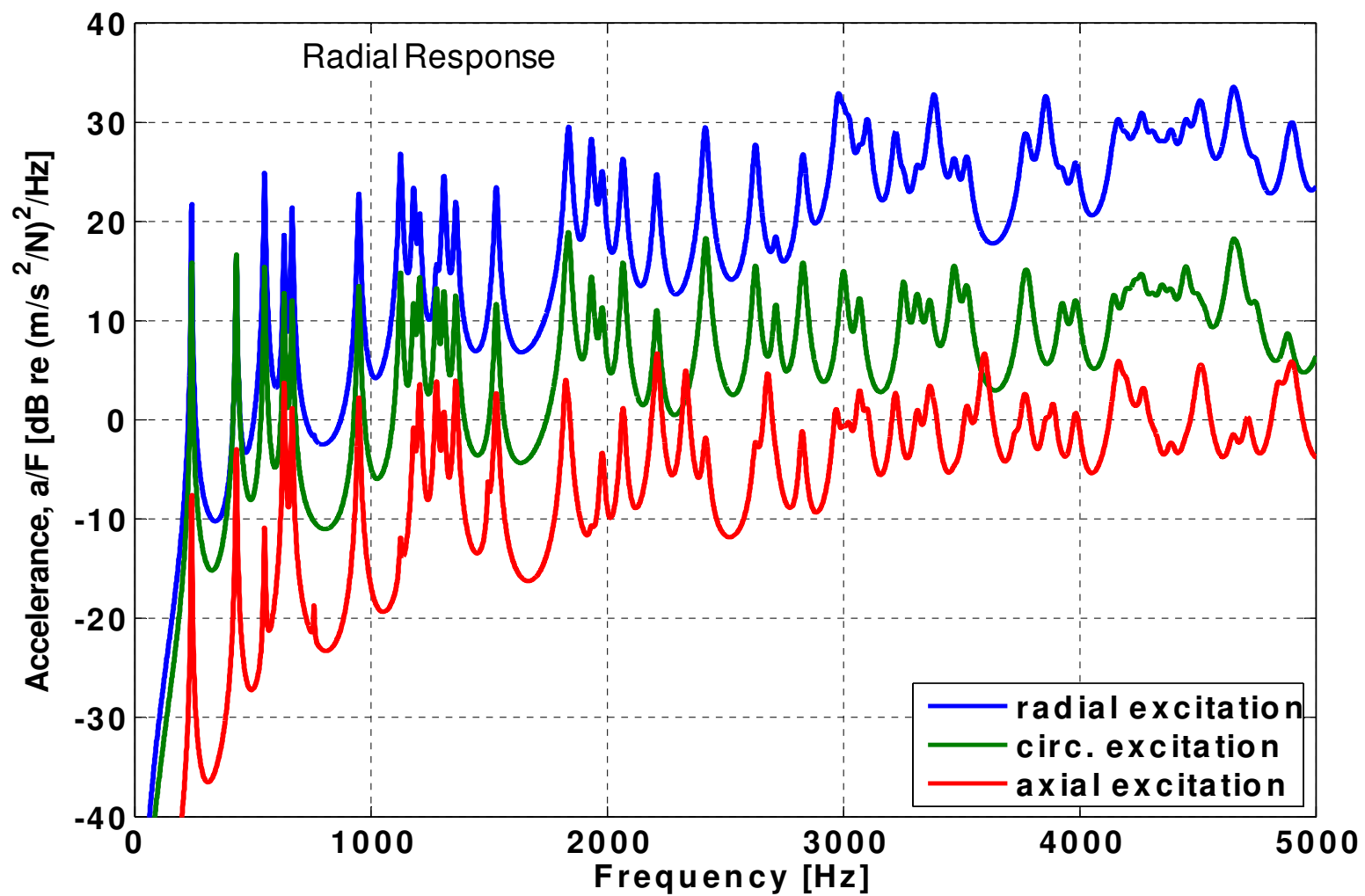
Figure 2.10 Analytical shell model radial vibration in response to excitation in three coordinate directions
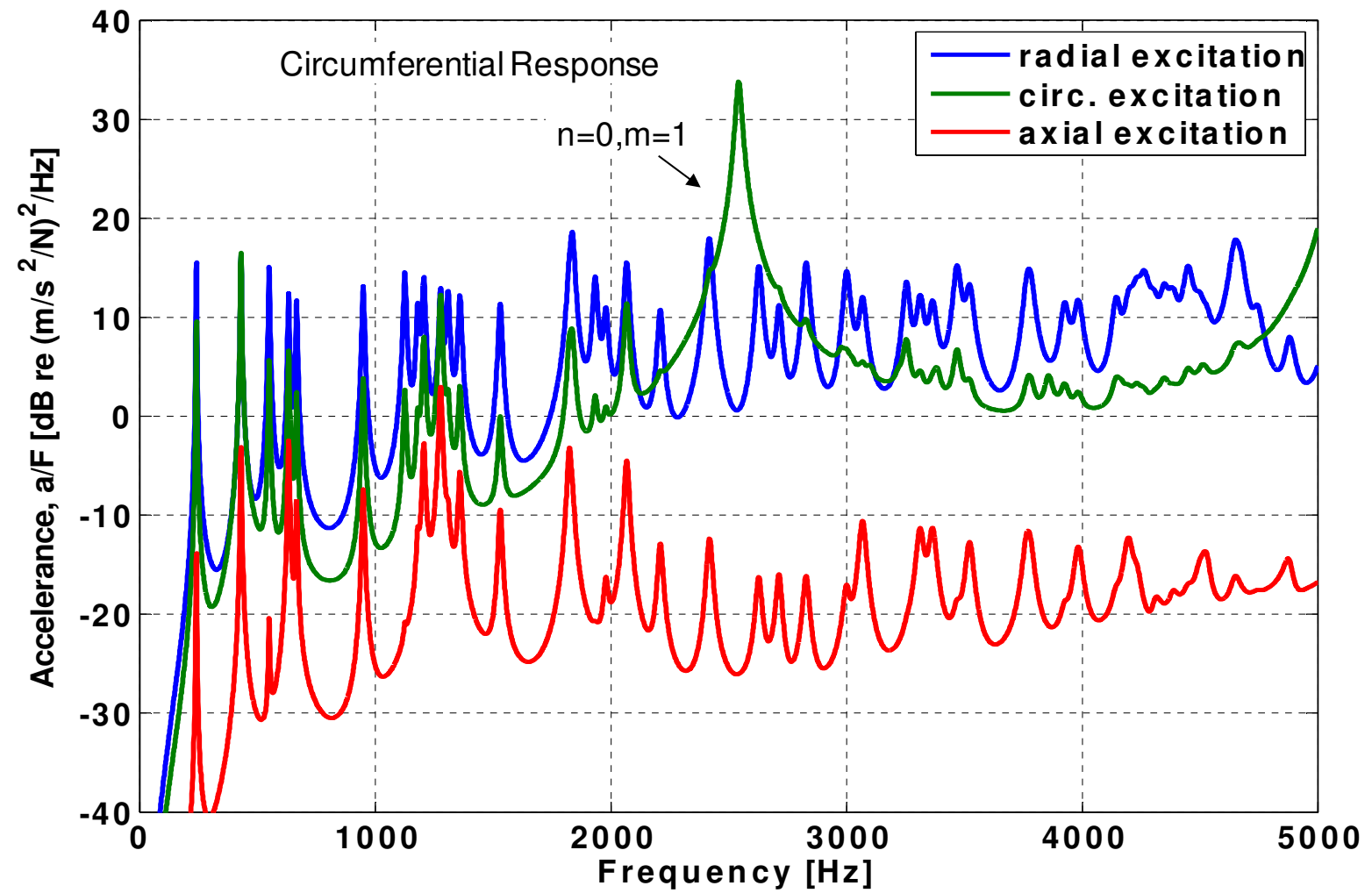
Figure 2.11 Analytical shell model circumferential vibration in response to excitation in three coordinate
directions
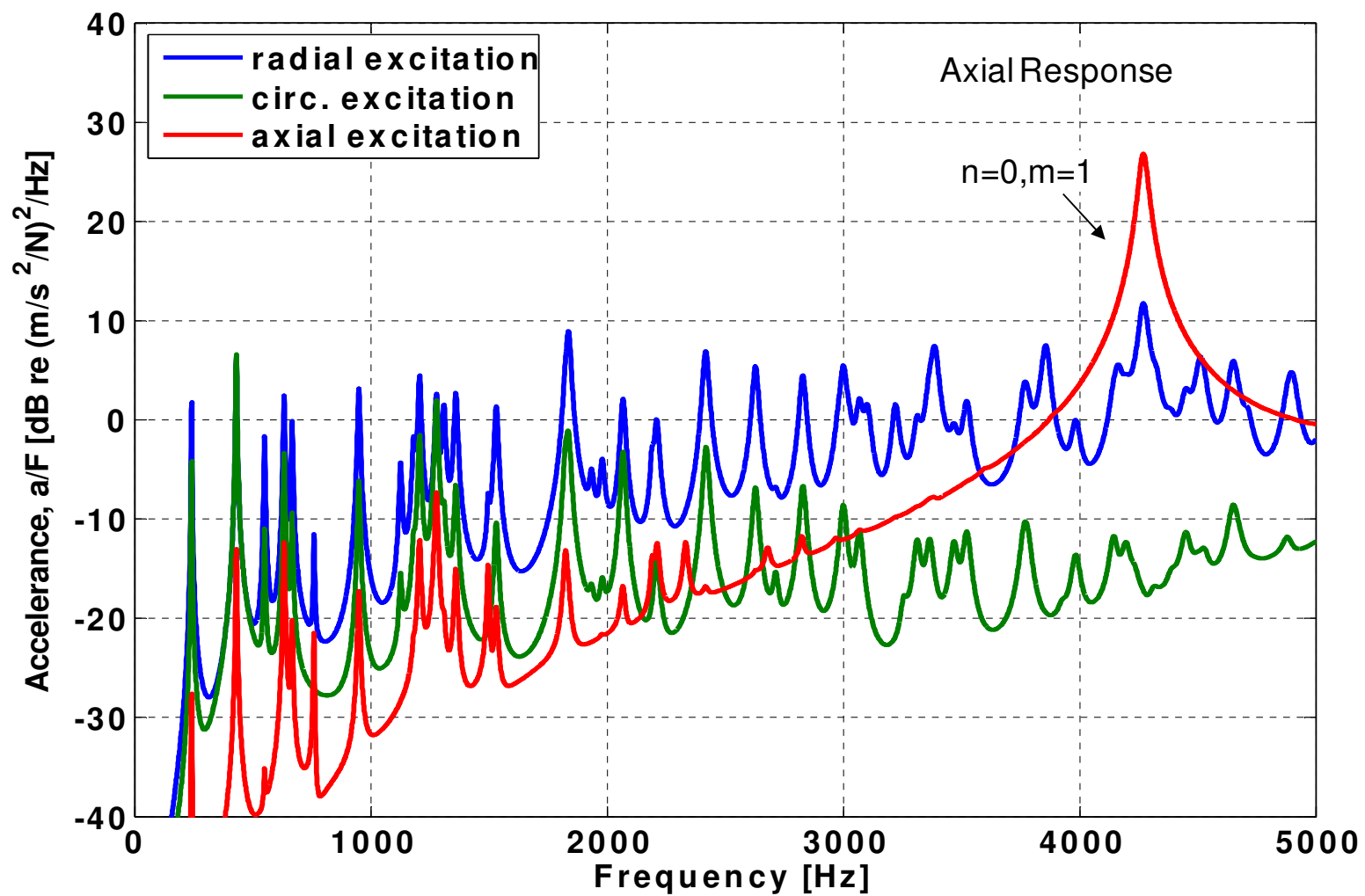
Figure 2.12 Analytical shell model axial vibration in response to excitation in three coordinate directions

n=3, m=1 (551 Hz)
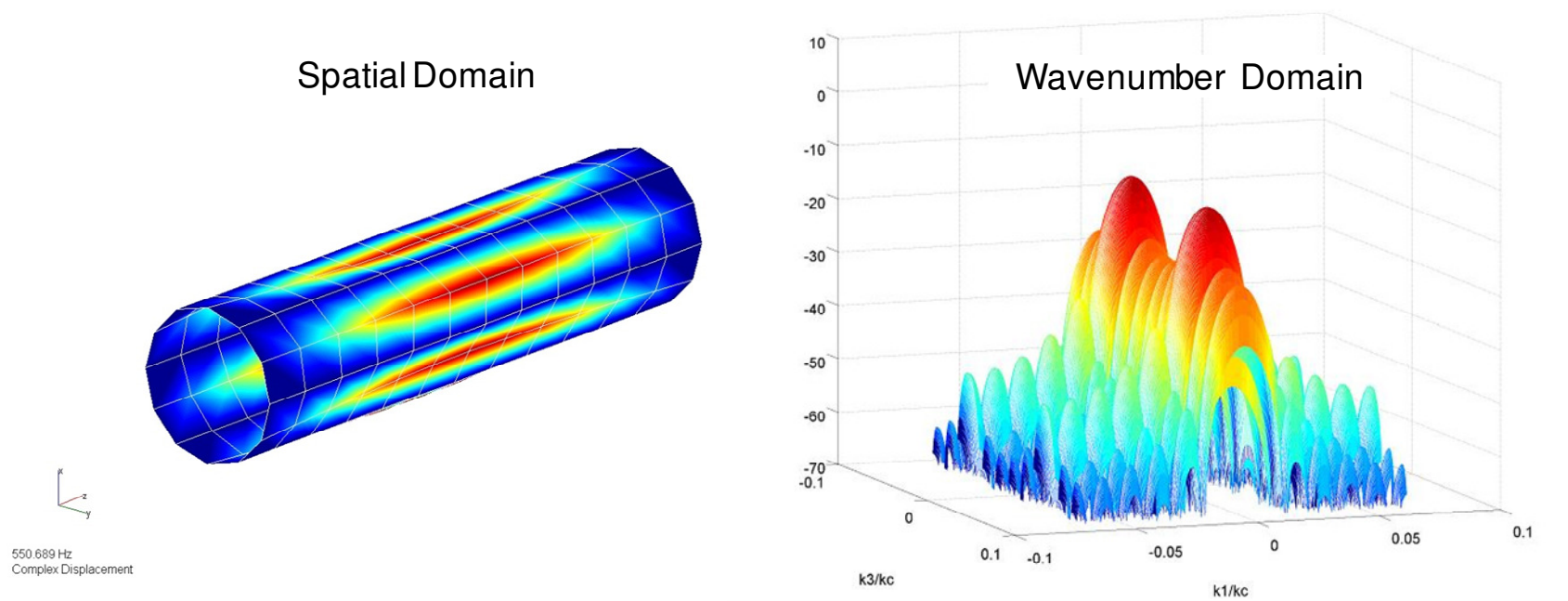
Figure 2.13 Analytical model example mode shape and corresponding sensitivity function
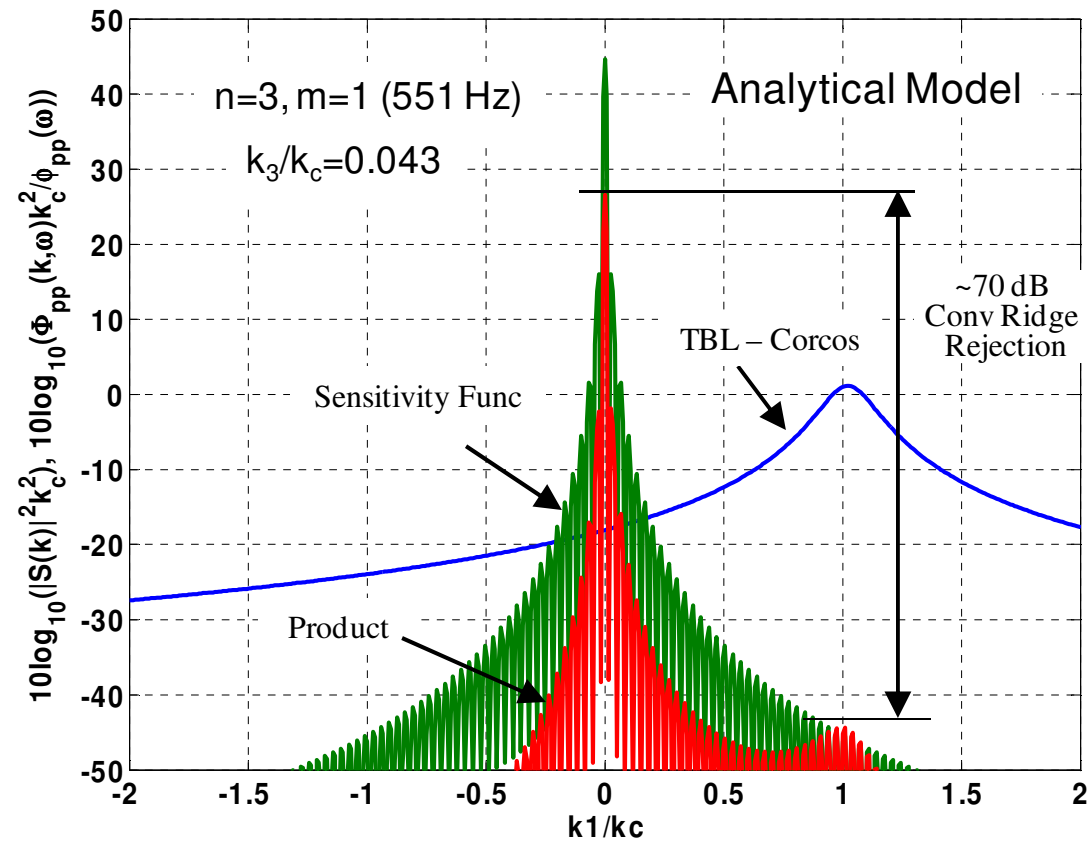
$$\left| F_n(\omega) \right|^2 = \int\limits_{-\infty}^{+\infty}\int P(k_1, k_3, \omega) \left| S_n(k_1, k_3) \right|^2 dk_1 dk_3$$

Figure 2.14 Flexible structure wavenumber filtering

Chapter 3

EXPERIMENTAL METHODS

3.1   Measuring Cylindrical Shell Response to Fully Developed Pipe Flow

The present work utilizes the Garfield Thomas Water Tunnel at ARL/PSU, depicted in Figure 3.1, as a 400 kl reservoir of water and capitalizes on the available hydrostatic head when the tunnel is filled. A long straight run of 150 mm diameter schedule 40, PVC pipe is connected to the lower leg of the tunnel and the pressure head above the pipe drives flow through a test-section (within the continuous pipe) into a reserve tank below the floor. The large volume of water contained in the water tunnel and reserve tank is adequate to produce only a small drop in velocity during the measurement window as the two tank levels equilibrate. The major advantage of this facility over more traditional flow facilities is that no fans or pumps are involved in driving the flow. This significantly reduces the normal background noise and vibration levels associated with a typical circulating water or wind tunnel facility which can mask the low pressure and vibration levels generated in low wavenumber TBL measurements.

The thin-walled aluminum cylindrical shell test-section is installed near the end of the straight pipe run which provides roughly 90 pipe diameters downstream from the nearest upstream flow distortion. This flow distortion is a perforated plate or flow straightening device (Laws, 1991, Spearman, *et. al.*, 1996, and Xiong, *et. al.*, 2003) installed just downstream of a large radius 90 degree elbow shown in Figure 3.2. The 90

pipe diameters of straight pipe provide ample length for both the velocity and turbulence profiles to reach fully developed conditions (Schlichting, 1979).

Flow is controlled using valves at the ends of the piping as shown in Figure 3.2. A gate valve is located on the upstream end where the pipe connects to the lower leg of the water tunnel and a butterfly valve is located on the downstream end where the pipe passes through the floor into a reserve tank. The butterfly valve is roughly 5 m or 30 pipe diameters downstream of the test-section. Available head from the filled water tunnel generates a flow speed of 6.1 m/sec in the 150 mm diameter pipe. Higher flow speeds are achievable; however, their use is limited due to cavitation inception in the pipe. The velocity change measured by a pitot-static probe in the pipe centerline as the water level drops during the 41 second time window required for data acquisition is +/- 1% from the average velocity. This system is very nearly steady-state over the data acquisition time period.

The 0.61 m long cylindrical shell test-section, shown in Figures 3.3 and 3.4, is machined from the center portion of a 1.22 m long, 150 mm diameter, schedule 40 (7.1 mm thick) aluminum pipe. The center thin-walled test-section is created by machining the outside surface down to a wall thickness of 3.2 mm. Circumferential V-shaped grooves are further machined to a depth of 0.64 mm around the outside of the pipe at the discontinuity between the thick pipe ends and the center thin-walled test-section. The grooves, illustrated in Figure 3.4, are used to further increase the structural discontinuity between the thick and thin sections of pipe. These grooves also help approximate pinned end conditions at the test-section boundaries.

The pipe inside surface is machined to create a constant inside diameter (measured at 156 mm), a constant test-section wall thickness, and a smooth interior surface. The aluminum pipe is also anodized which provides a slick interior surface finish approaching that of glass. Large aluminum blocks are rigidly bolted around the thick portion of pipe outside the center thin-wall test-section (adjacent to the V-shaped grooves) and rigidly attached to the floor which resides 23 cm below the pipe centerline. Sand bags are also placed on the thick piping outside the aluminum blocks to add mass and damping to the piping outside the test-section. The rigid blocks, grooves, corner braces, and sand bags shown in Figures 3.3 and 3.4, help limit motion of the shell end boundaries and help limit vibrational energy from crossing those boundaries.

The actual shell boundary conditions (BCs) for the experimental cylinder are likely a mix between pinned BCs and clamped BCs which differ from the simply supported BCs of the analytical shell model described in Section 2.3. An analytic solution only exists using simply supported BCs. Pinned BCs contain one additional constraint over the simply supported BCs in that translation in the axial direction is also constrained. For pinned BCs, all three translational degrees of freedom are fixed and all three rotational degrees of freedom are free. Clamped or rigid BCs are fixed for all six degrees of freedom for all points around the cylinder ends. Differing BCs between the analytical solution and the experimental setup leads to differing results between theory and experiment presented in Chapter 4 for certain low-order shell modes.

Only flow over the 0.61 m long test-section is intended to impart energy to the thin cylinder walls. The structural discontinuities marking the edges of the test-section are only on the outside of the pipe and create an abrupt change in pipe wall thickness

which acts as an impedance discontinuity. The internal flow does not experience any surface discontinuities at the leading or trailing edges of the test-section. The 1.22 m long aluminum pipe (in which the 0.61 m long test-section resides) is flanged and bolted between two sections of schedule 40, PVC pipe. Care was taken to minimize the gap between the pipe sections at the flanges.

Two line arrays of flush mounted wall pressure sensors (PCB-105M147, sens. ~ 50 mV/psi) are installed downstream of the test-section in the downstream thick portion of the 1.22 m long aluminum pipe shown in Figure 3.3. One array is aligned with the flow while the second is perpendicular to the flow. A ring array of twelve accelerometers (PCB W532, sens ~ 100mV/g) is attached around the shell at a single axial location corresponding to an evenly spaced circumferential grid. Five runs are conducted at the same flow conditions to allow moving and/or reorienting the circumferential ring array of accelerometers. Three runs are conducted with accelerometers oriented radially at the axial locations shown in Figure 3.3: $x/2L = 1/2$, $x/2L = 1/3$, and $x/2L = 1/6$. A fourth run is conducted with accelerometers oriented circumferentially and placed at the center axial location, $x/2L = 1/2$. A fifth run is conducted with accelerometers oriented axially and placed at the axial location, $x/2L = 1/6$. The variable mass loading effect of moving accelerometers to different measurement locations is minimized by placing dummy masses (approximating the mass of an accelerometer) at all grid locations unoccupied by an accelerometer.

In addition to the accelerometer and dynamic pressure sensor arrays, a pitot-static probe is installed in the pipe centerline 1.5 m downstream from the test-section, and two wall mounted static pressure taps are installed 0.91 m apart spanning the 0.61 m long

test-section. The pressure difference across the pitot-static probe and the static pressure drop across the test-section are measured using differential pressure transducers (Honeywell wet/wet differential, Model FP2000). The pitot probe and wall pressure taps provide measurements of the pipe centerline velocity and steady wall shear stress, respectively. The time domain accelerometer signals, dynamic pressure signals, and differential static pressure signals are all acquired simultaneously using an Agilent multi-channel data acquisition system sampling at 26,500 Hz. To generate frequency spectra from the time domain data, a complete Cross-spectral Density (CSD) matrix is computed from any desired set of sensors. The data is windowed using a Hanning window. Using 50% overlap and requiring 64 averages results in a total time record of 41 seconds. This data is later post-processed to establish the measured flow speed, convection velocity, steady wall shear stress, wall pressure spectra and cylinder vibration spectra in response to TBL excitation.

3.2   Experimental Modal Analysis

To determine actual mode shapes and modal masses associated with the resonance peaks identified in the flow data, a modal analysis is conducted on the test-section in all three coordinate directions with the cylinder and adjacent piping full of water. Figure 3.4 shows a picture and diagram of the modal analysis test setup. To acquire the modal transfer function data needed for the modal analysis, an evenly spaced 156 point grid (13 points axially by 12 points circumferentially) is excited with a roving force hammer in reciprocal manner. Flat spots are machined into the cylinder wall at each grid point to allow small aluminum cubes holding the accelerometers (or dummy masses)

to be securely adhered to each location. Frequency Response Functions (FRFs) are

simultaneously measured between the force hammer (PCB model type, sens ~ 50 mV/lbf)

and 12 reference accelerometers (PCB W532, sens ~ 100 mV/g). The 12 accelerometers,

consisting of four accelerometers oriented in each coordinate direction, represented drive

point locations at various axial and circumferential locations on the grid. The entire

modal grid on the cylinder was hit with the modal hammer three complete times with the

hammer oriented in a different coordinate direction for each pass. The transfer function

data between the modal hammer and 12 accelerometers were acquired simultaneously

using a Data Physics spectrum analyzer. The measured transfer functions, $H_{xy}(f)$, (or

FRFs) are defined as

$$H_{xy}(f) = \frac{G_{xy}(f)}{G_{xx}(f)} \tag{3.1}$$

where $G_{xy}(f)$ is the cross-spectrum between points x and y, and $G_{xx}(f)$ is the

autospectrum at x. The cross-spectrum and autospectrum are defined by

$$G_{xy}(f) = \overline{X^*(f)Y(f)} \tag{3.2}$$

where $X(f)$ and $Y(f)$ are the Fourier Transforms of the measured signals $x(t)$ and

$y(t)$ and the asterisk and overbar denote complex conjugate and ensemble average,

respectively.

After acquiring the FRF data, it is post processed using standard modal analysis

techniques to extract resonance frequencies, damping, modal masses, and mode shapes

for identifiable cylinder resonances and modes. The Complex Mode Indicator Function

(CMIF) technique is initially used to separate modes and identify resonance frequencies

and mode shapes (Catbas, *et. al.*, 2004). A Rational Fraction Polynomial scheme (Ewins, 2001) is then used to refine the resonance frequency and damping estimates. Finally, a surface average of measured FRF data is compared to corresponding FRF estimates using Equation 2.19 to determine the modal masses.

3.3   Processing Experimental Data

Although this test facility is designed to minimize background vibration and noise from interfering with TBL induced measured quantities, because the TBL levels are so low relative to other sources the measured data still contains a degree of unwanted signal contamination. Therefore a signal removal technique is implemented to recover the TBL induced signals.

In addition to the sensors installed to measure TBL induced vibration and pressure (TBL sensors), additional dynamic pressure sensors and accelerometers are installed at various locations to measure the unwanted signal (reference sensors). Two reference pressure sensors are installed in the same axial plane as the most upstream TBL pressure sensor, and are installed 120 degrees apart. The separation distance between the reference pressure sensors and all the TBL pressure sensors results in uncorrelated TBL pressures for all frequencies of interest (Lauchle and Daniels, 1988). Two reference accelerometers are placed in the midst of the TBL pressure sensor arrays to measure local pipe vibrations. In addition, six reference accelerometers are placed on the test-section supports (solid aluminum blocks) to measure the test-section boundary vibrations at both ends in all three coordinate directions. Figure 3.3 shows the location and number of

reference sensors used in the signal removal process. Acceleration is shown on the left and wall pressure is shown on the right.

Because the unwanted signals in this case produces coherent signals over long distances and the TBL induced signals do not, any portion of a TBL sensor signal coherent with a reference sensor signal can be removed leaving only the TBL induced signals. This technique is outlined by Bendat and Persol (1986) and illustrated with a three sensor model in the diagram of Figure 3.5.

The TBL induced cross-spectrum is desired between sensors x and y. Measured signals at x and y contain signals which correlate with a third reference sensor, n, representing the unwanted signal or noise. It is desirable to reject the portion of the measured x and y signals which correlate with the measured n signal. The TBL induced cross-spectrum, $G_{xy}(f)$, can be obtained from the measured cross-spectrum, $G_{x*y*}(f)$, and spectral measurements involving the reference sensor using

$$G_{xy}(f) = G_{x*y*}(f) - \frac{G_{x*n}(f)G_{y*n}(f)}{G_{nn}(f)}. \tag{3.3}$$

This requires that the cross-spectra between all sensors (both TBL sensors and reference sensors) be measured simultaneously. It also assumes that the correlation between the TBL sensors and reference sensors is associated with the unwanted signal only.

For a two sensor model, this signal removal technique reduces to a form related to Coherent Output Power (COP),

$$G_{xx}(f) = \left(1 - \gamma_{x*n}^2(f)\right)G_{x*x*}(f). \tag{3.4}$$

This form yields a TBL induced autospectrum, $G_{xx}(f)$, obtained from a measured

autospectrum, $G_{x^*x^*}(f)$, and the coherence, $\gamma^2_{x^*n}(f)$, between a TBL sensor, x, and a

reference sensor, n.

This technique can be generalized to include as many reference sensors as desired

and still retain the cross-spectrum between any pair of TBL sensors,

$$G_{xy \cdot n!}(f) = G_{xy \cdot (n-1)!}(f) - \frac{G_{xn \cdot (n-1)!}(f) G_{ny \cdot (n-1)!}(f)}{G_{nn \cdot (n-1)!}(f)}, \tag{3.5}$$

where conditioned spectral densities of order $n!$ can be computed from previously known

conditioned spectral quantities of order $(n-1)!$.

Figures 3.6 and 3.7 demonstrate example results using the signal removal

technique on measured wall pressure cross-spectra. As with all pressure spectra reported

in this work, the correlated signals from two reference pressure sensors and two reference

accelerometers are removed from all reported pressure spectra. Figure 3.6 shows the

improved phase recovered below 100 Hz between flush mounted TBL pressure sensors in

the streamwise direction. Figure 3.7 shows the Corcos (1963) correlation function

compared with improved coherence recovered between TBL pressure sensors in the

streamwise array.

When evaluating the vibration data from the experimental cylinder obtained from

either water flowing through the test-section or from the impact modal analysis testing, it

is helpful to know the modal content of the vibration spectra. A helpful process for

identifying and analyzing the modes in vibration data from circular structures is

decomposing the individual rings of data into their Fourier wavenumber components.

Using representative transfer function data, $H_{xy}(f)$, an N-point spatial Discrete Fourier

Transform (DFT) can be performed around each ring of measured data for all

frequencies:

$$H_n(f) = \frac{1}{N} \sum_{y=1}^{N} H_{xy}(f) e^{-j2\pi(n-1)(y-1)/N} \, , \qquad (3.6)$$

where $H_n(f)$ represents the wavenumber components (positive and negative). In this

case, twelve evenly spaced response locations around each ring ($N=12$) yield six

circumferential mode orders before aliasing occurs. The resulting Fourier components

can be summed to recover the average measured data for each ring. Figure 3.8 shows

example results of circumferential Fourier decomposition using a single ring of 12 FRF's

from the modal analysis data.

Equation 3.6 requires transfer function data which is easily obtained from a modal

analysis experiment but which must be created from operational flow data when the input

force is not measured. Using the measured accelerometer cross-spectra obtained from

flow data, an arbitrary sensor in the ring array of accelerometers is chosen as the

reference sensor, x, in Equation 3.1. The magnitude of the resulting transfer functions

range from zero to one and must be "scaled" to produce spectral values and character

representative of the measured vibration,

$$H_{xy}(f) = \frac{G_{xy}(f)}{G_{xx}(f)} |G_{xx}(f)|^{\frac{1}{2}}. \qquad (3.7)$$

For this data set, this results in a set of 12 transfer functions relative to a single reference

accelerometer. Since the choice of the original reference accelerometer is arbitrary, it is

beneficial to repeat the process choosing each accelerometer in the ring array as the

reference sensor in succession until 12 sets of 12 transfer functions exist. A spatial DFT

(Equation 3.6) can be applied to each of the 12 sets of transfer functions, and the resulting

Fourier components for the different data sets can be averaged together to yield the

Fourier wavenumber components of the original average accelerometer spectrum. Figure

3.9 shows example results of the circumferential Fourier decomposition process used for

the flow data using a ring of 12 accelerometer signals. As with all flow related

acceleration spectra reported in this work, the correlated signals from two reference

pressure sensors and six reference accelerometers are removed from all reported

acceleration spectra.

Although resonance frequencies and damping are standard outputs from a typical

experimental modal analysis, they can also be estimated directly from measured vibration

data for certain structural modes. Resonance frequencies can be identified as the

frequencies corresponding with the maximum power levels, or resonance peak levels,

associated with each structural mode. Structural damping can be estimated based on

values related to the sharpness of the resonance peaks (Kinsler, *et. al.*, 1982). Structural

damping, η, expressed as a percentage, can be approximated as

$$\eta \cong \frac{\omega_2 - \omega_1}{\omega_0} \, , \tag{3.8}$$

where ω_2 and ω_1 are the two frequencies above and below the resonance frequency, ω_0,

where the average power has dropped to one-half of its original resonace peak value (3

dB below). Results for estimating resonance frequencies and damping using these

methods are presented in Chapter 4 for cylinder vibration data subjected to TBL flow

excitation.

Top View

150 mm PVC Pipe

Reserve Tank beneath floor

Cylindrical Test Section

Flow @ 6.1 m/s

13.5 m ~ 90 pipe diameters

Side View

97'- 2"

Top of Test Section

7 m

12 FT. DIAMETER SECTIONS

Hydrostatic pressure drives flow thru pipe

31'-1"

26'-10"

Ground Level

97'- 7"

3.7 m

Reserve Tank Floor
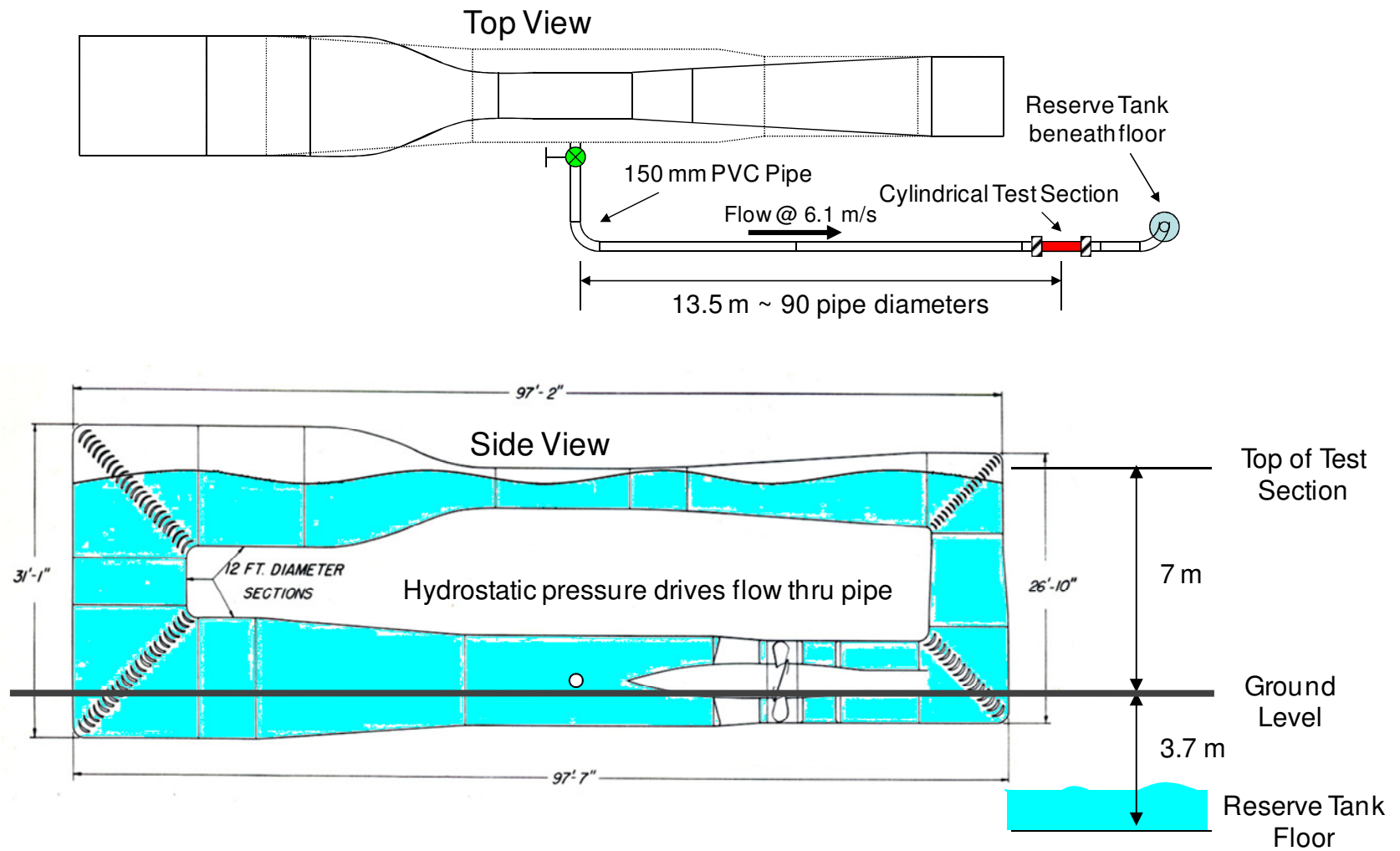
Figure 3.1 Experimental Facility - ARL 48" WT, piping, and cylindrical test-section
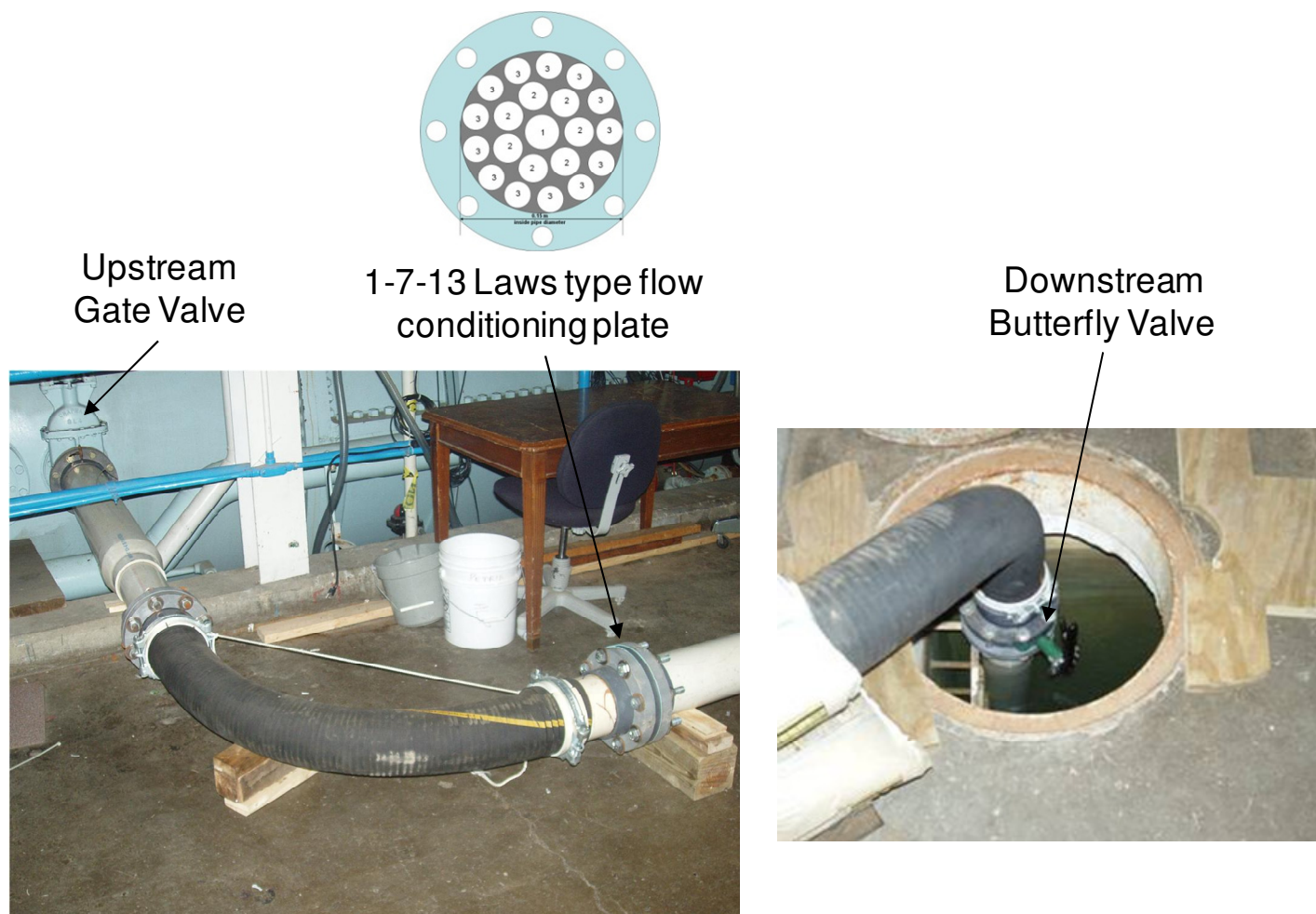
Figure 3.2 Valves and flow conditioning in the piping system
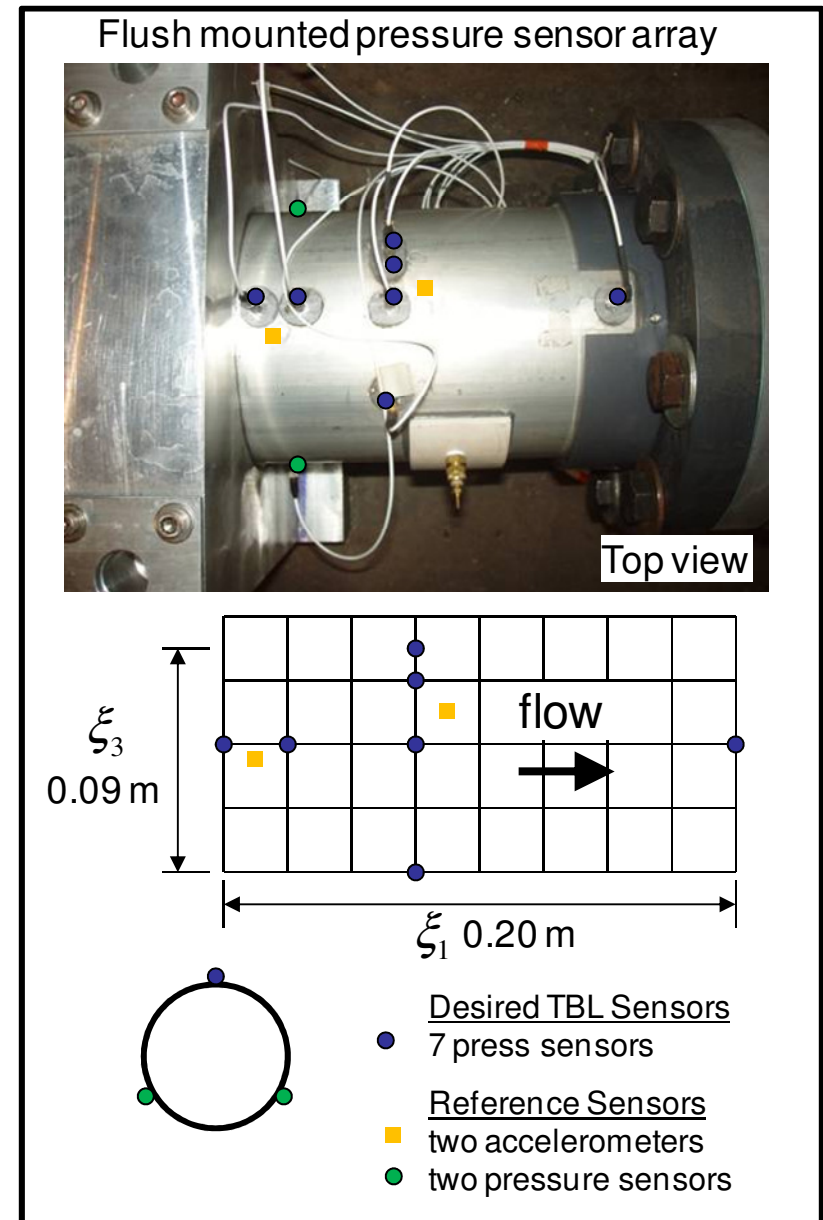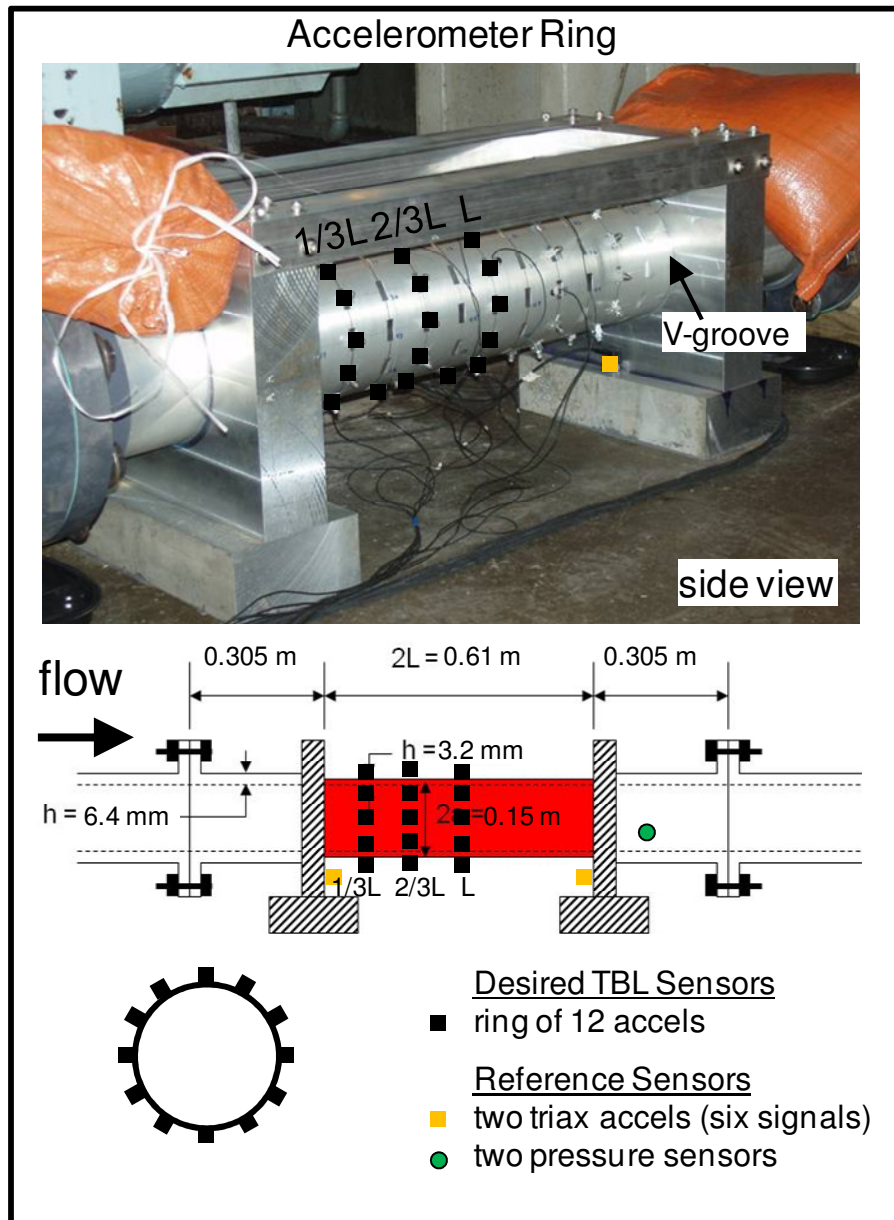
Figure 3.3 Experimental test-section, flow measurement arrays, reference sensors

7.1 mm

0.64 mm

3.2 mm

Schedule 40 pipe wall

Thin pipe wall

Aluminum block

V-groove

Measurement grid unwrapped

Bottom of cylinder

Circ. accels

Top of cylinder

Radial accels

Bottom of cylinder

Axial accels

Reciprocal measurement - Impact each grid point with hammer, accelerometer locations represent drive points

12 X 13 grid - 156 grid pts
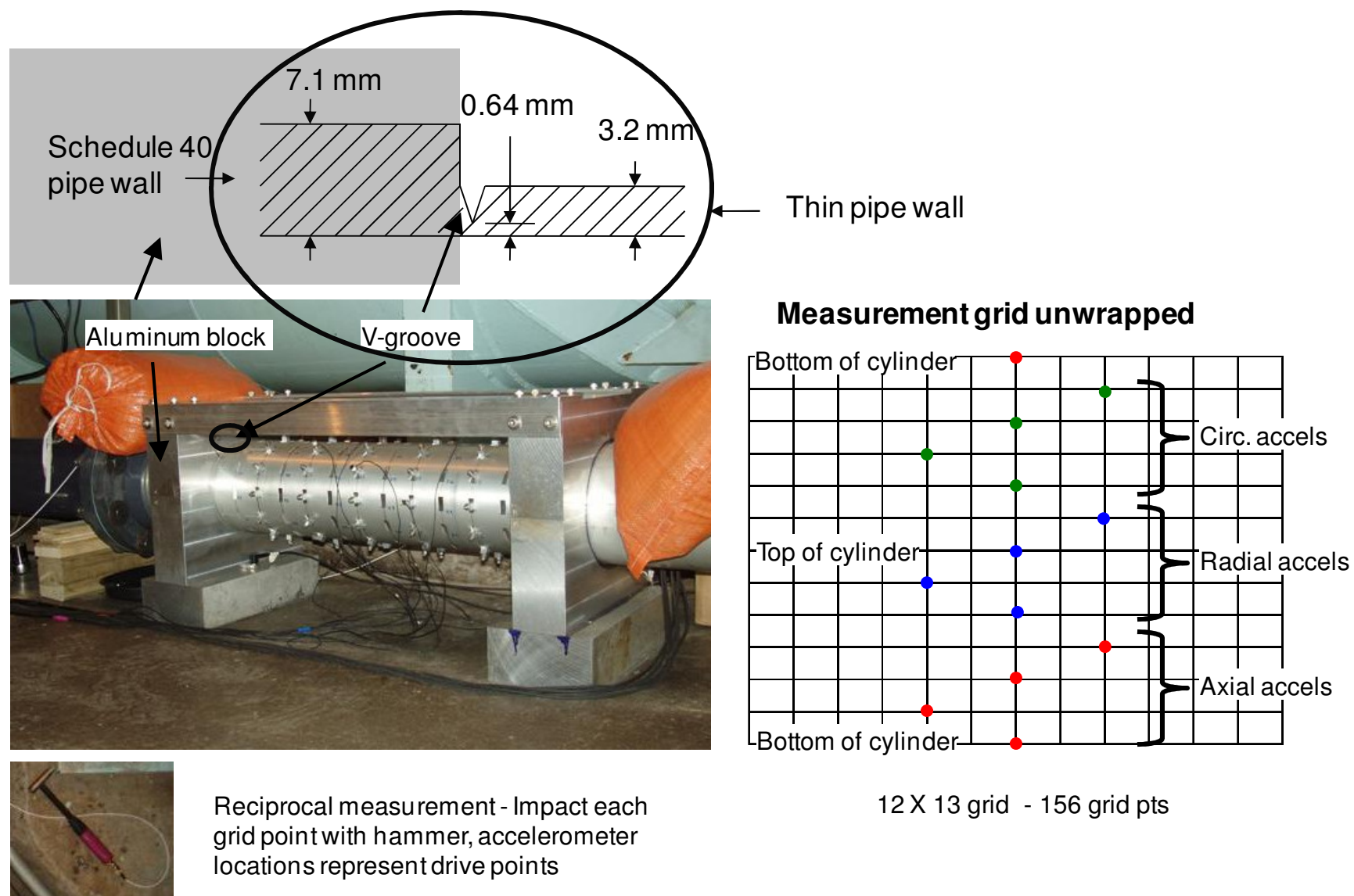
Figure 3.4 Experimental modal analysis test set-up
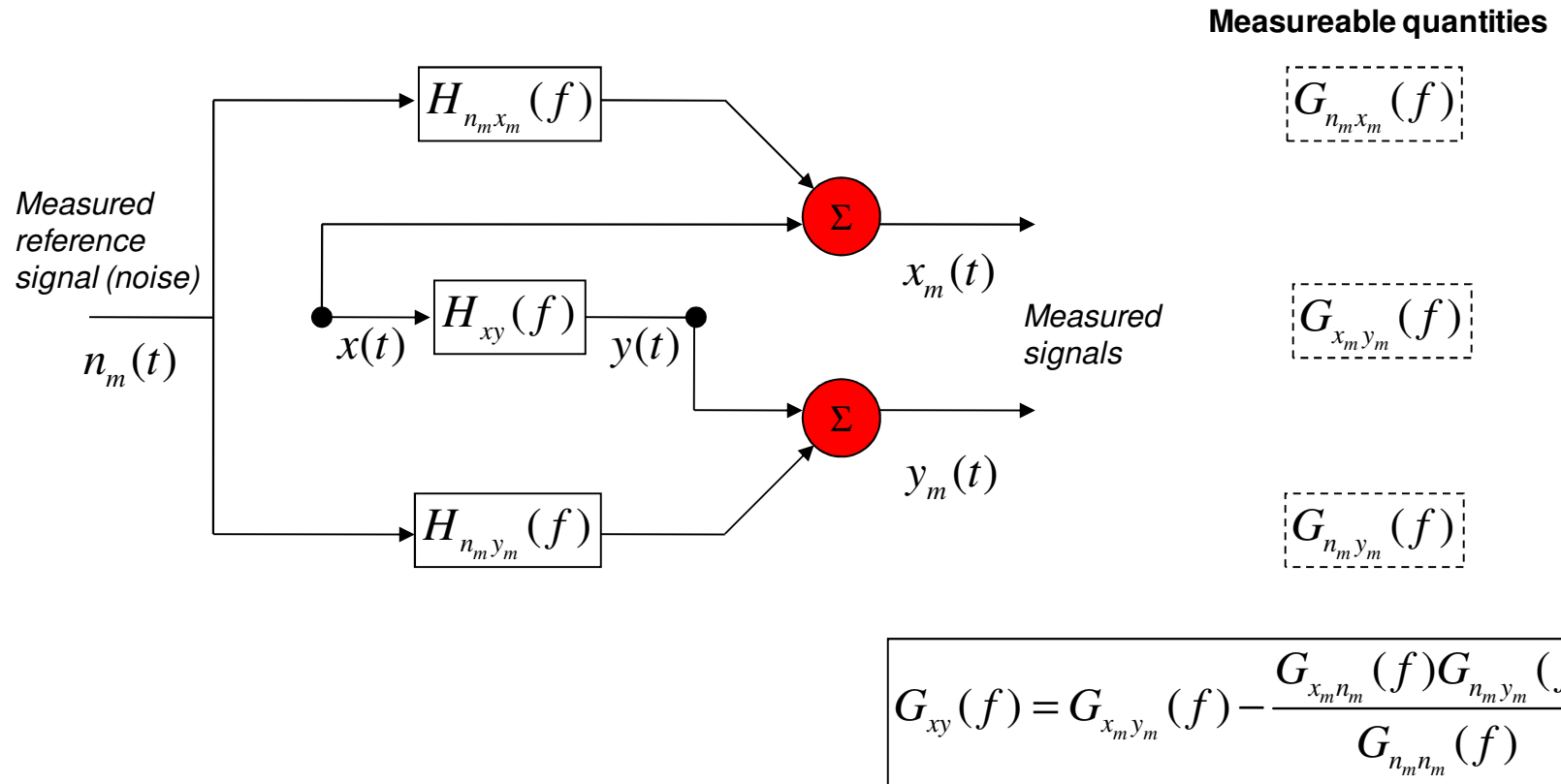
Figure 3.5 Three sensor model of coherent signal removal process
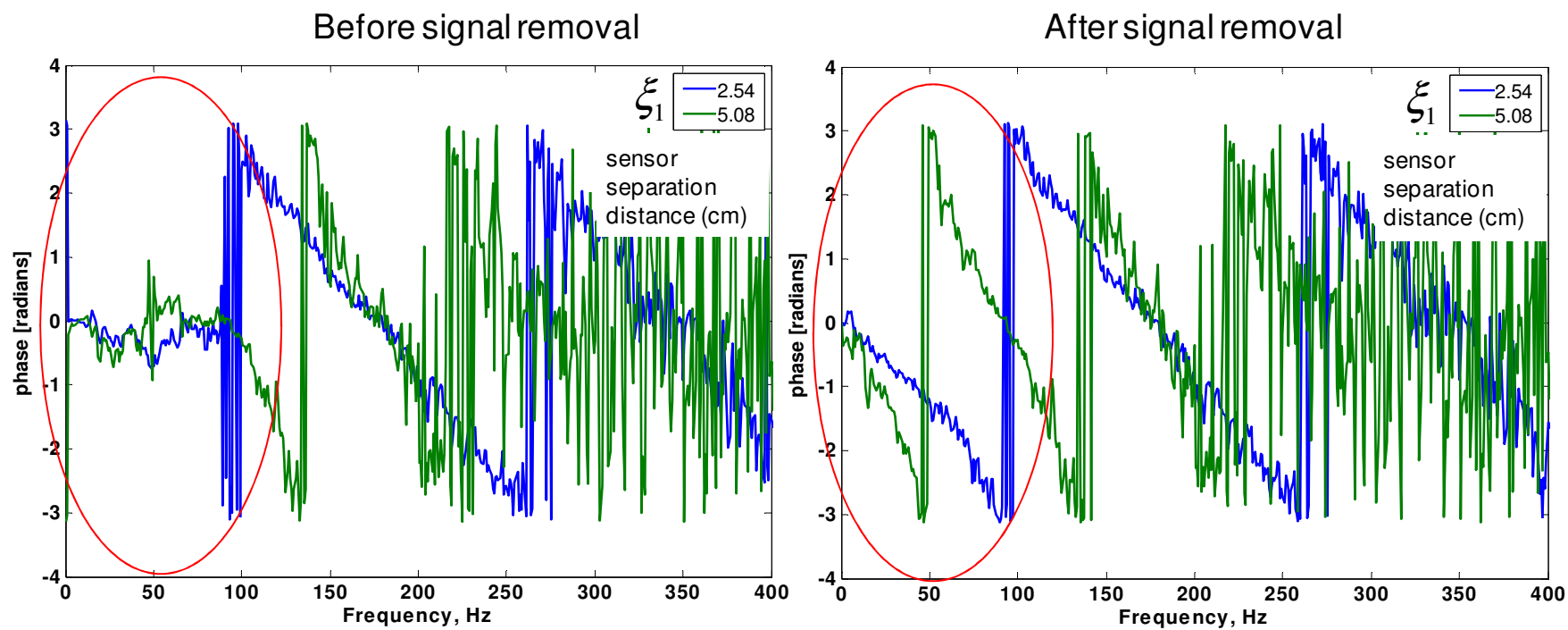
Figure 3.6 Example of signal removal using TBL wall pressure cross-spectra: phase between TBL pressure sensors separated in the streamwise direction
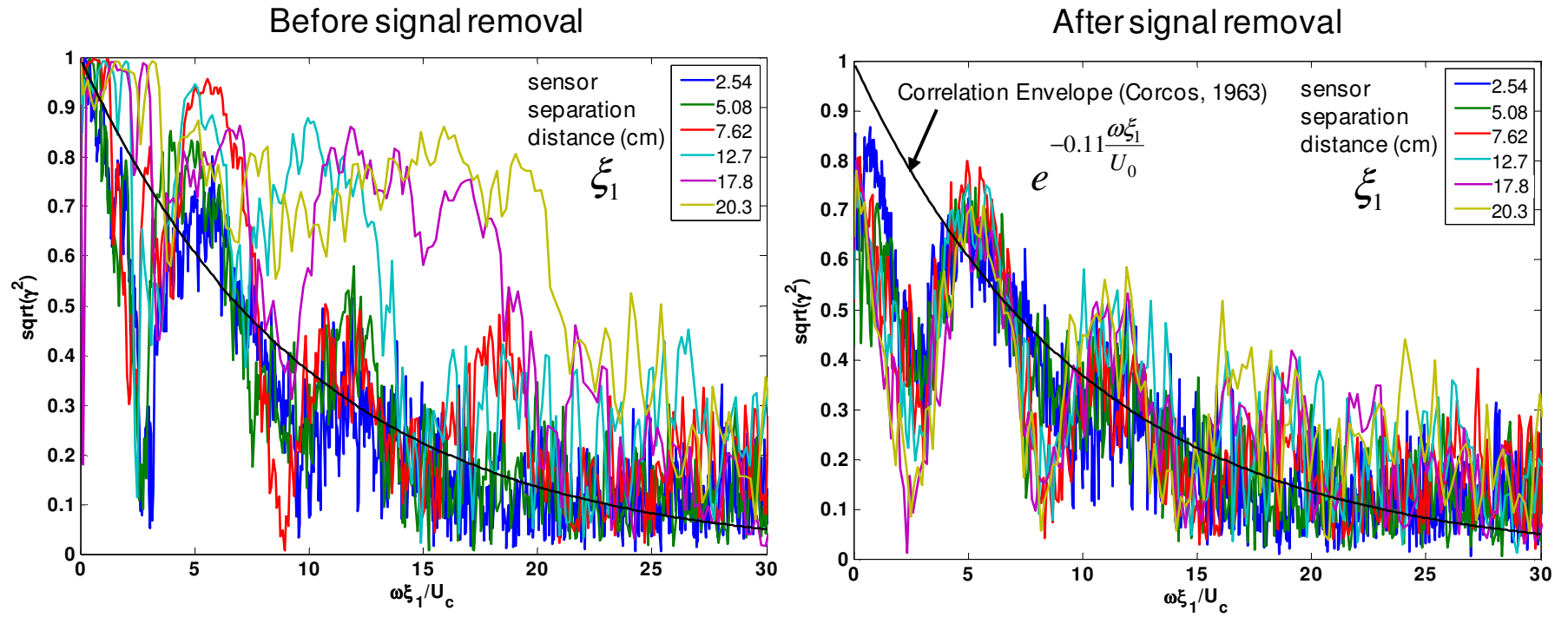
Figure 3.7 Example of signal removal using TBL wall pressure cross-spectra: coherence between TBL pressure sensors separated in the streamwise direction
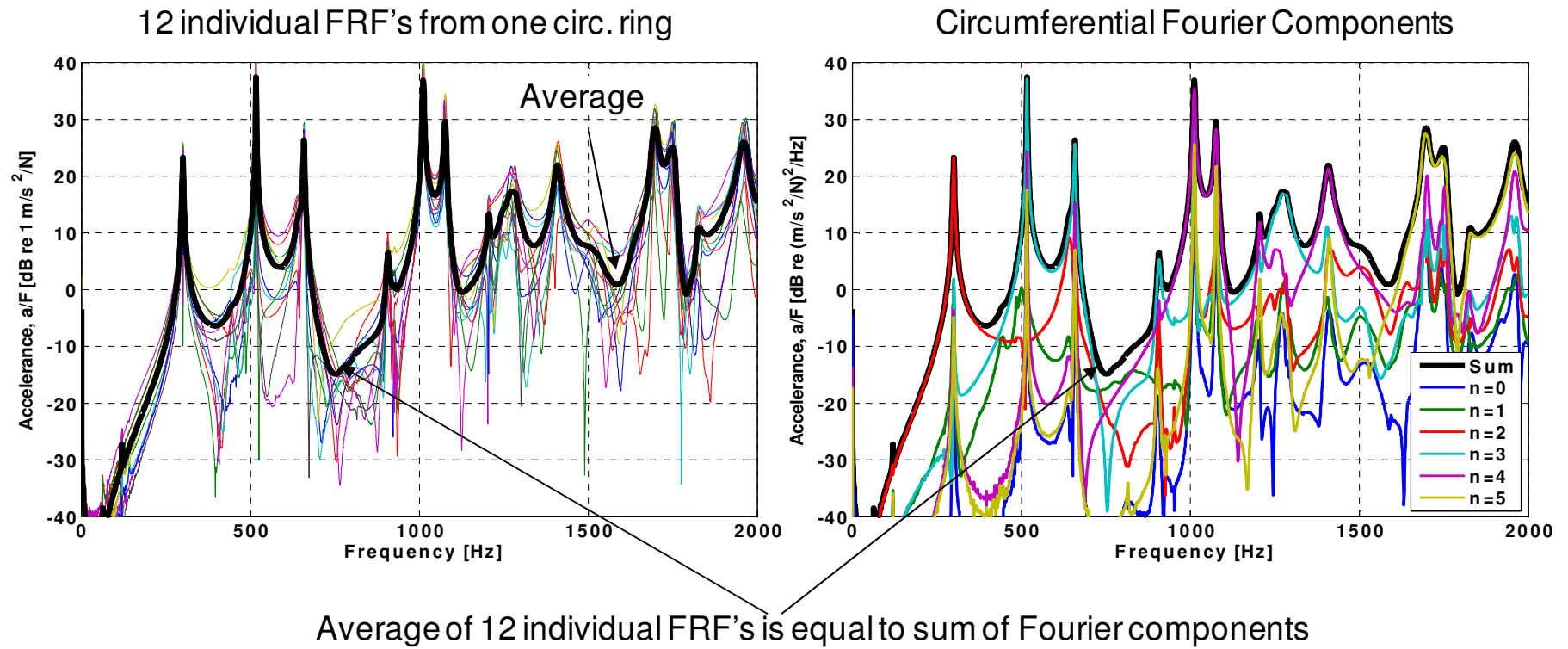
Figure 3.8 Example of circumferential Fourier decomposition using ring of 12 accelerometer FRF's from modal analysis data
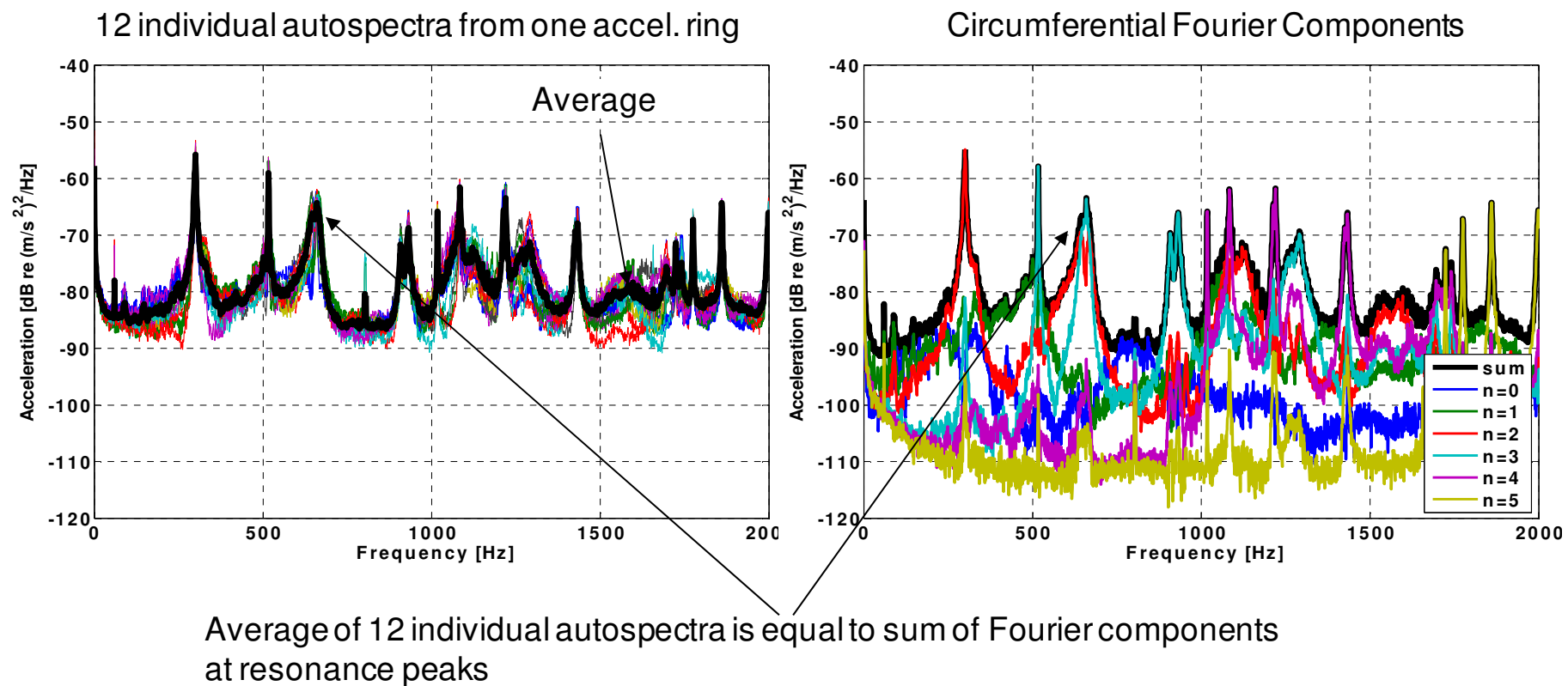
Figure 3.9 Example of circumferential Fourier decomposition using ring of 12 accelerometer signals from flow data

Chapter 4

RESULTS OF EXPERIMENTAL INVESTIGATION

4.1   Flow Measurement Results

The pitot-static probe placed in the pipe centerline measures total pressure (at the probe stagnation point) and static pressure (along the side of the probe) from which dynamic pressure, $P_{dyn} = \Delta P = P_{tot} - P_{stat}$ can be determined. The pipe centerline velocity can be computed from

$$v = \sqrt{\frac{2g_c}{\rho}(\Delta P)} \, . \tag{4.1}$$

The steady wall shear stress is determined by measuring the static pressure drop, ΔP, along the wall over a 0.91 m length spanning the cylindrical test-section. One can solve first for the friction factor, f, and then the wall shear stress, u_τ, using

$$\frac{\Delta P}{\rho g} = \frac{fL}{D}\frac{V_{bulk}^2}{2g}, \qquad \text{and} \qquad u_\tau = \frac{V_{bulk}}{(8/f)^{\frac{1}{2}}} \, . \tag{4.2}$$

Since fully developed pipe flow is established at the test-section, relationships for the velocity profile, bulk velocity, and boundary layer thickness are assumed to be known from historical research (Schlichting, 1979).

Five repeat flow runs are conducted with the only change being the axial location or directional orientation of the accelerometer ring array on the cylinder. Flow parameters for the five runs are listed in Table 4.1. Boundary layer displacement thickness, based on $\delta^* = 1/8a$ (Keith, *et. al.*, 1992) where a is pipe radius, is 9.8 mm. Static pressure

measurements indicate a friction factor of $f = 0.011$ (hydraulically smooth) and a friction velocity of $u_\tau/U_0 = 0.032$.

Table 4.1 Measured flow parameters for fully developed pipe flow

Accelerometer ring location, direction	U_0 (m/sec)	u_τ/U_0	δ^* (mm)
$x/2L = 1/2, r$	6.49	0.032	9.75
$x/2L = 1/3, r$	6.80	0.032	9.75
$x/2L = 1/6, r$	6.49	0.032	9.75
$x/2L = 1/2, \phi$	6.43	0.031	9.75
$x/2L = 1/6, z$	6.40	0.032	9.75

Because data from the separate runs are recorded at slightly different speeds and need to be compared and in some cases averaged together, the pressure and acceleration data are all scaled to a common reference speed of 6.1 m/sec. The pressure spectra are effectively non-dimensionalized using dynamic pressure and Strouhal number and then re-dimensionalized at 6.1 m/sec. Therefore, the levels are multiplied by $(6.1/U_0)^4$ and the frequencies are multiplied by $6.1/U_0$. The acceleration spectra are scaled by a ratio of TBL forces (levels are multiplied by $(6.1/U_0)^6$) while the accompanying frequencies are left unchanged since the frequency shift in the hydrodynamic forcing function is small and the cylinder resonance frequencies don't change.

Convection velocity (or phase velocity) can be computed from the phase between pairs of dynamic pressure sensors in the streamwise direction,

$$U_c \approx -\frac{\omega \xi_1}{\theta(\omega, \xi_1)} .$$
(4.3)

Values for normalized convection velocity, U_c/U_o , are plotted in Figure 4.1 from the

two pressure sensor pairs with the shortest streamwise separation distances, 2.54 cm and

5.08 cm. Coherence between even the most closely spaced pair diminishes above 400 Hz,

therefore sensors pairs with greater separation do not add any additional information to

the plot. These data are plotted along with an estimate for convection velocity suggested

by Ko (1993) based on work by Bull (1967) where,

$$\frac{U_c}{U_o} \cong 0.6 + 0.4e^{-0.8\omega \delta^*/U_o} .$$
(4.4)

Above 200 Hz, the Ko approximation reasonably represents the measured data. Since the

resonance frequencies of all modes in this study are above 200 Hz, the Ko approximation

is used throughout this work to represent convection velocity for all subsequent analysis.

Measured autospectra from the seven pressure sensors are averaged together for

the three flow runs with radially oriented accelerometers and shown in Figure 4.2. Both

the as-measured and signal removed TBL spectra are shown. The peaks removed from

the measured spectra below 100 Hz are likely acoustic pressures as they are removed due

to coherence with pressure sensors mounted on the opposite pipe wall. Durant and Robert

(2000) suggest the lowest order longitudinal acoustic mode for conditions of this

experiment should occur at roughly 30 Hz. Smaller peaks in the measured pressures

above 100 Hz are likely induced by local pipe vibration as they are removed due to

coherence with accelerometers installed adjacent to the pressure sensors.

Figure 4.2 also includes two theoretical curves: the Chase model of TBL frequency spectra (Equation 2.12 with the high frequency exponential decay factor based on Lysak (2006)) plotted for these conditions, and the actual signal a sensor of the size used for these measurements is expected to measure. The high frequency attenuation visible in the measured data and reflected in the green curve is due to the well known effect of area averaging over the sensor (Corcos, 1963). Fluctuating pressure scales, smaller than the sensor face, integrate to nearly zero or cancel one another to reduce the measured TBL pressure. The larger the sensor face the lower in frequency the attenuation occurs. This attenuation is a measurement artifact and does not reflect the actual pressure on the surface of the structure. To determine the expected area averaged frequency spectrum, the Chase TBL wavevector pressure spectrum is multiplied by a sensor response function, $H(k_1, k_3)$, and integrated over all wavenumbers, such that

$$\phi(\omega) = \int_{-\infty}^{\infty} \int_{-\infty}^{\infty} P(k_1, k_3, \omega) |H(k_1, k_3)|^2 \, dk_1 dk_3, \tag{4.5}$$

where for a circular transducer with radius, R,

$$H(\tilde{k}R) = \frac{2J_1(\tilde{k}R)}{\tilde{k}R} \quad \text{and} \quad \tilde{k} = \left(k_1^2 + k_3^2\right)^{1/2}.$$

The integrated Chase curve shows good agreement with the measured data. Therefore, the Chase frequency spectrum (with exponential factor included) is a good estimate of the true wall pressure spectrum and is used in subsequent analyses.

An example of a spectrogram from an accelerometer on the cylinder acquired with flow through the test-section at 6.1 m/s is shown in Figure 4.3. Visible in the plot are the times at which flow through the pipe was started and stopped. Below 2000 Hz are

obvious cylinder resonances which appear as horizontal lines. Above 3500 Hz is evidence of periodic cavitation bursts.

Measured cylinder vibration spectra in the radial direction in response to TBL excitation for the three different radial accelerometer ring locations are averaged together, scaled to 6.1 m/s, and shown in Figure 4.4. Both the as-measured and signal removed spectra are shown. The signal removed vibration levels are decomposed into circumferential Fourier components which reveal low-order cylinder modes from n=2 to n=5 below 2000 Hz. These resonance peaks represent the TBL induced cylinder vibration levels from which the low wavenumber TBL pressures can be determined.

4.2   Modal Analysis Results

To estimate TBL induced cylinder vibration from modal forces using Equation 2.21, four modal parameters are needed to compute vibration estimates for each mode: resonance frequency and damping (obtained from the measured flow data), and mode shape and modal mass (obtained from the experimental modal analysis). Resonance frequency and damping for the measured flow induced vibration data are estimated based on the resonance peak frequency and the half-power points as described in Chapter 3. Table 4.2 includes values for the modal parameters extracted from the flow data for identified modes which have relatively low damping.

Mode shapes and modal masses for corresponding resonance frequencies are determined from the modal analysis data. A plot of the surface averaged accelerance from the modal analysis measurements, decomposed into circumferential Fourier components,

is shown in Figure 4.5. The modal analysis data shows much of the same spectral content as the measured cylinder vibration due to flow excitation shown in Figure 4.4.

There are slight differences in resonance frequency and damping between the two data sets especially at higher frequency as indicated by the values in Table 4.2. For example, comparing Figure 4.5 with Figure 4.4 reveals the n=5 resonance peaks with flow are higher in frequency and less damped than the corresponding modal analysis peaks. This is likely due to disassembling and reassembling the test apparatus between measurement periods which introduced slight structural differences rather than the effect of flow through the cylinder. Preliminary modal analysis and flow data where disassembly between measurement periods did not occur does not show this difference.

Table 4.2 Measured modal parameters for water-filled cylindrical shell used to estimate TBL wall pressure

Mode n,m	Res. Freq. (Hz) Modal Analysis	Damping (%) Modal Analysis	Modal Mass (Kg)	Res. Freq. (Hz) Flow	Damping (%) Flow	Low wavenumber $10\log_{10}\left(\dfrac{P(k,\omega)}{\phi_{pp}k_c^{-2}}\right)$
2,1	300	0.007	3.8	301	0.007	-38
3,1	517	0.003	3.0	517.5	0.003	-41
3,2	659	0.005	2.5	660	0.009	-40
3,3	907	0.009	2.4	910	0.009	-42
3,3	927	0.007	2.9	932	0.006	-41
4,1	1012	0.003	1.7	1018	0.002	-43
4,2	1076	0.005	1.7	1084	0.003	-42
4,3	1207	0.005	1.5	1221	0.003	-41
4,4	1411	0.01	1.5	1434	0.004	-43
5,1	1702	0.006	2.8	1726	0.002	-37
5,2	1756	0.006	2.8	1777	0.002	-40
5.3	1834	0.008	1.9	1862	0.002	-40
5,4	1969	0.01	1.7	1999	0.002	-42

The modal mass for each individual mode are a combination of some fraction of the aluminum shell mass (2.5 Kg) involved in modal displacement and some fraction of the mass of the water (11 Kg within the shell boundaries) entrained in the modal displacement. The modal masses for identified modes determined using Equation 2.20 are listed in Table 4.2 and range from 1.5 Kg for the higher-order radial modes to 3.8 Kg for the lowest order radial mode.

The cylindrical shell mode shapes determined from the modal analysis and listed in Table 4.2 involve displacements primarily in the radial direction. Representative mode shapes and their corresponding sensitivity functions for the primarily radial modes are shown in Figure 4.6. For the lowest order n=0 and n=1 modes, only the n=1, m=1 mode is clearly visible in the modal test data in Figure 4.5. None of the radial n=0 modes can be identified. The analytical shell model results suggest the radial n=0 modes have a very low response due to internal fluid loading. Also, it is likely the damping for these low-order modes is relatively high (as is indicated by the 1,1 mode) which makes them difficult to excite and identify.

Figures 4.7 and 4.8 show the measured sensitivity functions for identified cylindrical shell modes and the location of the primary lobes relative to the TBL wavenumber spectrum. The primary lobes all fall completely outside the acoustic domain in the k_3 direction and are centered below $k_1/k_c < 0.01$ in the k_1 direction.

4.3 Estimating Low Wavenumber Pressure Levels from TBL Vibration Data

Using the modal parameters and measured mode shapes for the modes listed in Table 4.2 and assuming a constant low wavenumber TBL pressure level at and around

the modal wavenumbers, the modal force is computed from Equation 2.22 for each mode. Cylinder vibration spectra are estimated from Equation 2.21 for the accelerometer locations measured with flow and reported in Figure 4.4 (three rings of twelve locations each). The constant low wavenumber pressure spectrum levels required to match each estimated resonance peak with the measured flow data are reported in Table 4.2 and plotted versus wavenumber in Figure 4.9.

Figure 4.9 shows the constant low wavenumber pressure spectrum levels derived from these experiments compared to historical data, along with representative curves from the three TBL wavenumber models described previously. The plotted values represent two-sided functions of k_1, k_3, and ω. The Chase point frequency spectrum (Equation 2.12 with high frequency exponential decay factor included) is used to convert the historical data from the form in which it was originally reported to the form of Figure 4.9. Although the primary lobes for these modes extend over a range of wavenumbers, each pressure value is represented at its maximum k_1 and k_3 value in Figure 4.9. As shown in Figure 4.8, the primary lobes for all modes fall completely outside the acoustic domain in the k_3 direction. Therefore, the modes identified in Table 4.2 and represented in Figures 4.7 - 4.9, provide an opportunity to evaluate the low wavenumber domain outside the acoustic domain. The acoustic domain cannot be specifically addressed with this dataset.

The low wavenumber pressure values derived from these experiments fall midway between the Smol'yakov and Chase TBL models and roughly 25 dB lower than the Corcos model. The levels extracted from these data are slightly below the lower bound of the measurements by Martin and Leehey (1977) and Farabee and Geib (1975).

However, Farabee and Geib suggest the data measured at the lowest speed during their experiment (represented by the four lowest values in level and wavenumber) are the least likely to be contaminated from convective and acoustic sources.

Chase (1980) suggests several model forms showing a power-law dependence to fit available low wavenumber data. The simplest of these forms is both scale independent and wavenumber white,

$$P\left(k_1, k_3, \omega\right)_{low-wavenumber} = C_0 \rho^2 u_t^6 \omega^{-3}. \tag{4.6}$$

Chase (1993) refers to a fit of the Martin and Leehey (1977) data with this form where $C_0 = 10^{-0.9}$ as the "Martin-Leehey" level which represents a single-sided function of k_1 in Equation 4.6.

Figure 4.10 shows the same data as Figure 4.9 replotted in the form both Martin and Leehey (1977) and Farabee and Geib (1975) originally reported their results. The pressure levels in this plot are single-sided in k_1 and are non-dimensionalized by dynamic pressure and displacement thickness rather than the frequency spectrum and convective wavenumber used in Figure 4.9. A constant low wavenumber value (depicted in Figure 4.9) corresponding to a point frequency spectrum which falls entirely within the universal range (where $P(\omega) \approx 1\rho^2 u_t^4 \omega^{-1}$) translates to a line in Figure 4.10 which has a slope of $\left(\omega\delta^*/U_\infty\right)^{-3}$. In the non-dimensional form of Figure 4.10, no wavenumber dependence can be determined. It is best to view this plot as representing all low wavenumber data without regard to where in the low wavenumber spectrum it occurs.

Martin and Leehey report a least squares fit to their data showing a slope of $\left(\omega\delta^{*}/U_{0}\right)^{-3.34}$. Farabee and Geib suggest their highest reduced frequency data (least likely to be contaminated) shows a $\left(\omega\delta^{*}/U_{0}\right)^{-4}$ dependence. This difference in slope is likely due to the difference in slope of the respective point frequency spectra. The Martin and Leehey data fall almost entirely within the universal range where $\phi(\omega) \sim \omega^{-1}$. The Farabee and Geib data extend into the viscous subrange region (exponential roll-off) where the frequency dependence of $\phi(\omega)$ is steeper than ω^{-1}.

Since Chase did not model the high frequency roll-off portion in his point frequency spectrum, Equation 4.6 does not adequately model the low wavenumber pressure levels at high reduced frequency. The exponential decay factor, $e^{-2.2(\omega v/u_{\tau})}$, can be appended to Equation 4.6 (as was done for Equation 2.12) to better fit the data shown in Figure 4.10. The dashed line in Figure 4.10 which runs through the Martin and Leehey data is plotted using

$$P\left(k_{1},k_{3},\omega\right)_{low-wavenumber} = C_{0}\rho^{2}u_{t}^{6}\omega^{-3}e^{-2.2(\omega v/u_{\tau})}, \tag{4.7}$$

where $C_{0} = 10^{-0.9}$.

The current data set is also plotted in Figure 4.10. The dashed line running through this data comes from plotting Equation 4.7 where $C_{0} = 10^{-1.25}$ which corresponds to the constant low wavenumber value for this data identified from Figure 4.9. The value of C_{0} determined for the current data is 3.5 dB below the "Martin-Leehey" level.

The non-dimensionalization scheme of Figure 4.9 suggests a slightly different form for the low wavenumber pressure levels, where

$$P\left(k_{1}, k_{3}, \omega\right)_{low-wavenumber} \approx H_{0} \phi(\omega) k_{c}^{-2}. \tag{4.8}$$

Equation 4.8 represents two-sided functions of k_{1}, k_{3}, and ω. For frequencies within or

above the universal range of $\phi(\omega)$ this leads to a wavenumber white form of pressure,

$$P\left(k_{1}, k_{3}, \omega\right)_{low-wavenumber} = H_{0} \rho^{2} u_{t}^{4} U_{c}^{2} \omega^{-3} e^{-2.2(\omega v/u_{\tau})}. \tag{4.9}$$

The current data shown in Figure 4.9 yields the constant, $H_{0} = 10^{-4.1}$. As in Figure 4.10,

this level represents a 3.5 dB reduction from the "Martin-Leehey" level, however Figure

4.9 also suggests the Martin and Leehey data measured at higher reduced wavenumbers

may be slightly elevated by the tail of the convective ridge.

Equation 4.9 reveals a dependence on convection velocity not present in the

modified simple Chase model of Equation 4.7. The point frequency spectrum dependence

modeled in Equations 4.8 and 4.9 contains a friction velocity to the fourth power and the

accompanying wavenumber dependence contains a convection velocity squared. The

current data suggest the low wavenumber domain of TBL pressures can be reasonably

represented using the wavenumber white forms of Equations 4.8 and 4.9.

4.4   Estimating Low Wavenumber Shear Stress Levels from TBL Vibration Data

In the same way that low wavenumber levels of normal wall pressure can be

determined from radial vibration measurements, shear stress levels in both the cross-flow

and streamwise directions can be determined from vibration measurements in the

circumferential and axial directions. However, it is more difficult to determine TBL shear

stress levels since nearly all cylinder modes are coupled in all three directions. Excitation

in any one direction produces displacement in all three directions, and the displacements

in all three directions are generally more sensitive to radial excitation than circumferential or axial excitation. This is evident in the analytical model results shown in Figures 2.11 and 2.12. Since TBL excitation produces wall pressure and wall shear stress simultaneously, vibration modes not directionally coupled represent the best opportunity to isolate excitation levels in each direction. The lowest order n=0, m=1 modes are best suited for this purpose since there are three unique modes, one associated with each coordinate direction, which contain little if any displacement in the other coordinate directions.

The analytical shell model with simply supported boundary conditions discussed in chapter 2 indicates the n=0, m=1 resonance frequencies in the radial, circumferential, and axial directions occur at 745 Hz, 2500 Hz, and 4300 Hz, respectively. The radial n=0, m=1 mode and resonance peak could not be identified in either the experimental modal analysis data or the flow excited cylinder vibration data. However, both the circumferential and axial n=0, m=1 modes are readily evident in both experimental data sets. Figures 4.11 - 4.14 show both flow excited cylinder vibration data (decomposed into circumferential Fourier components) and experimental modal analysis data in the circumferential and axial directions.

In the flow induced vibration data with circumferentially oriented accelerometers in Figure 4.11, the n=0, m=1 mode occurs near 2100 Hz and clearly dominates the entire circumferential vibration spectrum between 1500-2500 Hz. The modal analysis results shown in Figure 4.12 suggests this circumferential mode is primarily driven by a circumferential excitation. Both the flow and modal data sets reveal a pure n=0

contribution to the n=0, m=1 resonance peak. The experimental modal data looks similar to the analytical shell model results shown in Figure 2.11.

In the flow data of Figure 4.13, the axial n=0, m=1 mode occurs near 3500 Hz. The modal data in Figure 4.14 again suggests an axial excitation is responsible for exciting this mode during pipe flow. In both the axial modal analysis data and flow data sets, several n=0 peaks are evident in the vibration spectra between 2-4 kHz. Inspection of the three-dimensional mode shapes reveals only the two highest resonance peaks are associated with primarily n=0, m=1 modes in the axial direction. The other lower frequency peaks are also primarily n=0, m=1 modes, but contain significant displacement in either the radial or circumferential directions. These modes do not appear in the analytical solution. The two resonance peaks near 3500 Hz best represent the axial n=0, m=1 mode evident in the analytical results. The mode shapes associated with these two peaks are very similar to one another suggesting the single n=0, m=1 mode in the analytical model split into two similar modes in the actual structure. While these modes are dominated by n=0 content, the modal analysis data indicates they also contain significant n=1 contribution. The flow data indicate, however, these modes are more purely n=0 than the modal analysis data.

Results from the experimental modal data for the axial n=0, m=1 mode shown in Figure 4.14 do not match the analytical shell model results shown in Figure 2.12 as well as they do for corresponding results for the circumferential n=0, m=1 mode. The simply supported boundary conditions of the analytical model adequately represent the dynamics of the circumferential n=0, m=1 mode for the actual experimental cylinder. Simply supported boundary conditions do not adequately represent the dynamics of the axial

n=0, m=1 mode for the actual experimental cylinder. The pinned or clamped boundary conditions in the actual structure have a significant effect on the axial n=0, m=1mode and very little effect on the circumferential n=0, m=1mode. Slight imperfections in the experimental cylinder may also more greatly affect the axial n=0, m=1 mode than the circumferential n=0, m=1 mode. Therefore, mode shapes and modal masses determined from the analytical model are more reliable for the circumferential n=0, m=1mode than for the axial n=0, m=1mode.

Inspection of the mode shapes for these two modes shown in Figures 4.15 and 4.16 reveals general n=0, m=1 motion, however displacement at the four drive point locations is low relative to the non-drive point locations. Because additional mass was added to the small aluminum cubes at all experimental grid locations to compensate for the added mass of the accelerometers at the drive point locations, there is no obvious reason for this result. For a variety of reasons, the quality of measured data for many experimental modal data sets tends to deteriorate as frequency increases. It is also generally more difficult to extract valid modal parameters for more highly damped modes in a region of high modal density. Therefore, in an attempt to simulate mode shapes which should better represent the actual n=0 motion of the structure for these relatively highly damped, high frequency modes, the measured modal transfer function data was filtered to isolate the n=0 contribution to vibration. To accomplish this, the measured data was transformed from the spatial domain to the wavenumber domain and decomposed into the Fourier components using Equation 3.6. The non n=0 components (n=1 through n=6) were set to zero after which the data was transformed back to the spatial domain. This filtered data set was again processed using standard modal analysis techniques as

before. The filtered and unfiltered mode shapes for the n=0, m=1 modes are normalized to a peak value of one in Figures 4.15 and 4.16 consistent with Equation 2.20. Although additional processing is required, the filtered mode shapes appear to be more physically realistic.

Determining modal mass using Equation 2.20 involves use of the mode shape function at the drive point locations. The low displacement at the drive point locations for the unfiltered mode shapes yields a relatively low modal mass. The higher displacement at the drive point locations for the filtered mode shapes yields a much higher modal mass. Modal parameters determined for the measured circumferential and axial n=0, m=1 modes for both unfiltered and filtered mode shapes are reported in Table 4.3.

Table 4.3 Measured modal parameters for water-filled cylindrical shell for n=0 modes used to estimate shear stress

Mode n,m	Res. Freq. (Hz) Modal Analysis	Damping (%) Modal Analysis	Modal Mass (Kg)	Res. Freq. (Hz) Flow	Damping (%) Flow	Low wavenumber $10\log_{10}\left(\dfrac{S(k,\omega)}{P(k,\omega)}\right)$
Using unfiltered modal data						
$0,1\phi$	2122	0.033	0.28	2145	0.033	+1 dB
$0,1z$	3367	0.017	1.6	3360	0.017	+7 dB
$0,1z$	3463	0.012	1.5	3465	0.012	+6 dB
Using filtered n=0 modal data						
$0,1\phi$	2105	0.034	2.6	2145	0.034	+10 dB
$0,1z$	3370	0.012	33.5	3360	0.012	+20 dB
$0,1z$	3461	0.010	29.5	3465	0.010	+19 dB

The modal masses determined from the analytical model for the circumferential and axial n=0, m=1 modes are both 1.25 Kg. As discussed previously, because of the difference in boundary conditions between the analytical model and the actual structure,

this modal mass is more reliable for the circumferential n=0, m=1mode than for the axial n=0, m=1mode.

Using the modal parameters from Table 4.3, circumferential and axial cylinder vibration spectra are estimated from Equation 2.21 for the accelerometer locations measured with flow and reported in Table 4.1. The constant low wavenumber shear stress levels required to match the estimated resonance peaks with the measured flow data for the n=0, m=1 modes are also reported in Table 4.3 relative to the constant low wavenumber value determined for normal pressure, where $C_0 = 10^{-1.25}$. The unfiltered circumferential mode shape (2100 Hz) yields a cross-flow low wavenumber shear stress level which is 1 dB above the pressure level. The unfiltered axial mode shapes (3500 Hz) yield streamwise low wavenumber shear stress levels which are roughly 6 dB above the pressure level. Using the filtered mode shapes, the cross-flow and streamwise shear stress levels at these frequencies become 10 dB and 20 dB above the pressure level, respectively.

The shear stress levels determined using filtered mode shapes are appreciably higher than those determined using unfiltered mode shapes. Only a small part of the difference is a result of integrating the different sensitivity functions over wavenumber (Equation 2.22). Most of the difference is the result of differing modal masses determined for the different mode shape functions. This higher modal mass requires a correspondingly higher modal force (and associated low wavenumber shear stress level) to make the estimated acceleration levels match the measured resonance peak levels from the flow data.

The low wavenumber shear stress levels determined from the filtered n=0, m=1 modes shapes are normalized by dynamic pressure and displacement thickness and are shown as a function of reduced frequency in Figure 4.17. The line representing constant low wavenumber pressure levels determined from Figure 4.10 is included for comparison. Also shown for reference is the value of the Chase (1993) streamwise shear stress model at zero wavenumber. The Chase values are multiplied by a factor of two to account for both positive and negative streamwise wavenumbers being represented in this figure. The red and blue lines in Figure 4.17 will be described later.

Once trial shear stress levels have been established from modes dominated by motion in the axial and circumferential directions in isolation, it is helpful to determine whether these same low wavenumber levels explain the response of modes at other frequencies which have coupled displacement in multiple directions. A few modes which were previously left out of the evaluation for normal pressure are included for this purpose. These modes all have higher damping than those evaluated for normal pressure. And, while they are all still dominated by displacement in the radial direction, they all have higher relative displacements in the circumferential or axial directions than the modes used to evaluate normal pressure listed in Table 4.1. Modal parameters for these additional modes are listed in Table 4.4.

Table 4.4 Measured modal parameters for water-filled cylindrical shell used to estimate shear stress

Mode n,m	Res. Freq. (Hz) Modal Analysis	Damping (%) Modal Analysis	Modal Mass (Kg)	Res. Freq. (Hz) Flow	Damping (%) Flow
1,1	444	0.039	18	446	0.04
1,1	503	0.043	9	503	0.04
2,2	644	0.03	3.2	643	0.02
2,3	1094	0.076	2.3	1125	0.022
3,4	1255	0.035	2.2	1258	0.029
3,4	1276	0.030	2.4	1292	0.016

In order to determine whether constant low wavenumber shear stress levels established for the n=0, m=1 modes can explain the response of modes at other frequencies, one must know the frequency dependence of the TBL shear stress spectrum. In the same way that the TBL pressure spectrum can be appropriately separated into independent functions of frequency and wavenumber (Equation 2.8),

$$P(k_1, k_3, \omega) = \phi_2(\omega) F_2(k_1, k_3), \tag{4.10}$$

it is convenient and appropriate to separate the TBL wavevector-frequency shear stress spectra into independent functions of frequency and wavenumber,

$$S_1(k_1, k_3, \omega) = \phi_1(\omega) F_1(k_1, k_3) \text{ - streamwise direction,}$$

$$S_3(k_1, k_3, \omega) = \phi_3(\omega) F_3(k_1, k_3) \text{ - cross-flow direction.} \tag{4.11}$$

Chase (1993) proposed the only known model of the shear stress frequency spectrum in the streamwise direction only. This model is normalized by inner variables (u_τ and ν / u_τ) and plotted in Figure 4.18. Also plotted in this figure are: a sample of very limited experimental shear stress data (Colella and Keith, 2003), low Reynolds number

shear stress DNS results (Jeon, *et. al.*, 1999), and the pressure frequency spectrum used in this study based on Chase (1980). The experimental data and DNS results collapse reasonably well with the Chase (1993) shear stress model with some scatter occurring at high frequencies. The pressure spectrum model is very nearly a constant 15 dB higher than the shear stress model in the universal range (as noted by Chase, 1993), but exceeds the shear stress levels by more than 15 dB in the high frequency viscous subrange. Because of limited available data for the shear stress frequency spectrum and the uncertainty of this spectrum at high frequency, for convenience in this work, the shear stress frequency dependence is assumed to be the same as the pressure frequency dependence at high frequency. Jeon, *et. al.* (1999) report streamwise and cross-flow shear stress frequency spectra results which are very similar to one another except at very low reduced frequencies. Therefore, the exponential decay factor, $\exp\left(-2.2\left(\omega v/U_\tau\right)\right)$, used in the normal pressure frequency model is assumed to represent the frequency dependence for both directions of the shear stress frequency spectra as well.

The red and blue lines in Figure 4.17 which run through the data points for the n=0, m=1 circumferential and axial modes and extend to low frequency are the result of plotting Equation 4.7 where the value for C_0 is 10 and 20 dB higher than the value used for normal pressure. These lines represent constant low wavenumber TBL shear stress levels over a broad frequency range which are 10 and 20 dB higher than pressure.

The constant low wavenumber levels represented in Figure 4.17 for pressure, cross-flow shear stress, and streamwise shear stress are used to estimate acceleration levels using Equation 2.21 from 0 - 2000 Hz for all modes listed in Tables 4.2 and 4.4.

First, the low wavenumber pressure level corresponding to $C_0 = 10^{-1.25}$ from Figure 4.17

is used as the basis for the modal force due to pressure only. The resulting acceleration

levels are shown in Figure 4.19. As expected, the TBL normal pressure is sufficient to

excite the modes with relatively high radial displacement and low damping (Table 4.2

modes) to levels which match the measured cylinder vibration data subjected to flow.

However the modes listed in Table 4.4 are not sufficiently excited by these pressures to

vibration levels which match the measured flow data.

The estimated acceleration levels resulting from modes excited by cross-flow

shear stress only, corresponding to a low wavenumber level which is 10 dB higher than

that used for pressure ($C_0 = 10^{-0.25}$), are shown in Figure 4.20. The resonance peaks for all

modes are well below the measured flow data except for the n=1, m=1 modes near 500

Hz. The same low wavenumber shear stress level required to match the measured

vibration data in the circumferential direction at 2100 Hz, is adequate to explain the

measured radial vibration levels for these specific modes. This suggests that cross-flow

shear stress generates the dominant excitation force for these modes and can be

represented by a constant low wavenumber value over the frequency range from 500 to

2100 Hz.

Finally, estimated acceleration levels resulting from modes excited by streamwise

shear stress only, corresponding to a low wavenumber level ($C_0 = 10^{0.75}$) which is 20 dB

higher than that used for pressure, are shown in Figure 4.21. While these shear stress

levels provide a satisfactory match for the more highly damped 2,3 and 3,4 modes, the

resulting resonance peaks for several other modes (for example 2,2 and 3,3) exceed the

measured flow data by several decibels. In addition, acceleration levels estimated for all

three drives must be summed together and compared to the measured flow data, the results of which are plotted in Figure 4.22. Low wavenumber streamwise shear stress levels which are 20 dB above the pressure levels appear to be too high to satisfactorily explain the majority of the measured flow vibration data.

Possible explanations exist as to why the streamwise shear stress levels are too high based on analysis of the n=0, m=1 axial modes at 3500 Hz. From the spectrogram of vibration flow data shown in Figure 4.3, cavitation bursts are visible in the accelerometer data down to about 3500 Hz. Cavitation may have elevated the cylinder vibration levels beyond those due to TBL excitation only. Also, the single axial n=0, m=1 mode in the analytical model apparently split into multiple modes in the experimental cylinder with slightly different resonance frequencies likely due to structural imperfections. This makes determining accurate modal parameters more difficult. The n=0, m=1 experimental circumferential mode at 2100 Hz was not affected by either cavitation or mode splitting.

The constant low wavenumber cross-flow shear stress level measured near 2100 Hz and confirmed at 500 Hz suggest: 1) a constant universal wavevector function exists for shear stress as it appears to for pressure, and 2) the cross-flow results are more reliable than the streamwise results. Limited DNS studies of shear stress at low Reynolds number suggest that cross-flow and streamwise low wavenumber levels are comparable to one another. In view of the greater reliability of the cross-flow results, past research, and current results suggesting streamwise shear stress levels 20 dB above pressure are too high, it is reasonable to assume that the low wavenumber cross-flow results apply for both cross-flow and streamwise shear stress. Therefore, both components are assumed to be 10 dB higher than normal pressure. Figure 4.23 shows estimated cylinder acceleration

levels resulting from excitation by normal pressure only compared with those resulting

from both pressure and shear stress excitation. Both the low wavenumber cross-flow and

streamwise shear stress levels in Figure 4.23 correspond to a level which is 10 dB higher

than that used for pressure. These pressure and shear stress levels provide a reasonable

match with measured flow vibration data where shear stress excitation increases the

radial vibration response for certain directionally-coupled cylinder modes.

Suggesting the TBL low wavenumber shear stress levels are 10 dB above those of

pressure has a few implications. A summary of the limited research regarding the shear

stress frequency spectrum indicates it is roughly 15 dB below the pressure frequency

spectrum. This 15 dB difference would be reflected in convective peak levels if pressure

and shear stress were compared in the wavenumber domain using absolute levels. Results

from this research, along with others, indicate that low wavenumber pressure is roughly

40 dB below its convective peak level. Therefore, in order for the low wavenumber shear

stress levels to be 10 dB higher than those of pressure, low wavenumber shear stress is

likely no more than 15 dB below its convective peak level. In other words, the convective

peak in the shear stress wavevector spectrum is much less prominent than in the pressure

wavevector spectrum.

Also, results in this study indicating shear stress levels exceed pressure levels at

low wavenumber are in direct contrast to the limited past research on this topic. As

evident by the Chase (1993) model of streamwise shear stress shown in Figure 4.17,

Chase suggests the low wavenumber shear stress levels are comparable to those of

measured pressure. Hespeel (1998) also reported measured low wavenumber streamwise

shear stress levels similar to those of pressure. Jeon, *et. al.* (1999) report a 20 dB spread

of normalized shear stress levels at low wavenumbers for various frequencies. They suggest there are no universal normalized shear stress functions of wavenumber valid at all frequencies as these results seem to support and as is the case for various models of TBL pressure.

Because the current shear stress results differ from past research, it is useful to examine experimental circumstances which may have led to misleading results. The measured shear stress levels in this study, which exceed pressure levels by 10 dB, are based on low-order n=0, m=1 modes which are susceptible to acoustic excitation. The low-order n=0, m=1 sensitivity function primary lobes are centered at zero wavenumber, completely inside the acoustic domain, and therefore can be contaminated by acoustic sources. Even the n=1,m=1 modes at 500 Hz used to validate the circumferential shear stress levels have primary lobes which extend into the acoustic domain making them somewhat susceptible to acoustic contamination. In contrast, the primary lobes for the sensitivity functions of the higher order modes used for determining normal pressure are all completely outside the acoustic domain. These modes effectively filter out all acoustic sources that may be present.

Arguments against acoustic contamination of the low-order circumferential and axial modes include a test facility which is very quiet. Slight cavitation was present, but was limited to frequencies above 3500 Hz. In addition, acoustic pressures should act normal to the bounding surface and affect only normal pressure. They should not affect shear stress.

$$\frac{U_c}{U_o} \cong 0.6 + 0.4 e^{-0.8\omega\delta^*/U_o}$$

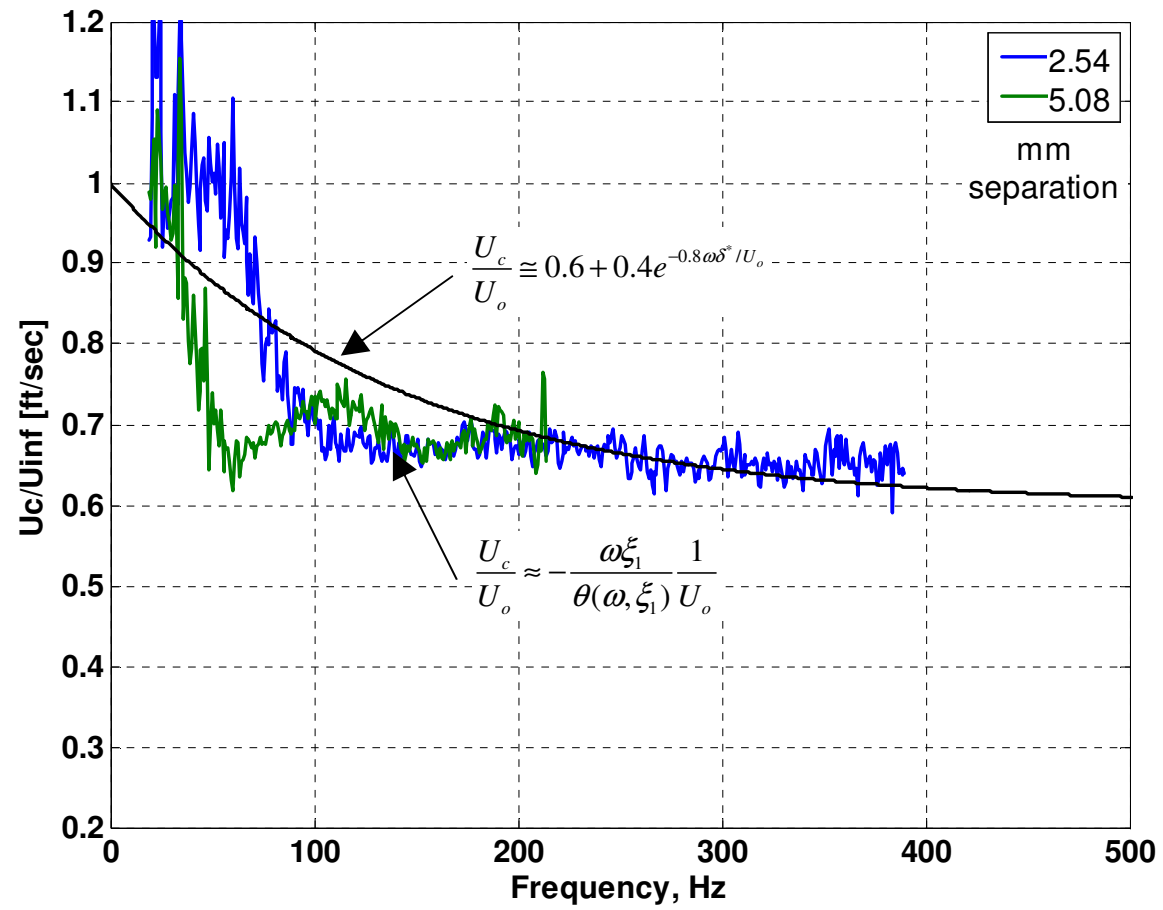$$\frac{U_c}{U_o} \approx -\frac{\omega\xi_1}{\theta(\omega,\xi_1)}\frac{1}{U_o}$$

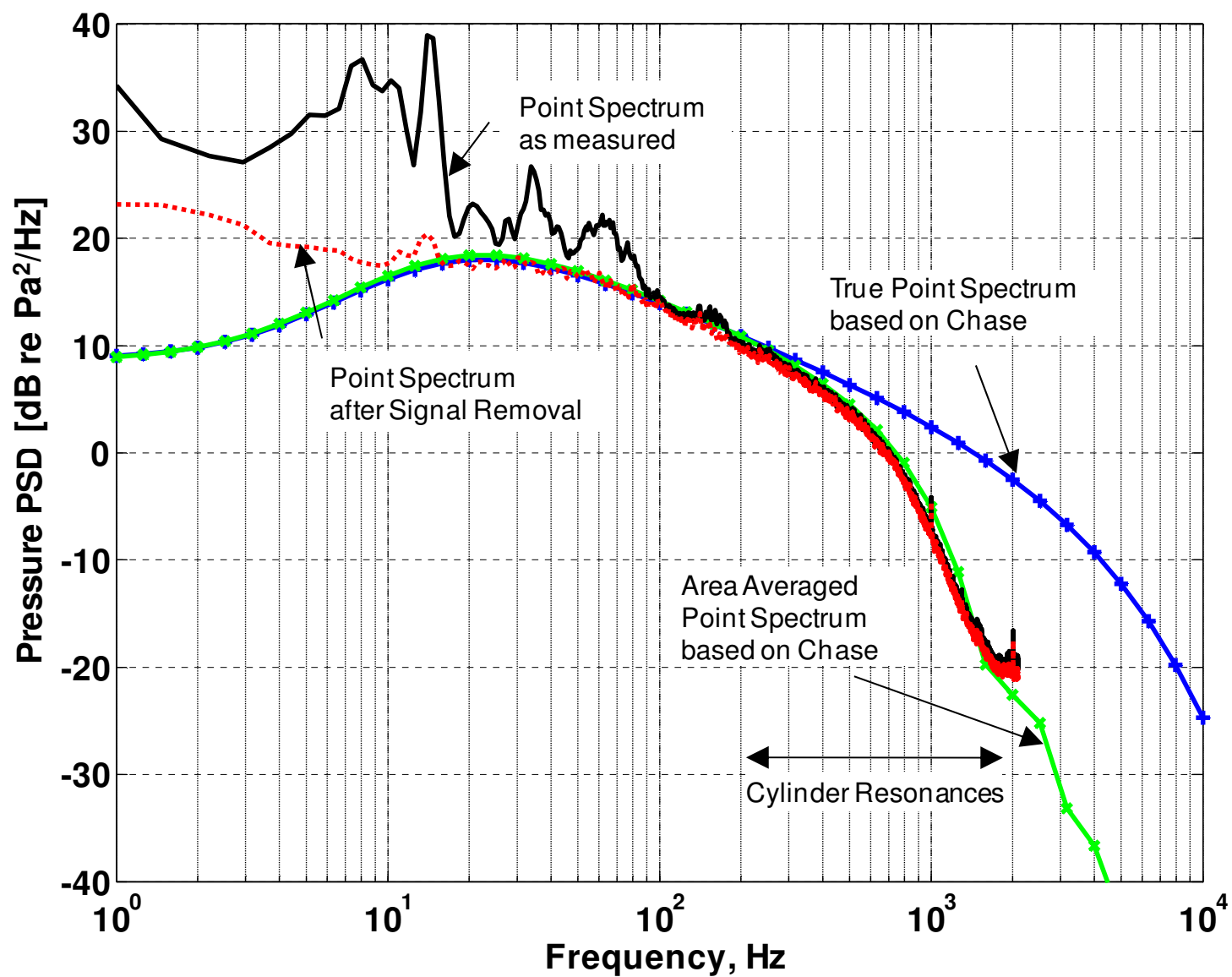Figure 4.1 Comparison of measured convection velocity with empirical model

Figure 4.2 Measured TBL point pressure frequency spectrum compared with Chase model accounting for sensor area averaging
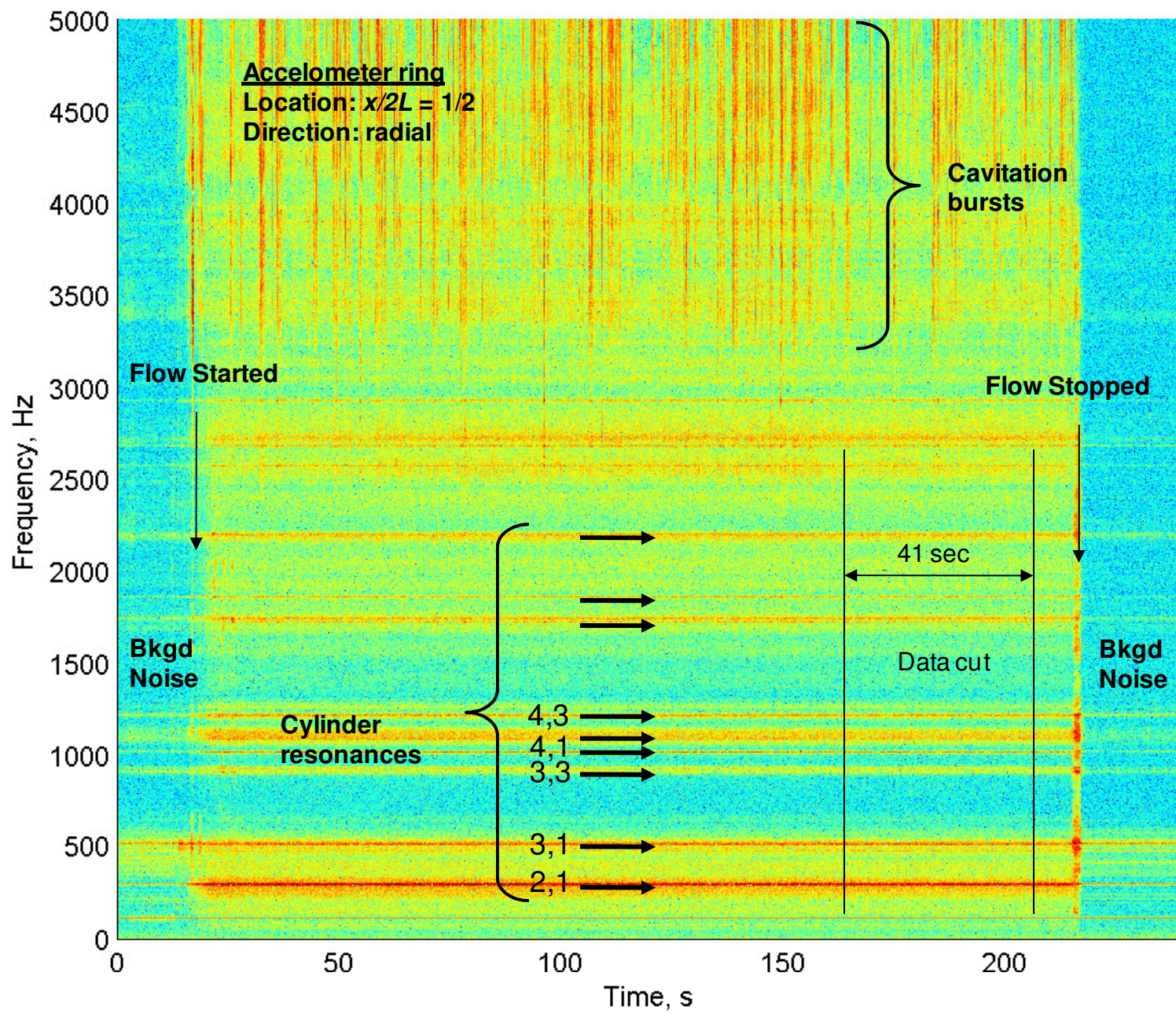
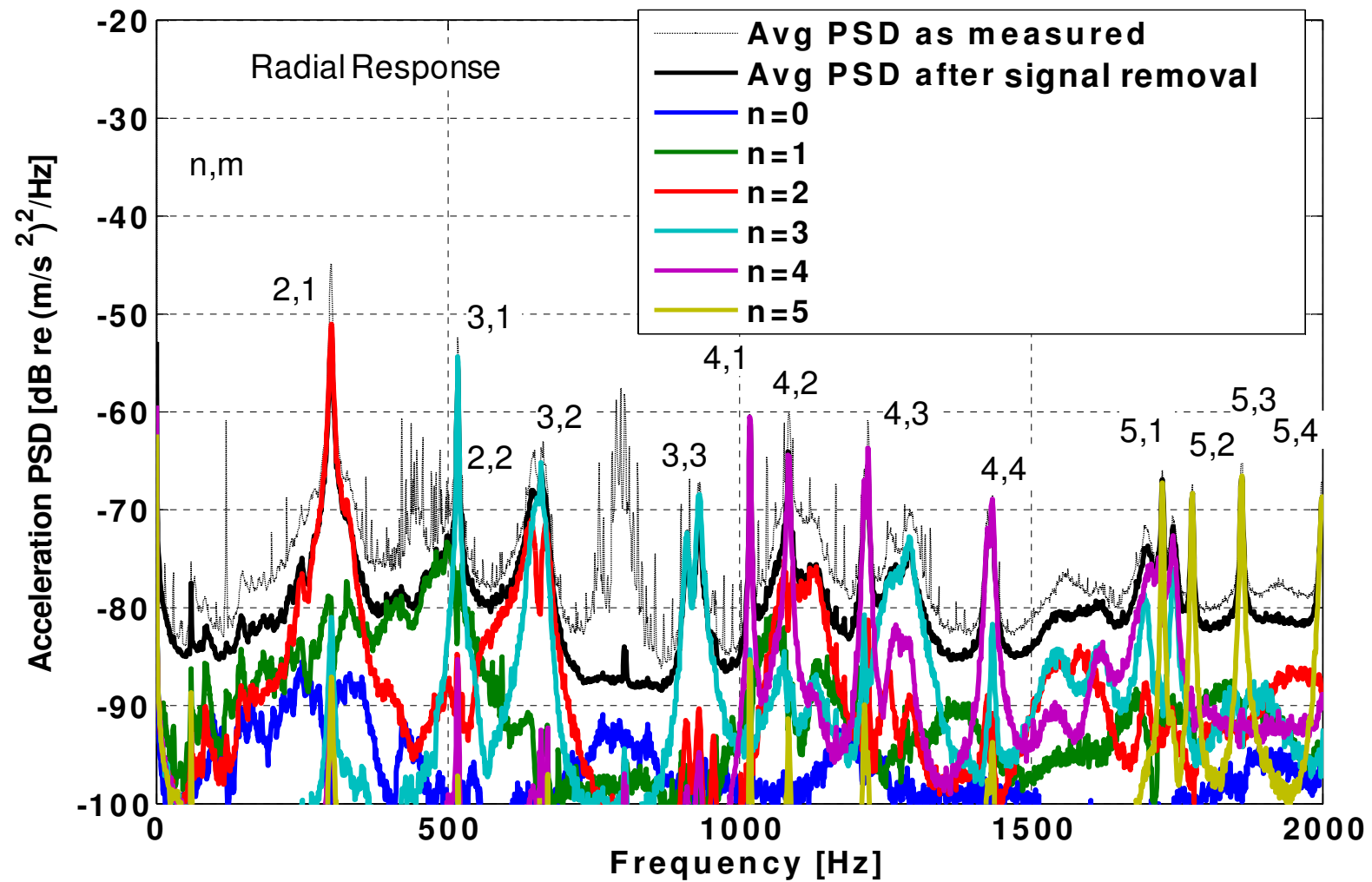Figure 4.3 Spectrogram of accelerometer data on cylinder with flow

Figure 4.4 Measured average radial cylinder vibration with flow decomposed into circumferential Fourier components
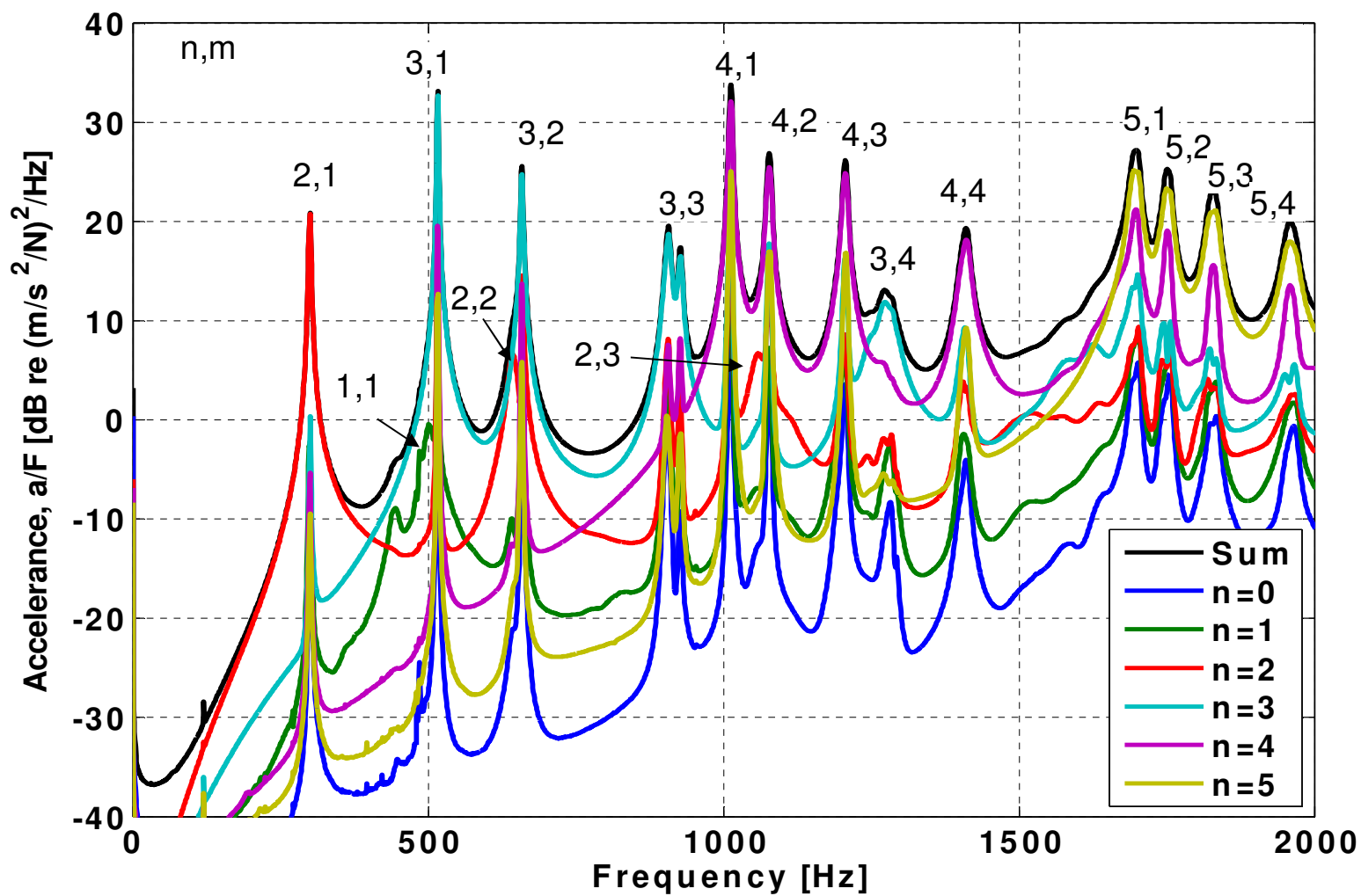
Figure 4.5 Experimental modal analysis average radial cylinder vibration decomposed into circumferential Fourier components
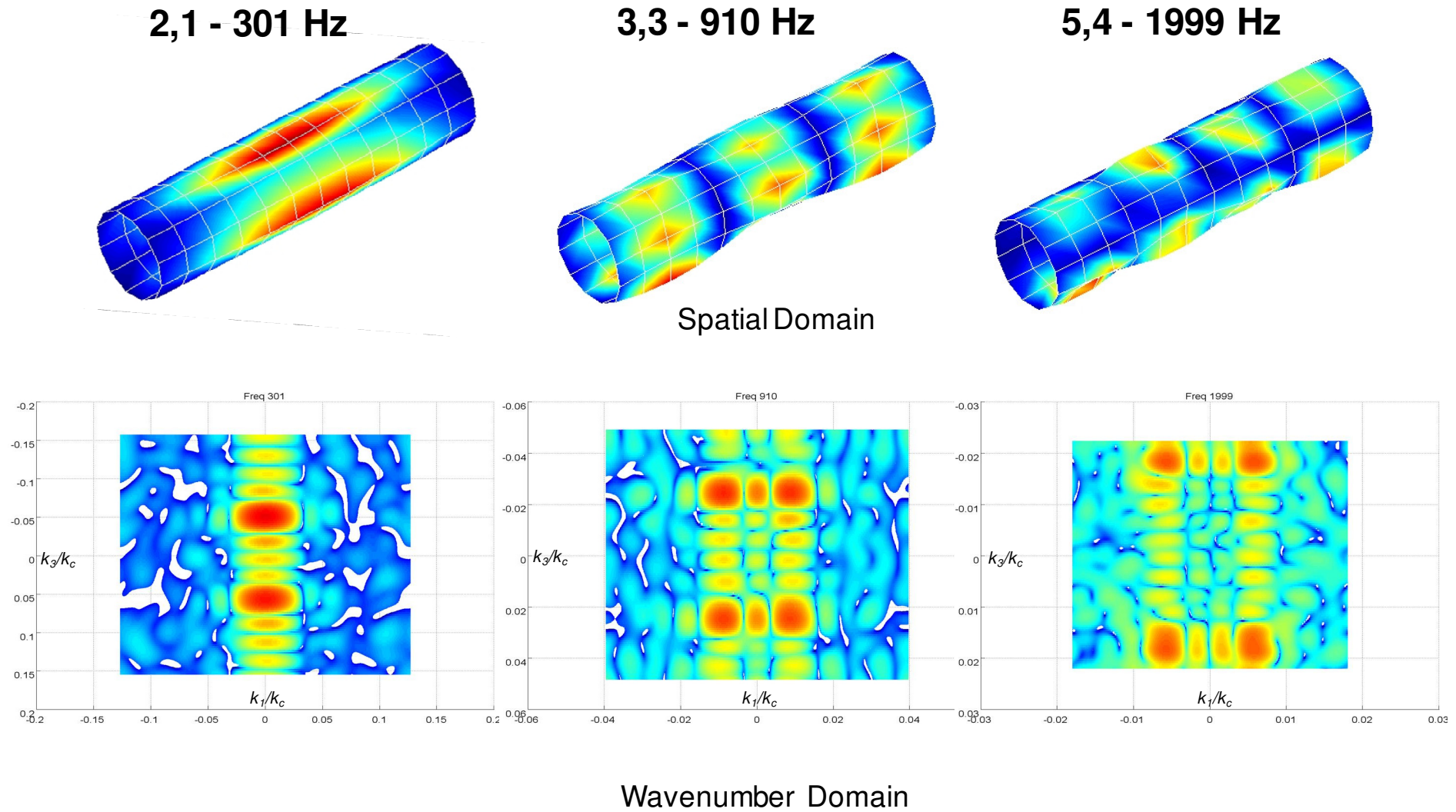
2,1 - 301 Hz   **3,3 - 910 Hz**   **5,4 - 1999 Hz**

Spatial Domain

Wavenumber Domain

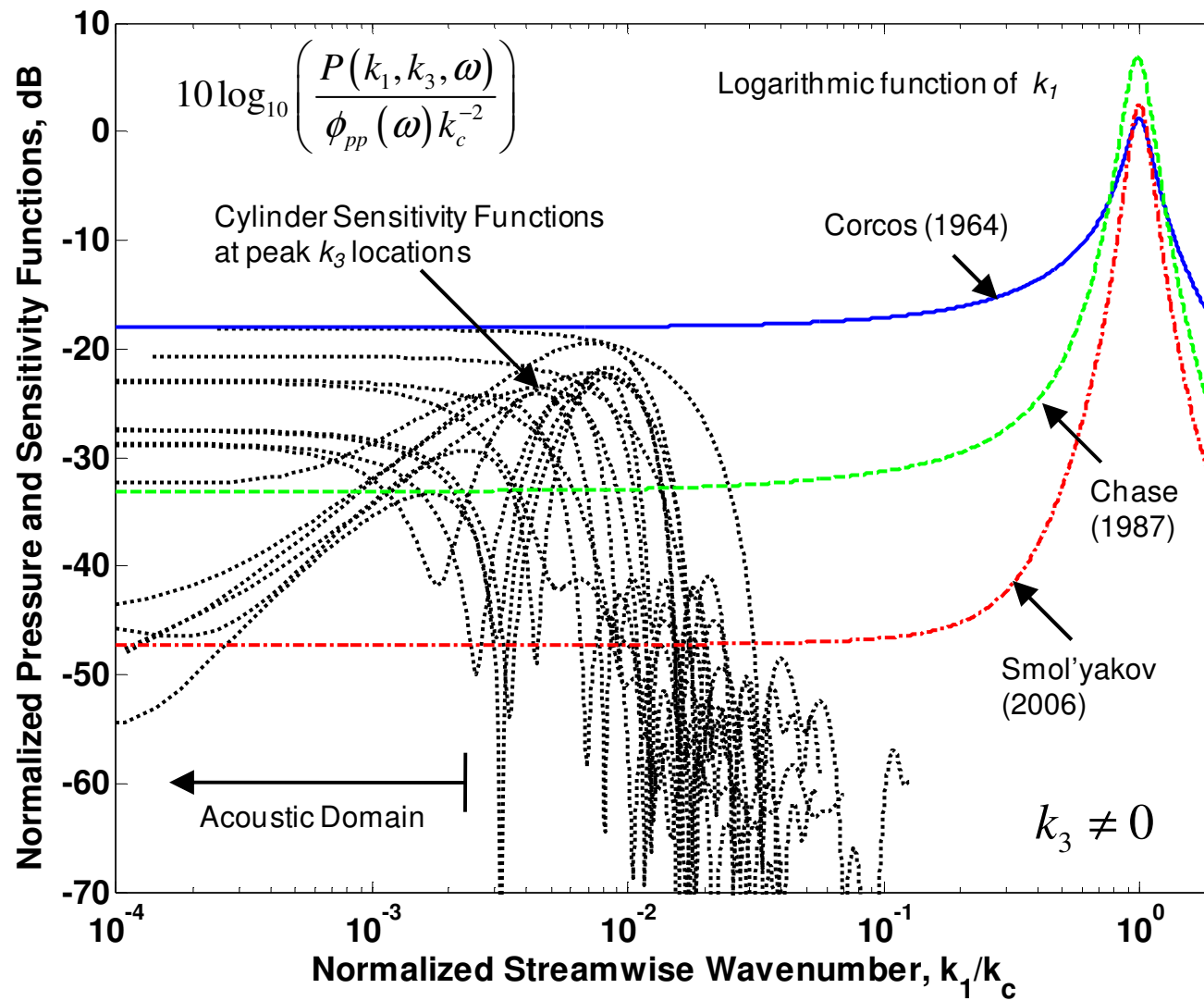Figure 4.6 Representative mode shapes and sensitivity functions for radial modes used to determine TBL pressure

Figure 4.7 Relationship between the streamwise wavenumber spectrum and measured sensitivity functions for identified cylindrical shell modes
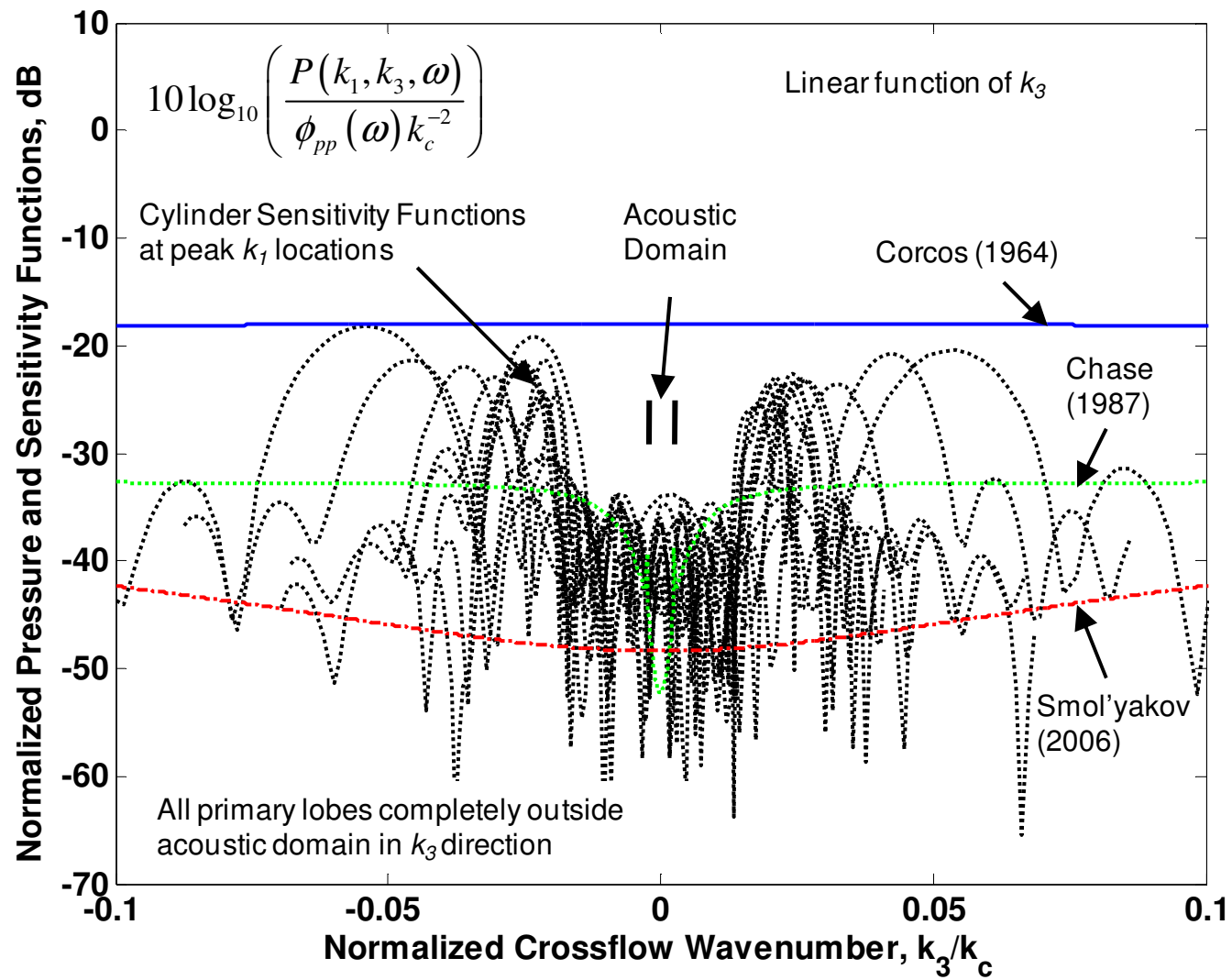
The y-axis is labeled **Normalized Pressure and Sensitivity Functions, dB** ranging from -70 to 10.

The equation shown on the plot:

$$10\log_{10}\left(\frac{P(k_1, k_3, \omega)}{\phi_{pp}(\omega)k_c^{-2}}\right)$$

Plot annotations: Linear function of k_3; Cylinder Sensitivity Functions at peak k_1 locations; Acoustic Domain; Corcos (1964); Chase (1987); Smol'yakov (2006); All primary lobes completely outside acoustic domain in k_3 direction.

The x-axis is labeled **Normalized Crossflow Wavenumber, k_3/k_c** ranging from -0.1 to 0.1.

Figure 4.8 Relationship between the cross-flow wavenumber spectrum and measured sensitivity functions for identified cylindrical shell modes
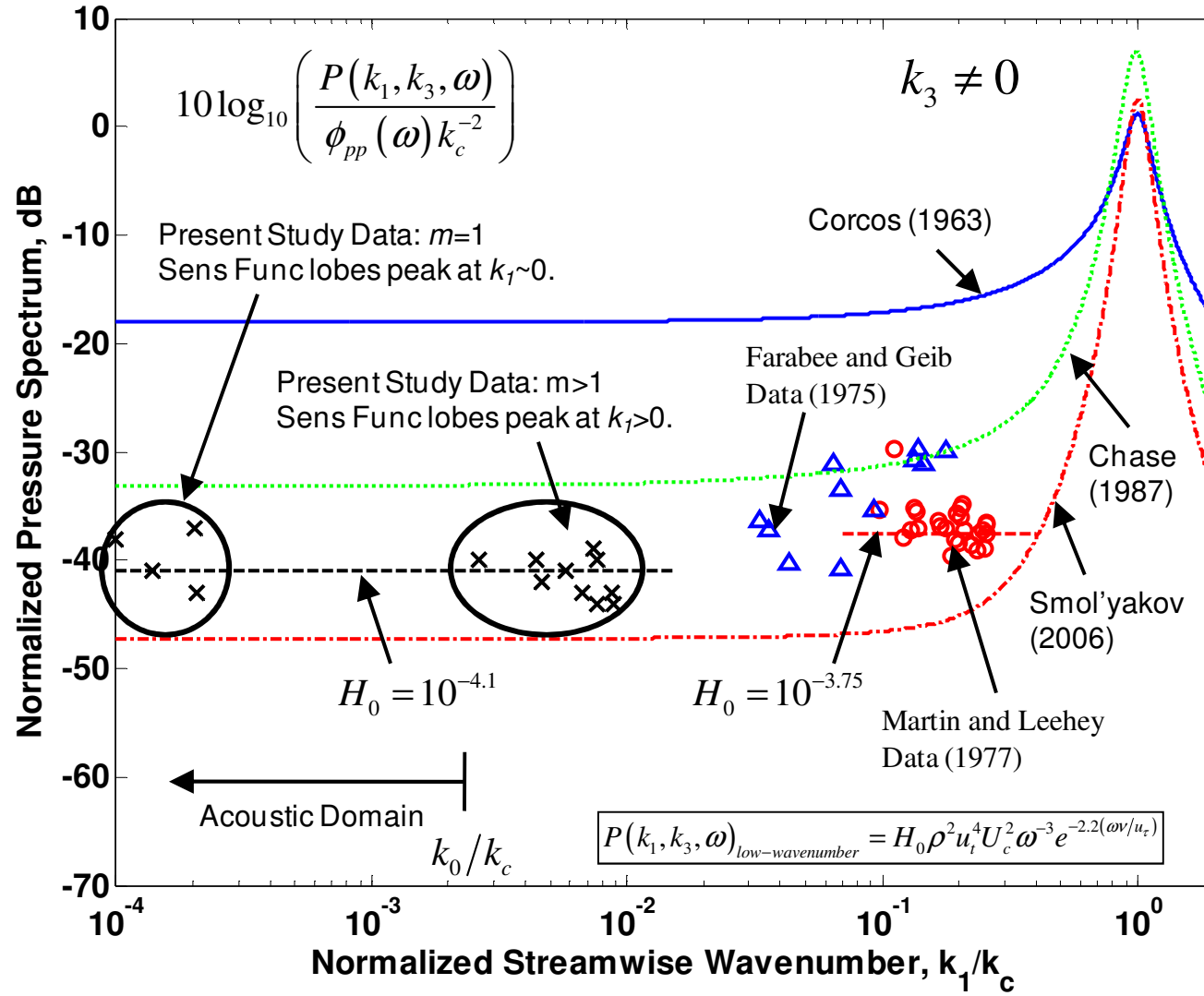
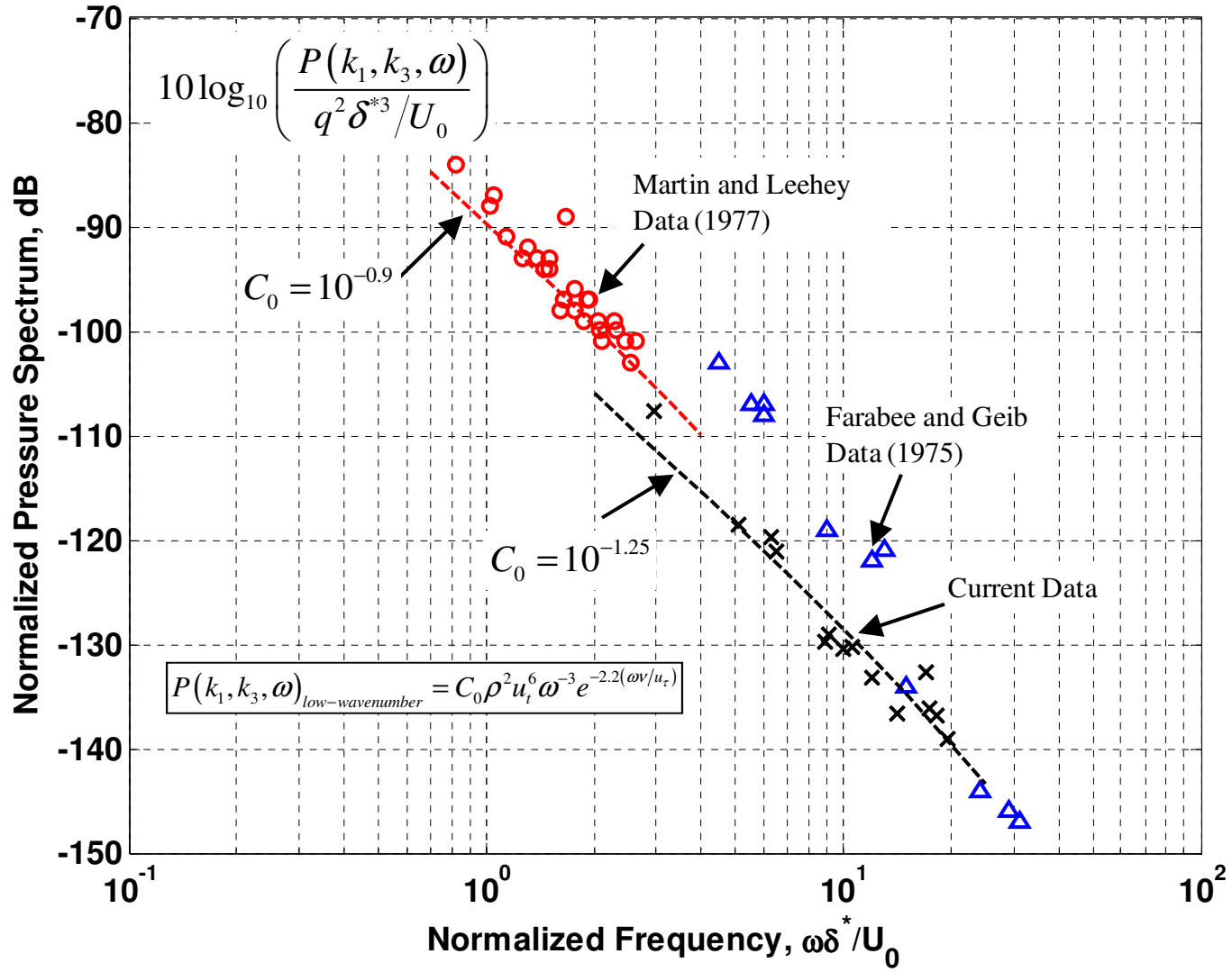Figure 4.9 Measured low wavenumber pressure spectrum levels as a function of reduced wavenumber

Figure 4.10 Measured low wavenumber pressure spectrum levels as a function of reduced frequency
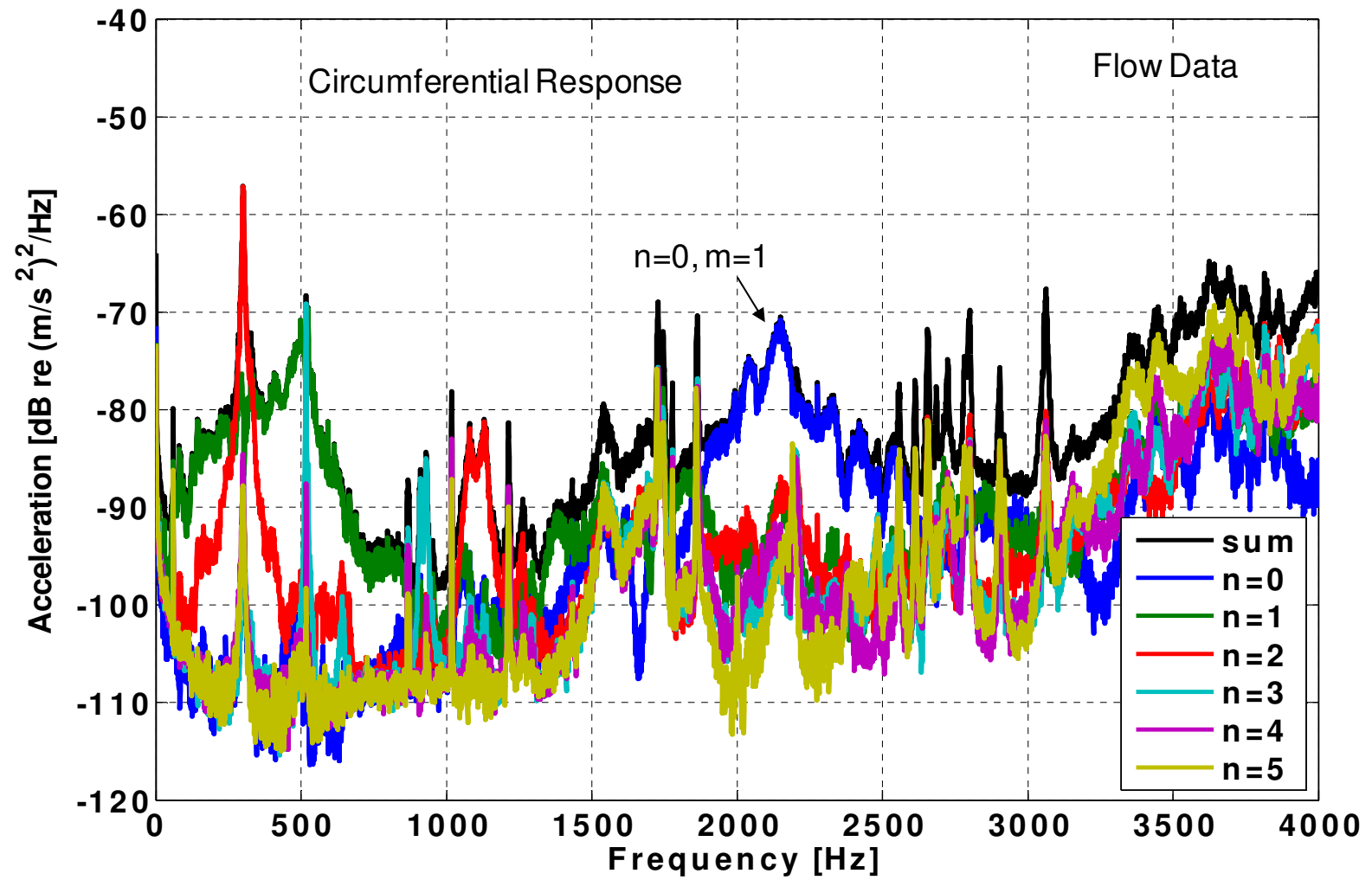
Figure 4.11 Measured average circumferential cylinder vibration with flow decomposed into circumferential Fourier components
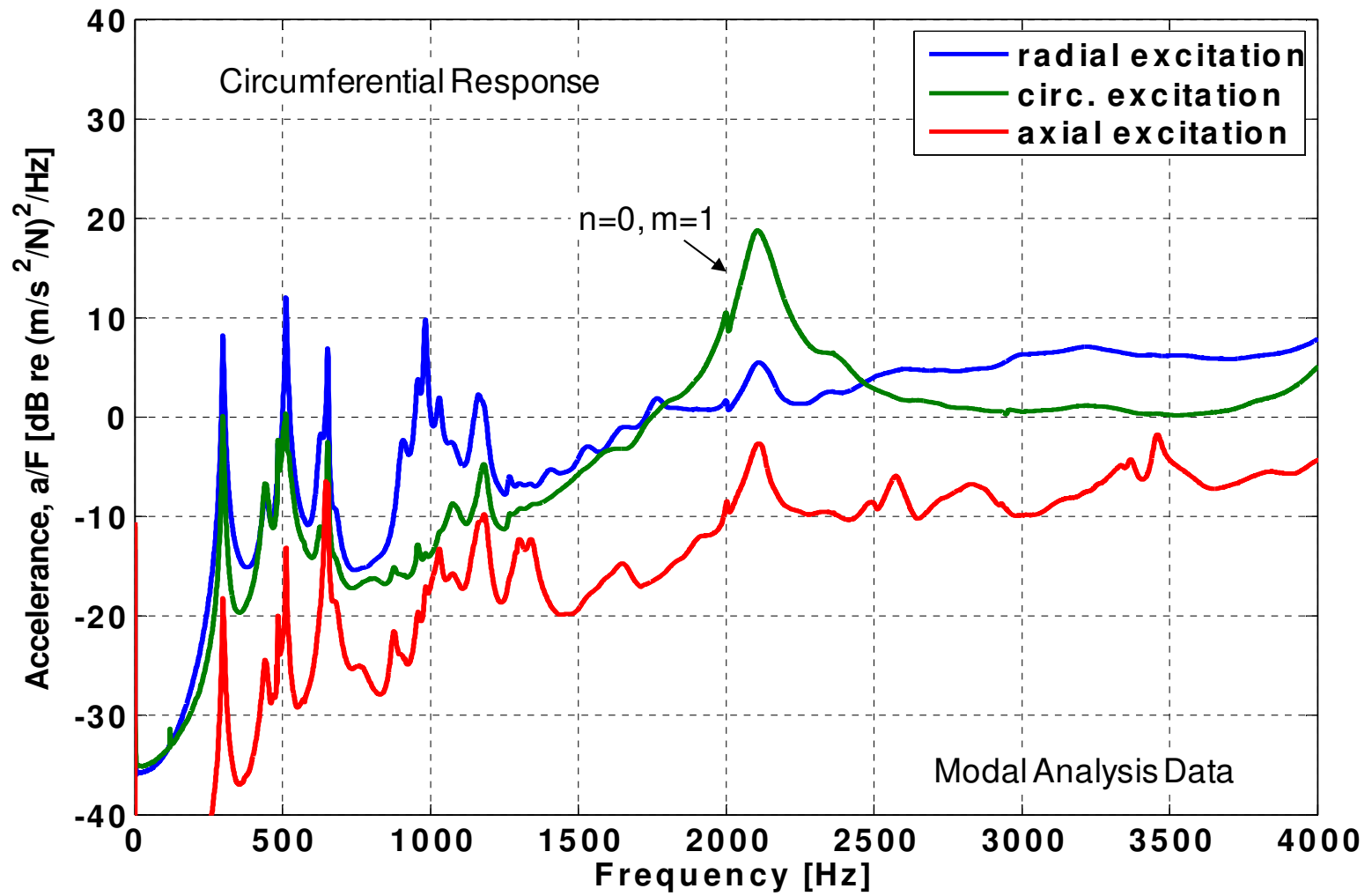
Figure 4.12 Experimental modal analysis average circumferential cylinder vibration in response to excitation in three coordinate directions
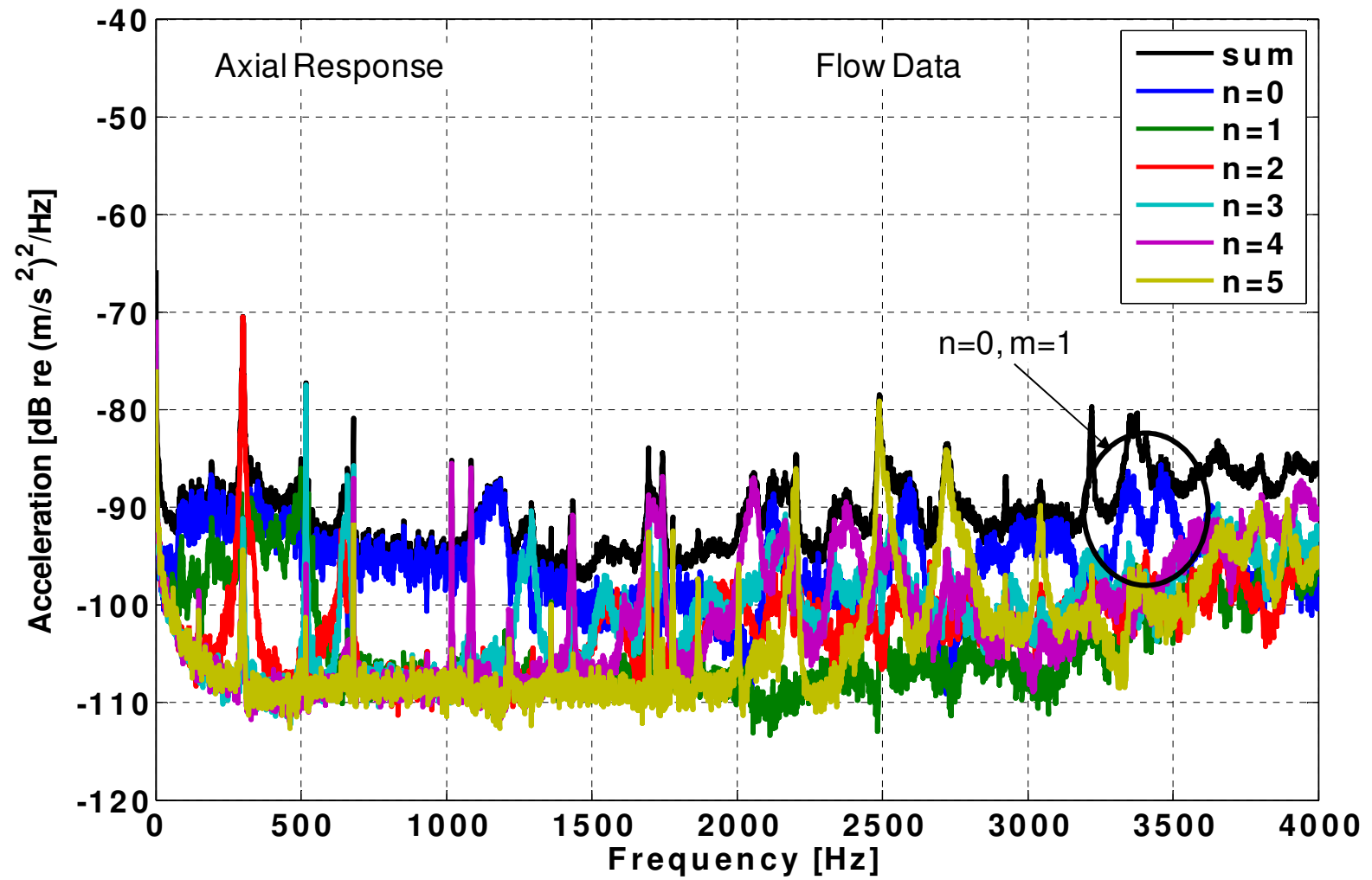
Figure 4.13 Measured average axial cylinder vibration with flow decomposed into circumferential Fourier
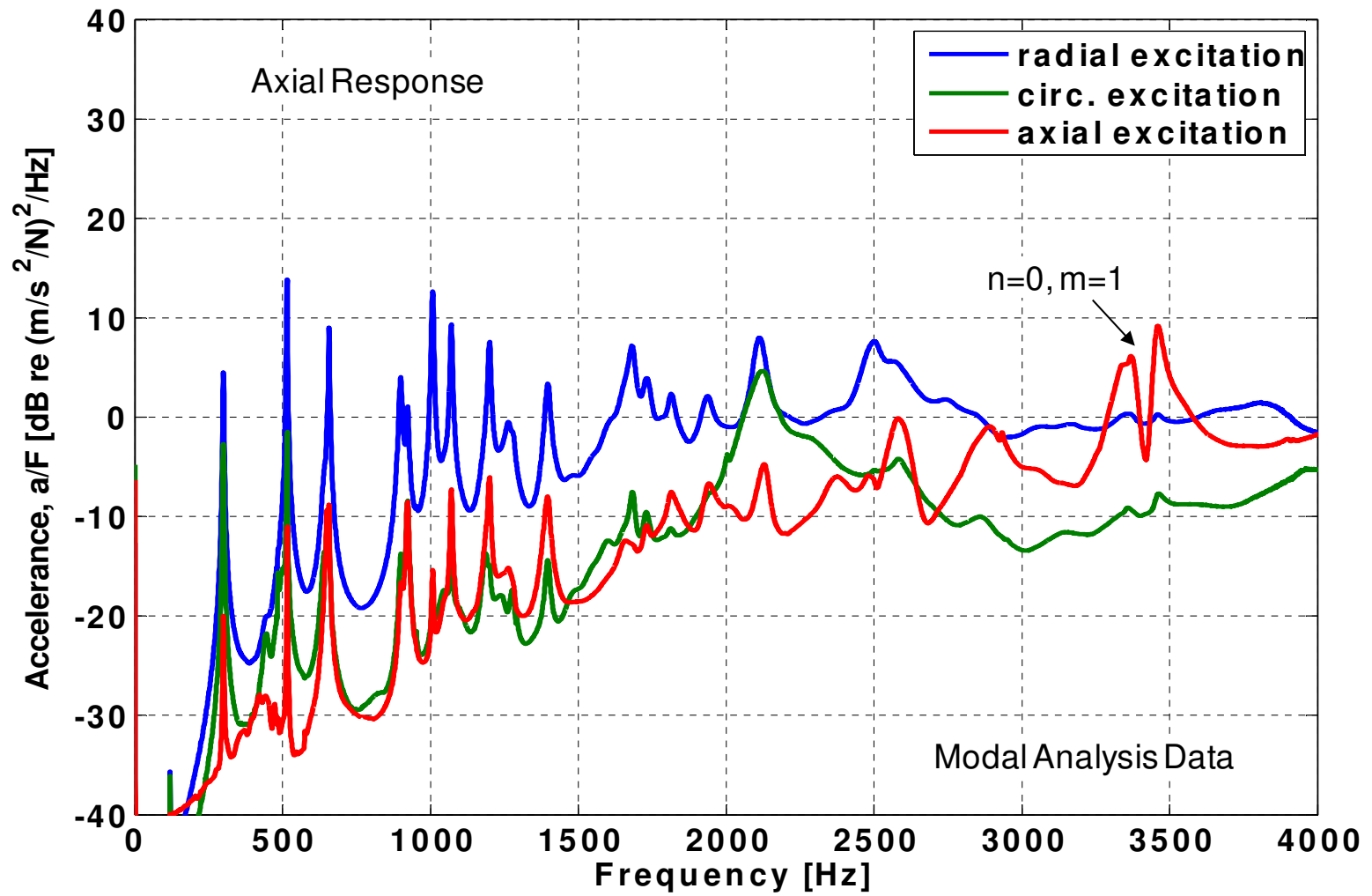   components

Figure 4.14 Experimental modal analysis average axial cylinder vibration in response to excitation in three
coordinate directions
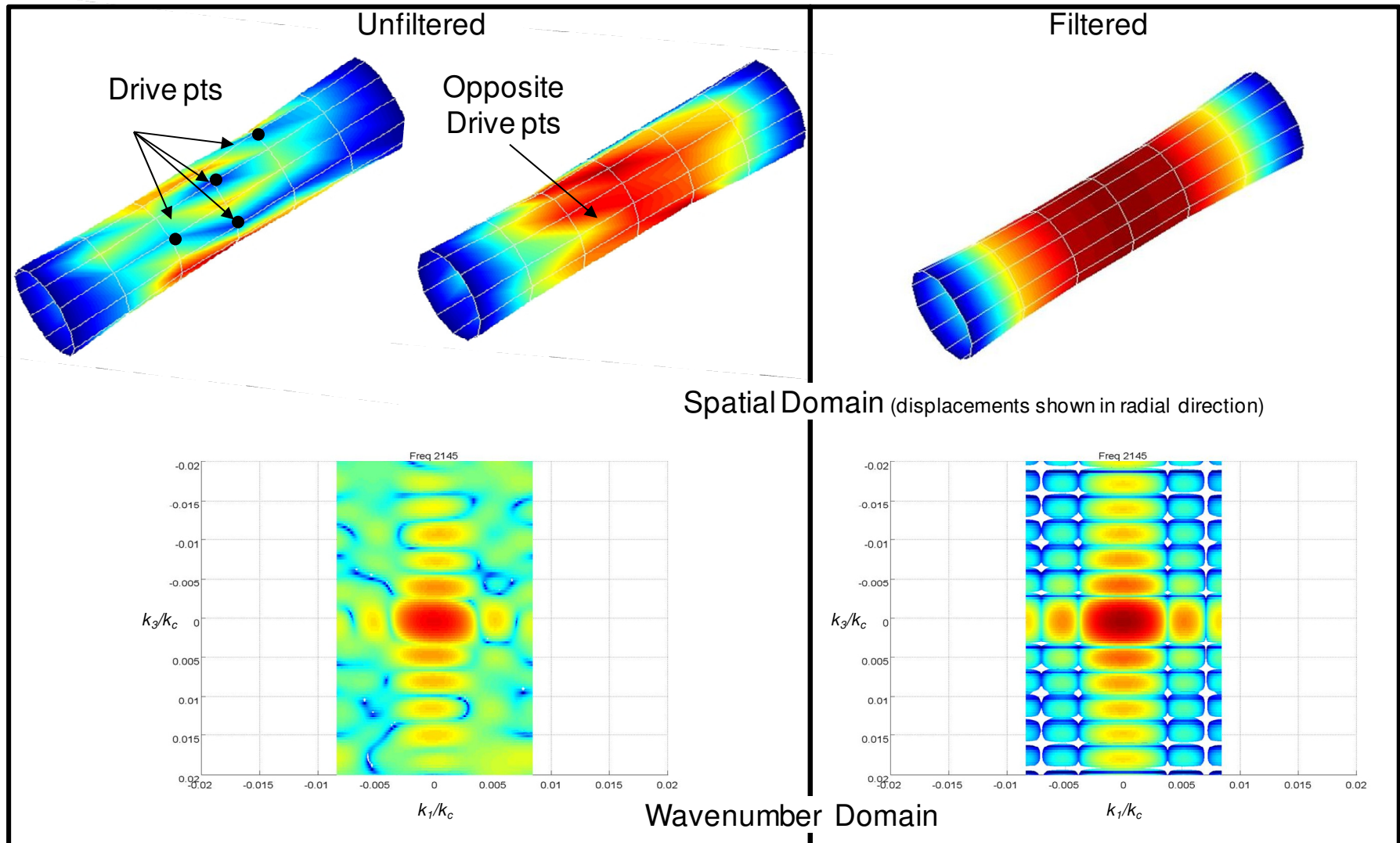
0,1 Circumferential - 2145 Hz

Unfiltered

Filtered

Drive pts

Opposite
Drive pts

Spatial Domain (displacements shown in radial direction)

Freq 2145

Freq 2145

k_3/k_c

k_3/k_c

k_1/k_c

k_1/k_c

Wavenumber Domain

Figure 4.15 Comparison of filtered and unfiltered cylinder mode shapes, circumferential n=0, m=1
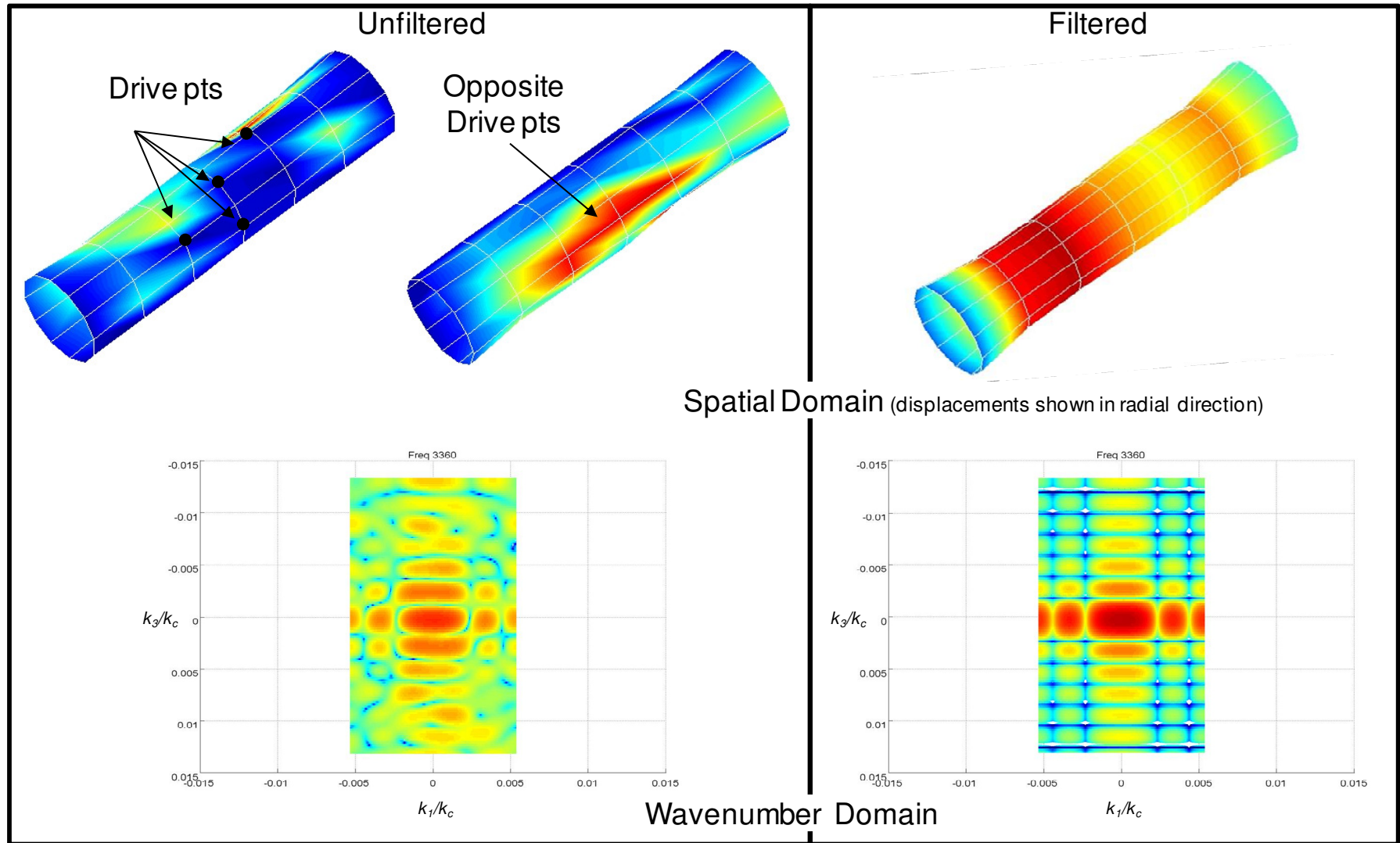
0,1 Axial - 3360 Hz

Figure 4.16 Comparison of filtered and unfiltered cylinder mode shapes, axial n=0, m=1
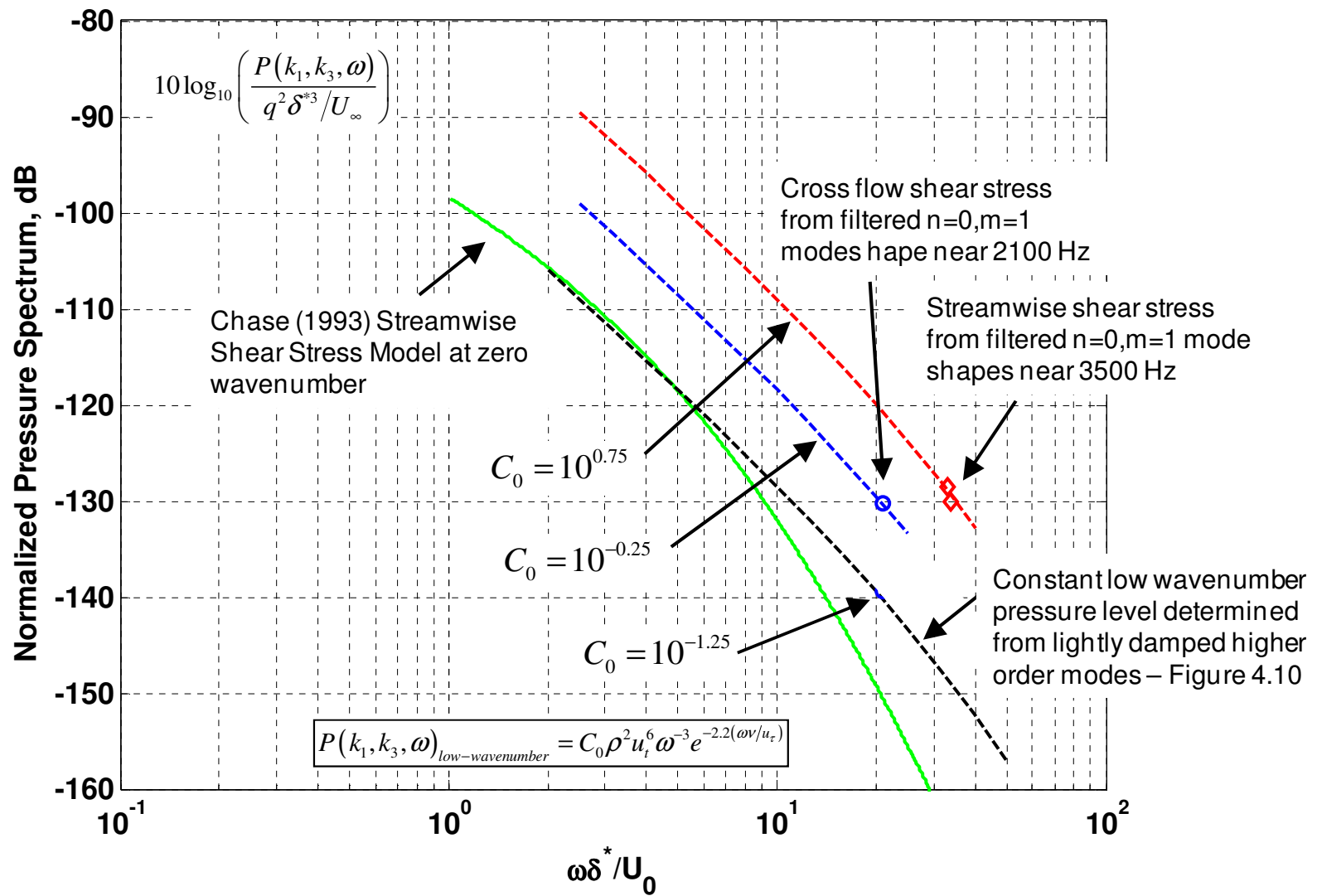
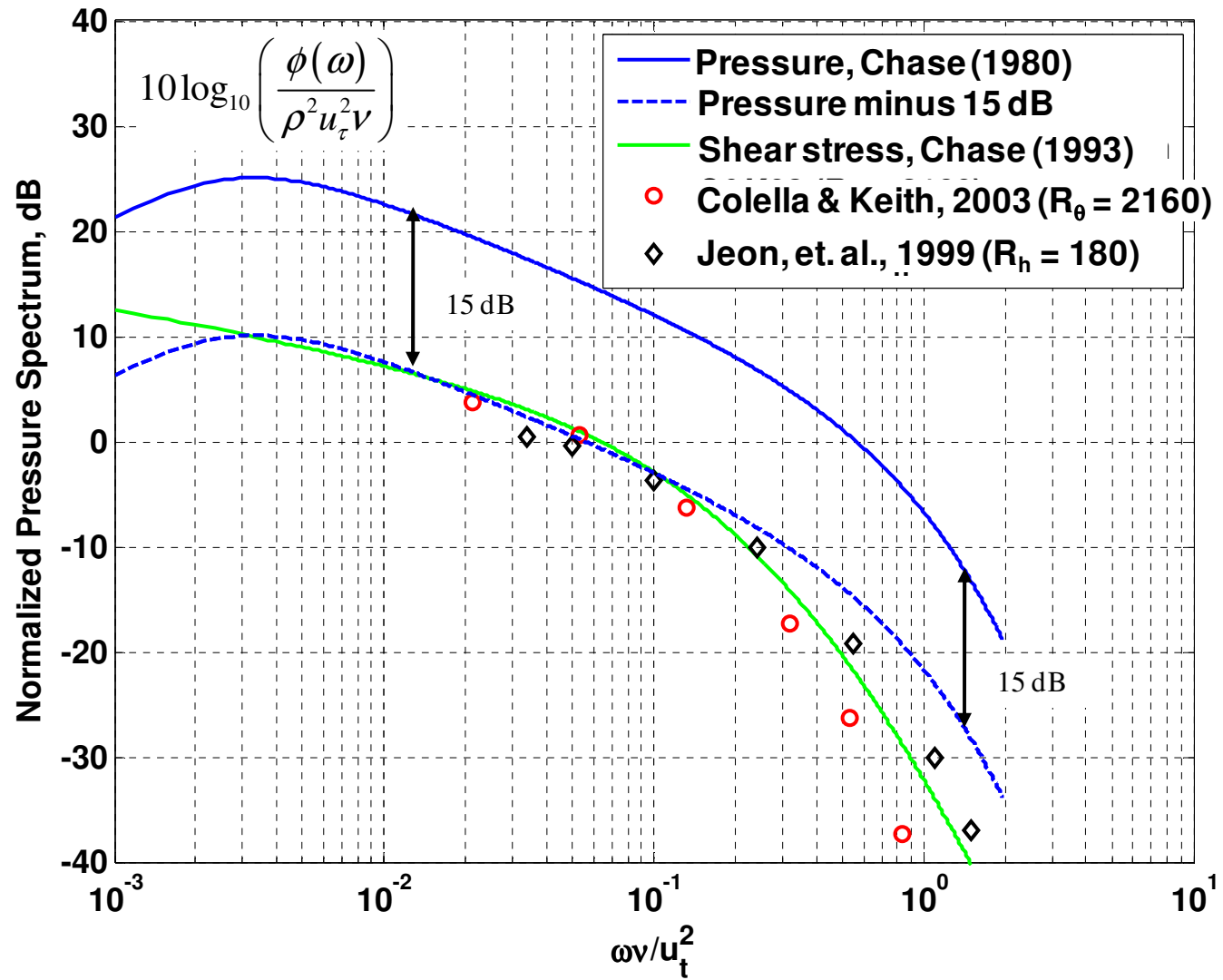Figure 4.17 Measured low wavenumber shear stress levels as a function of reduced frequency

Figure 4.18 Representative historical experimental TBL shear stress point frequency data compared with Chase models scaled on inner variables
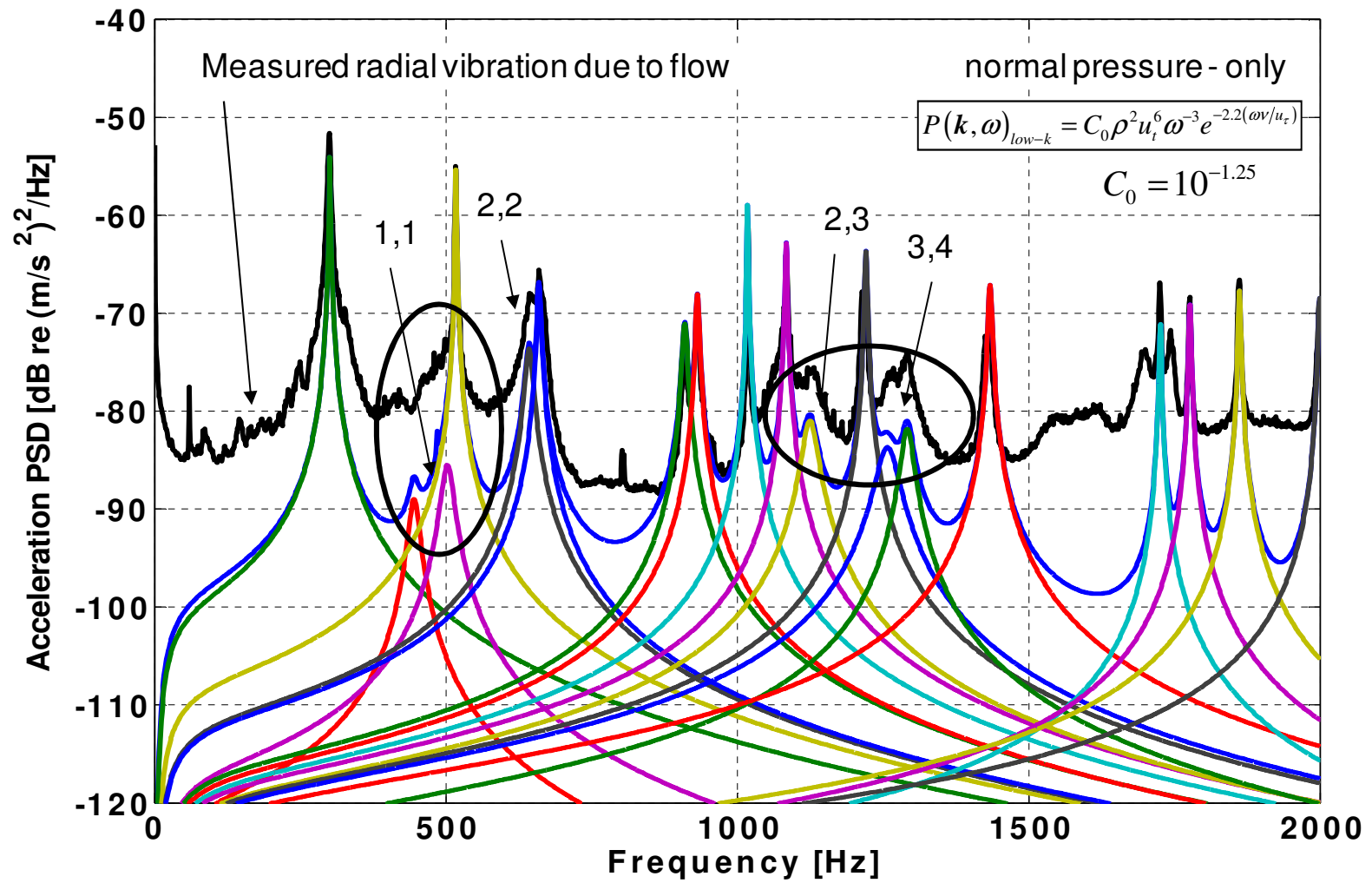
Figure 4.19 Estimated radial cylinder vibration spectra due to low wavenumber pressure levels corresponding to $C_0=10^{-1.25}$ compared to measured cylinder vibration
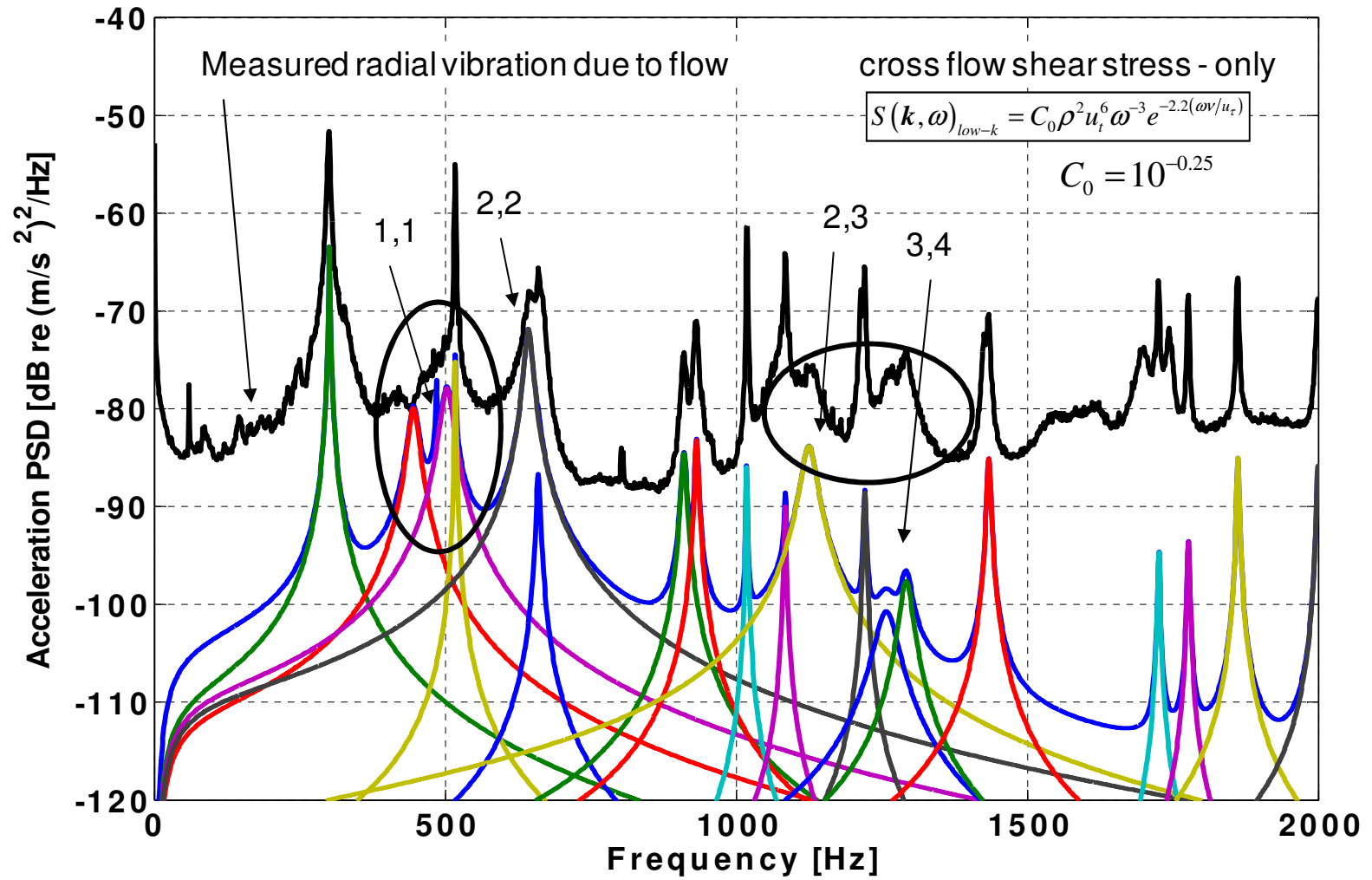
Figure 4.20 Estimated radial cylinder vibration spectra due to low wavenumber cross-flow shear stress levels corresponding to $C_0=10^{-0.25}$ compared to measured cylinder vibration
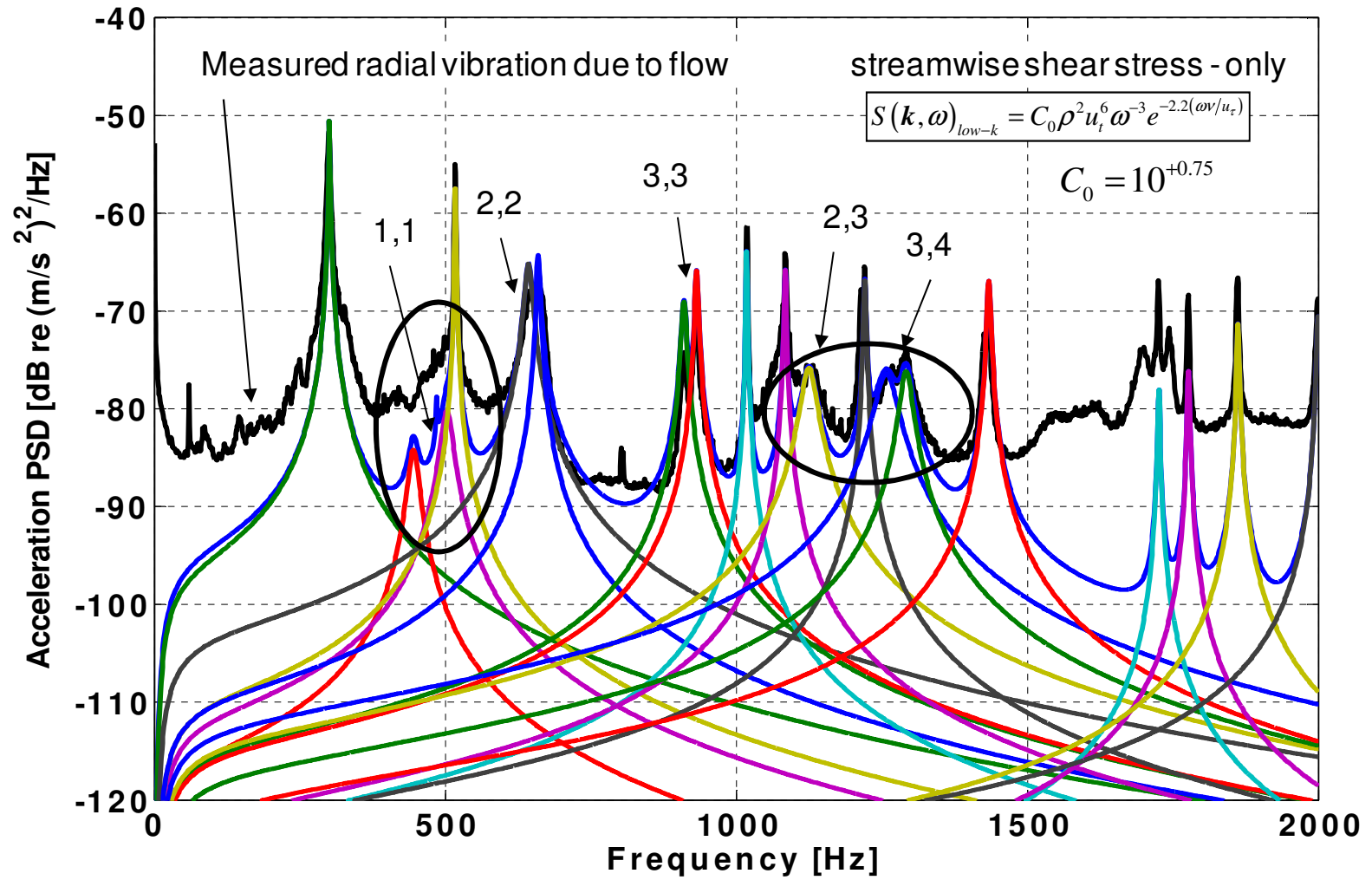
Figure 4.21 Estimated radial cylinder vibration spectra due to low wavenumber streamwise shear stress levels corresponding to $C_0=10^{+0.75}$ compared to measured cylinder vibration

Figure 4.22 Estimated radial cylinder vibration spectra due to low wavenumber pressure and shear stress compared to measured cylinder vibration

Figure 4.23 Final estimated radial cylinder vibration spectra due to low wavenumber pressure and shear stress compared to measured cylinder vibration

Chapter 5

SUMMARY, CONCLUSIONS, AND RECOMMENDATIONS
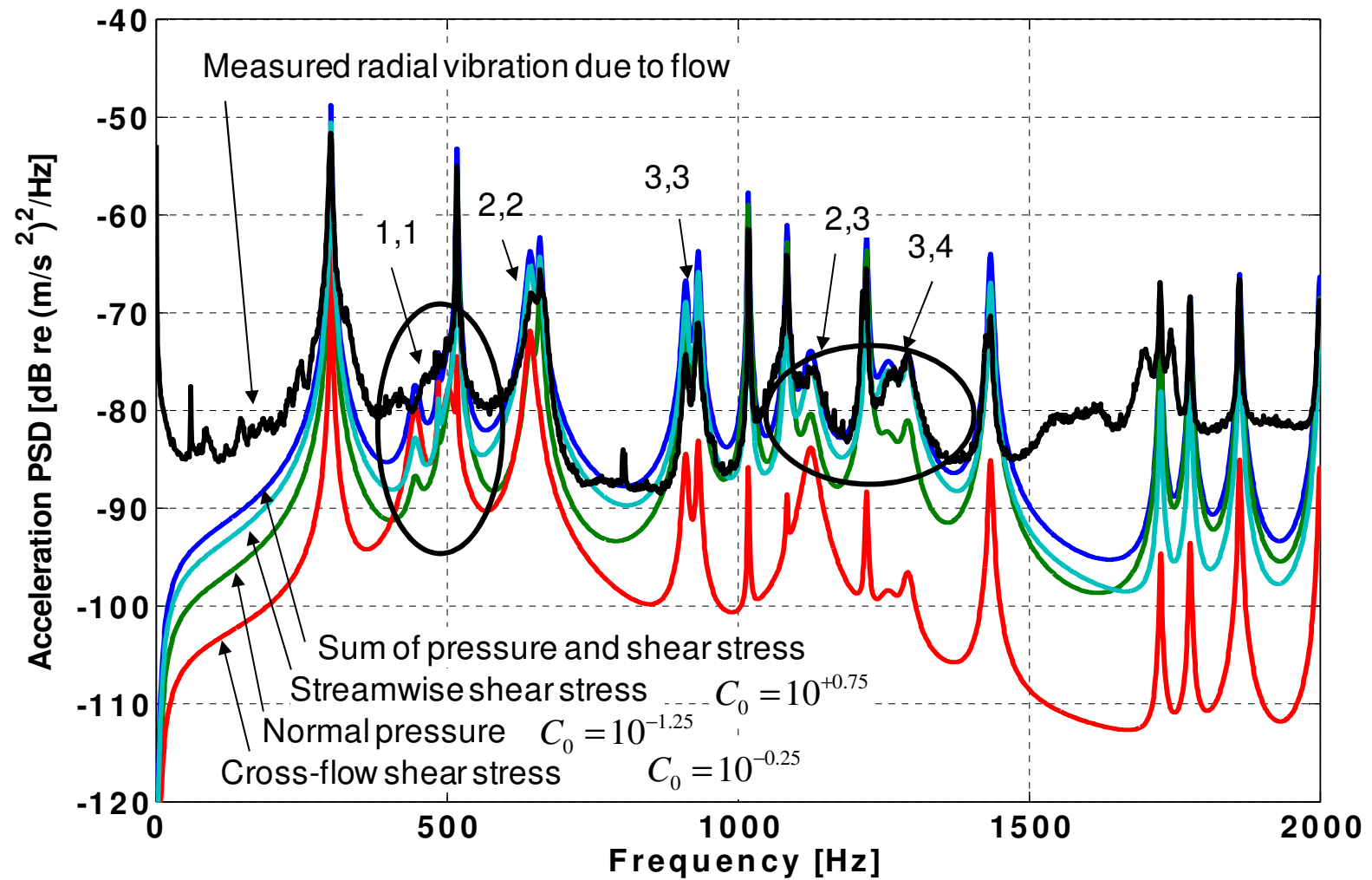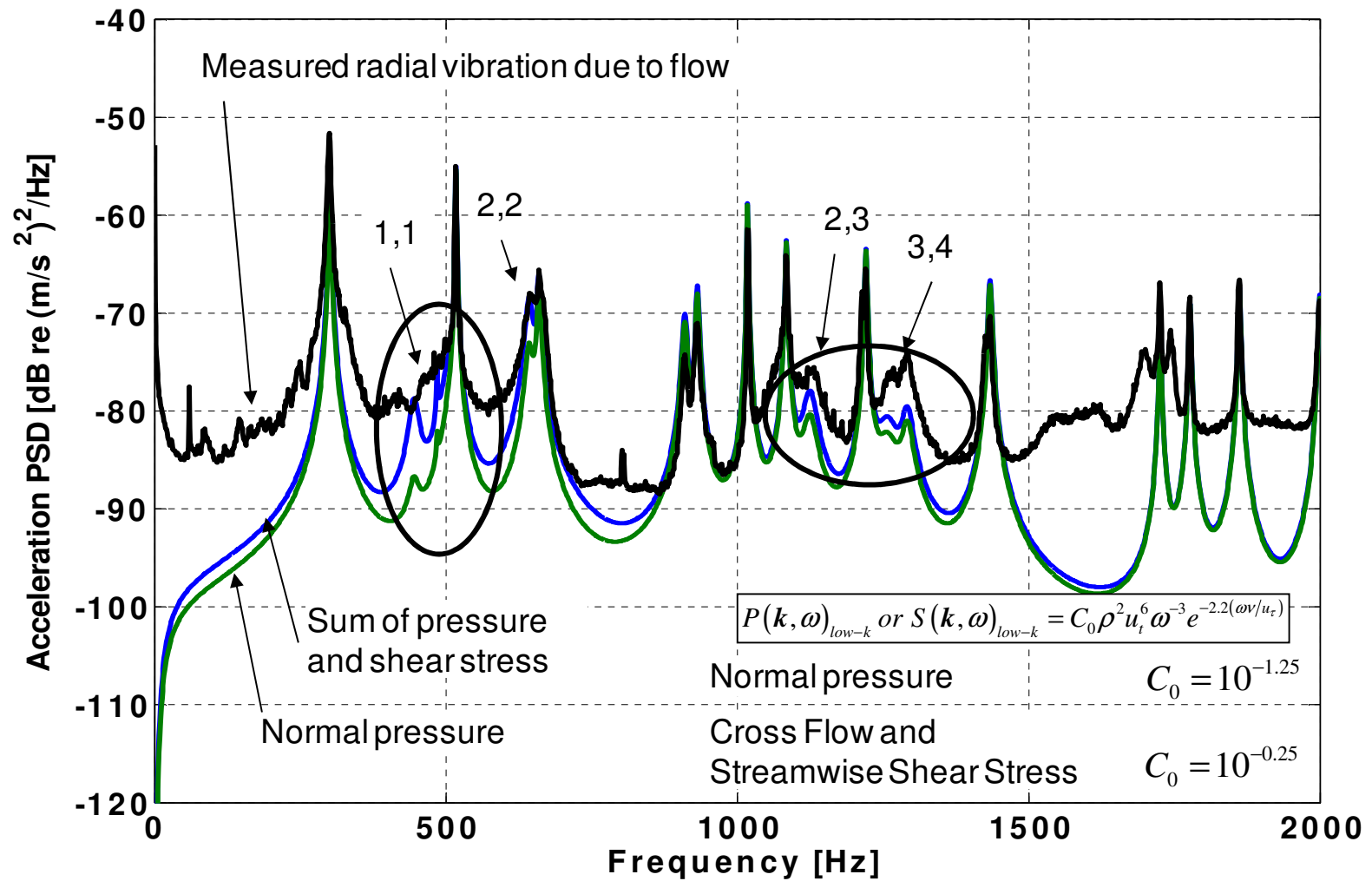
The specific goals of this work are to address the lack of measured TBL wall pressure data at especially low wavenumbers ($k_1/k_c < 0.01$) and the near complete absence of measured TBL cross-flow and streamwise shear stress data as a function of wavenumber. With these measurements, one can evaluate and improve existing empirical models of the TBL wall pressure and shear stress wavenumber domain.

These goals are accomplished by measuring the vibration response of a thin cylindrical shell to fully developed pipe flow at 6.1 m/sec in water. The measured vibration levels are used to inversely determine the low wavenumber TBL surface pressure and shear stress levels required to generate the cylinder's response . Making these measurements in water rather than air: broadens the low wavenumber domain for pressure and shear stress, increases the dynamic pressures in the operating fluid, and enables the use of the hydrostatic head of water to drive flow through a test-section reducing background noise levels.

A cylindrical shell is used as the structural filter (response structure) in the inverse measurement scheme. Since the dynamic response of a cylinder is coupled in all three coordinate directions, determining the dominant excitation direction responsible for any given mode of vibration is more difficult than for an uncoupled plate or membrane. However, directional coupling also presents the opportunity to sort out the contributions of cross-flow and streamwise shear stress in addition to normal wall pressure.

The role of viscosity or rotational effects that lead to the generation of increased fluctuating wall shear stress at low wavenumbers was largely neglected for many years. Chase (1993) suggested that viscosity induced shear stress may be important in certain applications of TBL excitation. Most underwater vehicles, for example, have curved surfaces where shear stress excitation can couple to flexural vibration and therefore cause noise radiation.

A three-dimensional experimental modal analysis of the cylinder filled with water was conducted to determine modal parameters needed to estimate TBL induced vibration levels based on assumed pressure or shear stress levels. The piping adjacent to the cylindrical shell test-section was also filled with water during modal analysis testing. The experimental modal analysis data shows much of the same spectral content as the measured cylinder vibration due to flow excitation.

The radial vibration levels for higher order lightly damped cylinder modes were used to evaluate normal pressure since these modes are primarily responsive to radial excitation and their displacement is primarily radial in nature. The circumferential and axial vibration levels for two low-order directionally uncoupled modes were used to isolate and evaluate shear stress in the cross-flow and streamwise directions respectively. The radial vibration levels for a few additional cylinder modes with more substantial coupling in multiple directions were used to assess the pressure and shear stress levels established from the low-order more uncoupled modes.

Using an assumed constant low wavenumber TBL wall pressure level at and around the modal wavenumber, cylinder vibration spectra for several higher order cylinder modes were estimated and compared with measured flow vibration data. The

constant low wavenumber pressure spectrum level which best represents the measured flow data is roughly 40 dB below the convective peak pressure level. This corresponds to a non-dimensional value of -41 dB shown in Figure 4.9 and leads to the wavenumber white forms for the TBL surface pressure spectrum at low wavenumber suggested in Equations 4.8 and 4.9.

The low wavenumber pressure level derived from these experiments falls midway between the Smol'yakov (2006) and Chase (1987) TBL wavevector-frequency models and is roughly 25 dB below the Corcos (1964) model. The level extracted from the current data is a few dB below the lower bound of measurements by Farabee and Geib (1975) and Martin and Leehey (1977).

In analyzing two low-order directionally uncoupled circumferential and axial modes to isolate and evaluate shear stress, vibration spectra were estimated and compared with corresponding measured flow vibration data for those two modes. The constant low wavenumber shear stress levels which best represent the measured flow data are roughly 10 dB above pressure for cross-flow shear stress and 20 dB above pressure for streamwise shear stress. Analysis of additional cylinder modes with more substantial coupling in multiple directions confirms the pressure and cross-flow shear stress levels established from the uncoupled modes, but suggests the streamwise shear stress level of 20 dB above pressure is too high. In view of the greater reliability of the cross-flow results, it is believed that the streamwise low wavenumber level is similar to the cross-flow low wavenumber level. The current experimental cylinder lacks additional vibration modes required to more fully evaluate streamwise shear stress.

As is the case for various models of TBL pressure, these measurements suggest that a nearly constant value for normalized shear stress at low wavenumber is valid over a broad range of frequencies. The same wavenumber white model forms suggested for low wavenumber TBL surface pressure are also appropriate for shear stress - though different coefficients are required. Results from this research, along with others, indicate that low wavenumber pressure is roughly 40 dB below its convective peak level. In contrast, low wavenumber shear stress is likely no more than 15 dB below its convective peak level.

Low wavenumber pressure results from this study are consistent with past research, however, the shear stress results are not. Current results indicate the low wavenumber shear stress levels are 10 dB higher than those of pressure, whereas past research suggests they are comparable. In light of this difference, additional measurements of low wavenumber shear stress should be conducted. Resolving this discrepancy is important for accurately modeling TBL excitation of marine vehicles.

An important aspect of the structural response to TBL excitation not addressed in this study and one which has received relatively little attention is the effect of surface roughness on low wavenumber TBL excitation (Blake, 1970, Howe , 1988, 1991). While this study focuses on establishing the smooth wall levels of TBL surface pressure and shear stress, the current measurement facility and approach could be readily extended to a provide a systematic evaluation of how TBL excitation is affected by surface roughness.

BIBLIOGRAPHY

Abe, H., Kawamura, H., and Choi, H. (2004), "Very Large-Scale Structures and their Effect on the Wall Shear Stress Fluctuations in a Turbulent Channel Flow up to Ret=640," Journal of Fluids Engineering, Vol. 126, pp. 835-843.

Abraham, B.M. and Keith, W.L. (1998), "Direct Measurements of Turbulent Boundary Layer Wall Pressure Wavenumber - Frequency Spectra," Journal of Fluids Engineering, Vol. 120, pp. 29-39.

Bendat J.S. and Persol, A.G. (1986), "Random Data – Analysis and Measurement Procedures," John Wiley & Sons, Inc, New York, NY.

Bakewell, H.P., Carey, G.F., Libuka, J.J., Schloemer, H.H., and Von Winkle, W.A. (1962), "Wall Pressure Correlations in Turbulent Pipe Flow", US Navy Underwater Sound Laboratory Report No. 559

Blake, W.K. (1970), "Turbulent boundary-layer wall-pressure fluctuations on smooth and rough walls," Journal of Fluid Mechanics, 44(4), pp. 637-660.

Blake, W.K. and Chase, D.M. (1971), "Wavenumber-Frequency of Turbulent-Boundary –Layer Pressure Measured by Microphone Arrays," Journal of the Acoustical Society of America, 49(3), pp. 1017-1024

Blake, W.K. (1986), "Mechanics of Flow-Induced Sound and Vibration," Academic, New York, 1986, Vol. II, Chpt. 8

Catbas, N., Brown, D. L., and Aktan , A. E., (2004), "Parameter estimation for multiple-input multiple-output modal analysis of large structures", Journal of Engineering Mechanics, 130 (8), 921-930.

Chase, D.M. (1980), "Modeling the Wavevector-Frequency Spectrum Interaction," Journal of Sound and Vibration, 70, pp. 29-67.

Chase, D.M. (1987), "The Character of the Turbulent Wall Pressure Spectrum at Subconvective Wavenumbers and a Suggested Comprehensive Model," Journal of Sound and Vibration, 112, pp. 125-147.

Chase, D.M. (1991a), "The Wavevector-Frequency Spectrum of Pressure on a Smooth Plane in Turbulent Boundary-Layer Flow at Low Mach Number," Journal of the Acoustical Society of America, Vol. 90, No. 2, Pt. 1, pp. 1032-1040.

Chase, D.M. (1991b), "Fluctuations in wall-shear stress and pressure at low streamwise wavenumbers in turbulent boundary-layer flow," Journal of Fluid Mechanics, Vol. 225, pp. 545-555.

Chase, D.M. (1992), "Fluctuating Wall-Shear Stress and Pressure at Low Streamwise Wavenumbers in Turbulent Boundary-Layer Flow at Low Mach Numbers," Journal of Fluids and Structures, 6, pp. 395-413.

Chase, D.M. (1993), "A Semi-Empirical Model for the Wavevector-Frequency Spectrum of Turbulent Wall-Shear Stress," Journal of Fluids and Structures, x, pp. 639-659.

Colella, K.J. and Keith, W.L. (2003), "Measurements and Scaling of Wall Shear Stress Fluctuations," Experiments in Fluids, Vol. 34, pp. 253-260.

Corcos, G.M. (1963), "Resolution of Pressure in Turbulence," The Journal of the Acoustical Society of America, Vol. 35, No. 2, pp. 192-198.

Corcos, G.M. (1964), "The Structure of the Turbulent Pressure Field in Boundary-Layer Flows," The Journal of Fluid Mechanics, Vol. 18, No. 3, pp. 353-378.

Efimstov, B.M. (1982), "Characteristics of the Field of Turbulent Wall Pressure Fluctuations at Large Reynolds Numbers," Soviet Physics - Acoustics, Vol. 28, No. 4, pp. 289-292.

Ewins, D.J. (2001), "Modal Testing: Theory, Practice, and Applications, 2nd Ed.," Research Studies Press, Hertfordshire, England.

Farabee, T.M. and Geib, F.E. (1975), "Measurement of Boundary Layer Pressure Fields with an Array of Pressure Transducers in a Subsonic Flow," ICIASF '75 Record, pp. 311-319

Ffowcs Williams, J.E. (1982), "Boundary-Layer Pressures and the Corcos Model: a development to incorporate Low Wavenumber Constrains," Journal of Fluid Mechanics, Vol. 125, pp. 9-12.

Goody, M.C. (2004), "Empirical Spectral Model of Surface Pressure Fluctuations," Journal of AIAA, 42(9), pp. 1788-1794.

Graham, W.R. (1997), "A Comparison of Models for the Wavenumber-Frequency Spectrum of Turbulent Boundary Layer Pressures," Journal of Sound and Vibration, 206(4), pp. 542-565.

Hariri, H.H., and Akylas, T.R. (1985), "The wall-shear stress contribution to boundary-layer noise," Physics of Fluids, Vol. 28, No. 9, pp. 2727-2729.

Hespeel, D., Giovannelli, G., and Forestier, B.E. (1998), "Frequency-Wavenumber Spectrum Measurement of the Wall Shear Stress Fluctuations Beneath a Planar Turbulent Boundary Layer," Proceedings of the ASME Noise Control and Acoustics Division, NCA-Vol. 25, pp. 77-84.

Hu, Z.W., Morfey, C.L., and Sandham, N.C. (2002), "Aeroacoustics of Wall-Bounded Turbulent Flows," AIAA Journal, Vol. 40, pp. 465-473.

Howe, M.S. (1979), "The Role of Surface Shear Stress Fluctuations in the Generation of Boundary Layer Noise," Journal of Sound and Vibration, 65, pp. 159-164.

Howe, M.S. (1988), "The Turbulent Boundary-Layer Rough-Wall Pressure spectrum at Acoustic and Subconvective Wavenumbers," Proceedings of the Royal Society of London, 415, pp. 141-161.

Howe, M.S. (1991), "Surface pressures and sound produced by turbulent flow over smooth and rough walls," Journal of the Acoustical Society of America, 90(2), Pt. 1, pp. 1041-1047.

Howe, M.S. (1995), "The Damping of Sound by Wall Turbulent Shear Layers," Journal of the Acoustical Society of America, Vol. 98, No. 3, pp. 1723-1730.

Howe, M.S. (1998), "Acoustics of Fluid-Structure Interactions," Cambridge University Press, Cambridge, UK.

Hwang, Y.F., Bonness, W.K., and Hambric, S.A. (2008), "Comparison of Semi-Empirical Models of Turbulent Boundary Layer Pressure Spectra," Journal of Sound and Vibration, 142(1), pp. 1xx-1xx.

Hwang, Y.F. and Maidanik, G. (1990), "A Wavenumber Analysis of the Coupling of a Structural Mode and Flow Turbulence," Journal of Sound and Vibration, 142(1), pp. 135-152.

Jameson, P.W. (1975), "Measurement of the Low Wavenumber Component of Turbulent Boundary Layer Pressure spectral Density," Proceedings of the Fourth Biennial Symposium on Turbulence in Liquids, pp. 192-200

Keith, W.L. and Bennett, J.C. (1991), "Low-Frequency Spectra of the Wall Shear Stress and Wall Pressure in a Turbulent Boundary Layer," AIAA Journal, April, 1991Vol. 29, No. 4, pp. 526-530.

Kinsler, L.E., Frey, A.R., Coppens, A.B., Sanders, J.V. (1982), "Fundamentals of Acoustics - Third Edition," John Wiley & Sons, New York, NY.

Ko, S.H. (1993), "Performance of Various Shapes of Hydrophones in the Reduction of Turbulent Flow Noise," The Journal of the Acoustical Society of America, Vol. 93, No. 3, pp. 1293-1299.

Kraichnan, R.H. (1956), "Pressure Fluctuations in Turbulent Flow over a Flat Plate," The Journal of the Acoustical Society of America, 28(3), pp. 378-390

Khoo, B.C., Chew, Y.T., and Teo, C.L. (2001), "Near-Wall Hot-Wire Measurements – Part II: Turbulence time scale, convective velocity, and spectra in the viscous sublayer," Experiments in Fluids, Vol. 31, pp. 494-505.

Laws, E. M. (1990), "Flow conditioning - a new development," Flow Measurement Instrumentation, Vol. 1, No. 3, pp. 165-l 70.

Leehey, P. (1988), "Structural Excitation by a Turbulent Boundary Layer: An Overview," Transactions of the ASME, Vol. 110, April 1988, pp. 220-225

Lysak, P.D. (2006), "Modeling the Wall Pressure Spectrum in Turbulent Pipe Flows," Journal of Fluids Engineering, Vol 128, pp. 216-222.

Manoha, E. (1996), "The Wavenumber-Frequency Spectrum of the Wall Pressure Fluctuations beneath a Turbulent Boundary Layer," 2nd AIAA/CEAS Aeroacoustics Conference, May 6-8, 1996, State College, PA

Maidanik, G. (1967), "Flush-Mounted Pressure Transducer Systems as Spatial and Spectral Filters," The Journal of the Acoustical Society of America, 42(5), pp. 1017-1024

Martin, N.C. and Leehey, P. (1977), "Low Wavenumber Wall Pressure Measurements Using a Rectangular Membrane as a Spatial Filter," Journal of Sound and Vibration, 52(1), pp. 95-120.

Schlichting, H. (1979), "Boundary-Layer Theory, Seventh Edition", McGraw-Hill, New York, NY.

Sejeong, J., Choi, H., and Jung, Y.Y. (1999), "Space-time characteristics of the wall shear stress fluctuations in a low-Reynolds-number channel flow," Physics of Fluids, Vol. 11, No. 10, pp. 3084-3094.

Skelton, E.A. and James, J.H. (1997), "Theoretical Acoustics of Underwater Structures," Imperial College Press, pp. 373-381.

Smol'yakav, A.V. and Tkachenko, V.M. (1991), "Model of a Field of Pseudosonic Turbulent Wall Pressures and Experimental Data," Soviet Physical Acoustics 37, pp. 627-631.

Smol'yakav, A.V. (2000), "Calculation of the Spectra of Pseudosound Wall-Pressure Fluctuations in Turbulent Boundary Layers," Acoustical Physics, Vol. 46, No. 3, pp. 342-347.

Smol'yakav, A.V. (2006), "A New Model for the Cross Spectrum and Wavenumber-Frequency Spectrum of Turbulent Pressure Fluctuations in a Boundary Layer," Acoustical Physics, Vol. 52, No. 3, pp. 331-337.

Spearman, E. P., Sattary, J. A. and Reader-Harris, M. J. (1996), "Comparison of Velocity Profiles Downstream of Perforated Plate Flow Conditioners," Flow Measurement Instrumentation, Vol. 7, No. 3/4, pp. 181-l 99.

Willmarth, W.W. and Wooldridge, C.E. (1962), "Measurements of the Fluctuating Pressure at the Wall Beneath a Thick Turbulent Boundary Layer," Journal of Fluid Mechanics, Vol. 14, pp. 187.

Xiong, W., Kalkuhler, K., and Merzkirch, W., (2003), "Velocity and Turbulence Measurements Downstream of Flow Conditioners," Flow Measurement Instrumentation, Vol. 14, pp. 249-260.

VITA

William Kris Bonness

William Bonness was born in Omaha, Nebraska on August 8, 1963. He graduated from Bellevue East High School in Bellevue, Nebraska in June 1981. He graduated with a Bachelor of Science in Mechanical Engineering from The University of Nebraska - Lincoln in December 1985. William graduated with a Master of Science in Mechanical Engineering from The University of California - Berkeley in May 1991. He received a Doctor of Philosophy in Acoustics from The Pennsylvania State University in August 2009.

William worked from December 1986 through August 1989 at the Fleet Analysis Center in Corona, CA where he traveled extensively to monitor naval training exercises aboard participating ships and aircraft. From September 1991 through May 1998, he worked at the Naval Surface Warfare Center in Carderock, MD conducting experimental research involving the generation and reduction of noise associated with hydrodynamic sources and the structural response of marine structures. Since June 1998, he has worked at the Applied Research Lab at Penn State University where he conducts fundamental and applied research in the fields of hydrodynamics, hydroacoustics, and structural acoustics.